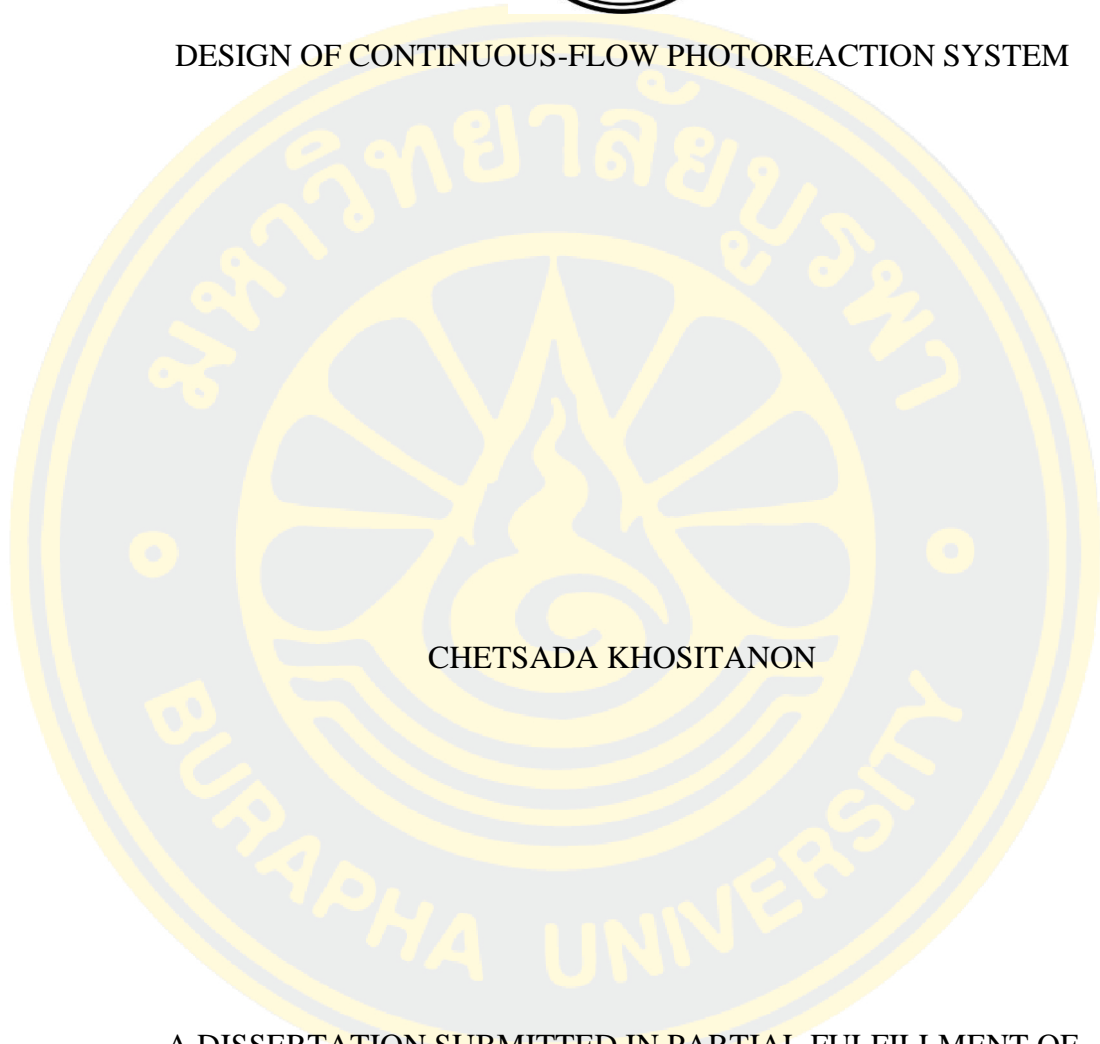




DESIGN OF CONTINUOUS-FLOW PHOTOREACTION SYSTEM



CHETSADA KHOSITANON

A DISSERTATION SUBMITTED IN PARTIAL FULFILLMENT OF
THE REQUIREMENTS FOR DOCTOR DEGREE OF PHILOSOPHY

IN CHEMICAL ENGINEERING

FACULTY OF ENGINEERING

BURAPHA UNIVERSITY

2024

COPYRIGHT OF BURAPHA UNIVERSITY

การออกแบบระบบสำหรับการทำปฏิริยาเชิงแสงในลักษณะไหลต่อเนื่อง



เจษฎา โฉมิตานนท์

คุณูปนิพนธ์นี้เป็นส่วนหนึ่งของการศึกษาตามหลักสูตรปรัชญาดุษฎีบัณฑิต

สาขาวิชาวิศวกรรมเคมี

คณะวิศวกรรมศาสตร์ มหาวิทยาลัยบูรพา

2567

ลิขสิทธิ์เป็นของมหาวิทยาลัยบูรพา



CHETSADA KHOSITANON

A DISSERTATION SUBMITTED IN PARTIAL FULFILLMENT OF
THE REQUIREMENTS FOR DOCTOR DEGREE OF PHILOSOPHY
IN CHEMICAL ENGINEERING
FACULTY OF ENGINEERING
BURAPHA UNIVERSITY

2024

COPYRIGHT OF BURAPHA UNIVERSITY

The Dissertation of Chetsada Khositanon has been approved by the examining committee to be partial fulfillment of the requirements for the Doctor Degree of Philosophy in Chemical Engineering of Burapha University

Advisory Committee

Examining Committee

Principal advisor

.....
(Associate Professor Dr. Nopphon Weeranoppanant)

..... Principal examiner
(Professor Richard Anthony Bourne)

..... Member
(Associate Professor Dr. Pailin Ngaotrakanwiwat)

..... Member
(Associate Professor Dr. Nopphon Weeranoppanant)

..... Member
(Assistant Professor Dr. Sareeya Bureekaew)

..... External Member
(Professor Suttichai Assabumrungrat)

..... Dean of the Faculty of Engineering
(Assistant Professor Nayot Kurukitkoson)

This Dissertation has been approved by Graduate School Burapha University to be partial fulfillment of the requirements for the Doctor Degree of Philosophy in Chemical Engineering of Burapha University

..... Dean of Graduate School
(Associate Professor Dr. Witawat Jangiam)

.....

61810004: MAJOR: CHEMICAL ENGINEERING; Ph.D. (CHEMICAL ENGINEERING)
KEYWORDS: CONTINUOUS FLOW PROCESS/ NANOPARTICLE SYNTHESIS/ CONTINUOUS PURIFICATION/ SOLVENT EXTRACTION/ CATALYTIC PERFORMANCE/ SILVER NANOPARTICLE/ CONTINUOUS-FLOW PHOTOCATALYTIC REACTOR/ DOPAMINE-ASSISTED IMMOBILIZATION/ FLUOROPOLYMER TUBING/ METHYLENE BLUE DECOLORIZATION/ PHOTOCATALYTIC BENZENE HYDROXYLATION/ PHOTOCATALYTIC FILM REACTOR
CHETSADA KHOSITANON : DESIGN OF CONTINUOUS-FLOW PHOTOREACTION SYSTEM. ADVISORY COMMITTEE: NOPPHON WEERANOPPANANT, Ph.D. 2024.

Continuous flow systems are extensively employed in chemical engineering due to their efficiency and reliable output. These systems operate with a continuous stream of inputs, allowing for uninterrupted chemical reactions. One major advantage of continuous flow systems is their ability to maintain steady-state conditions, which improve product quality and increase overall productivity. Unlike batch processing, where materials are added in discrete amounts and each batch must be processed before adding new material, continuous flow systems provide a constant and uniform flow of material throughout the process. Continuous flow systems are employed in many chemical reactions. In this thesis, we interested in inorganic material synthesis (chapter 3) and photochemical reaction (chapter 4 and 5)

In chapter 3, we developed a simple continuous flow system made of a PFA tube to purify silver nanoparticles (AgNPs) which were synthesized from chemical reduction. The continuous-flow extraction is a promising technique to remove impurities from the solution. This novel method is non-destructive to the nanoparticles as the extraction maintains their morphology as well as physical properties such as light absorption. We demonstrated that this method could remove the ligands in the solution in a significant level (~56.7% extraction, in the experiment with a volumetric ratio of 1:3 for the unpurified sample to the solvent). Further removal of ligands is achieved through higher extraction solvent usage or cascading of extraction. This method was also demonstrated as an in-line purification after the flow synthesis of AgNPs. About 73.3% removal of ligands was obtained during

continuous production of AgNPs. Therefore, this continuous-flow purification can potentially replace the conventional methods that are time-consuming and laborious.

In chapter 4, we built a photoreactor based on PFA tubing. we demonstrated the use of PDA and PEI for immobilizing TiO₂-P25 (P25) onto the wall of the PFA tubing. The FTIR spectra confirmed the presence of the deposited PDA and PEI, while the SEM/EDX verified the immobilization of P25. A higher density of P25 was achieved through a layer-by-layer assembly of PEI-P25, with the highest loading being 0.107 ± 0.009 mg/cm² for the five bilayers, which also gave the highest activity of 37.07% of dye decolorization at a residence time of 10 min. This simple fabrication from a commercially available tubing opens up considerable opportunities for continuous-flow photocatalytic applications.

In chapter 5, we explored a new type of photoreactor, a continuous flow flat-plate reactor to perform a photocatalytic benzene hydroxylation to phenol. A continuous flow flat-plate reactor emerges a promising option, as it allows for a large irradiation window and a short photon penetration depth. In this work, TiO₂ (Degussa P25) was applied as a photocatalyst. Use of smectite clays and a 3D-printed casting template were keys to the uniform immobilization of photocatalysts over the glass window surface. Acetonitrile was selected to be a carrier solvent for benzene since the fluid dynamics exhibited an efficient mixing with the aqueous H₂O₂ flow solution. Response surface methodology was employed to examine the effects of residence time, temperature, and light power. Our flat-plate reactor exhibited a photocatalytic space-time yield of 1.2×10^{-11} mol/W s, which is about 1-2 orders of magnitude higher than the reported batch counterparts. The transport phenomena equation was also formulated to elucidate the kinetics of the photocatalytic reaction, giving the adsorption constant and the intrinsic kinetic constant to be 0.0535 m³/mol and 8.21×10^{-6} mol/ (m².s), respectively.

ACKNOWLEDGEMENTS

I would like to express my deep gratitude to all those who have supported me throughout my Ph.D. journey. First and foremost, I am deeply grateful to my advisor, Assoc. Prof. Dr. Nopphon Weeranoppanant for his invaluable guidance, support, feedback over the past five years. Their expertise has been helped the direction and quality of this research.

I am also thankful to Prof. Richard Bourne, who served as advisor during my ten-month research stay in the UK. Additionally, I am honored to have him chair my committee.

I am also thankful to the member of my thesis committee. Prof. Suttichai Assabumrungrat, Assoc. Prof. Dr. Pailin Ngaotrakanwivat and Asst. Prof. Sareeya Bureekaew for their valuable suggestions on my research.

My sincere gratitude goes to the Royal Golden Jubilee Ph.D. Program for providing me with the financial support that made this doctoral journey possible.

I am also grateful to Department of Chemical Engineering, Faculty of Engineering, Burapha University and other supports. Thanks also go to lab members of Weeranopphanant research group for their helps, advise, and support.

Finally, I would like to express my deepest appreciate to my family for their unwavering love and support throughout my studies. In particular, I thank my sister, Petlada, and my twin brother, Chiradet, for their constant encouragement and belief in me.

Chetsada Khositanon

TABLE OF CONTENTS

	Page
ABSTRACT.....	D
ACKNOWLEDGEMENTS.....	F
TABLE OF CONTENTS.....	G
LIST OF FIGURES	9
LIST OF TABLES.....	15
CHAPTER 1	16
INTRODUCTION	16
Motivation.....	16
Research Objective	18
Scope of Research.....	18
CHAPTER 2	21
LITERATURE REVIEW	21
Metal nanoparticles.....	21
Nanoparticle purification process	26
Photocatalyst.....	28
Technical challenges in photoreactor design.....	36
Immobilization via polydopamine	42
Photocatalytic benzene oxidation to phenol	53
Application of continuous flow system for photocatalytic reaction	56
CHAPTER 3	63
CONTINUOUS-FLOW PURIFICATION OF SILVER NANOPARTICLES AND ITS INTEGRATION WITH FLOW SYNTHESIS	63
Introduction.....	63
Methods	66
Result and discussions	70
CHAPTER 4	79

A SIMPLE FABRICATION OF A CONTINUOUS-FLOW PHOTOCATALYTIC REACTOR USING DOPAMINE-ASSISTED IMMOBILIZATION ONTO A FLUOROPOLYMER TUBING	79
Introduction.....	79
Methods	81
Results and discussions.....	86
CHAPTER 5	101
CONTINUOUS FLOW PHOTOCATALYTIC BENZENE HYDROXYLATION INTO PHENOL IN A FLAT-PLATE REACTOR: DESIGN AND PROCESS OPTIMIZATION	101
Introduction.....	101
Methods	104
Results and discussions.....	108
CHAPTER 6	126
CONCLUSION.....	126
Future work.....	127
APPENDIX A.....	129
APPENDIX B	140
APPENDIX C	147
REFERENCES	152
BIOGRAPHY	175

LIST OF FIGURES

	Page
Figure 2 - 1 A diagram of the continuous diafiltration apparatus utilized The retentate reservoir is filled with the sample and the makeup solution. The peristaltic pump pushes the fluid through the diafiltration membrane (Sweeney et al., 2006).	28
Figure 2 - 2 UV-visible spectra of pure TiO ₂ and Ce-TiO ₂ (Mikaeili et al., 2018)....	29
Figure 2 - 3 Schematic diagram of during photocatalysis process on the surface photocatalyst (Kumar & Chowdhury, 2018)	30
Figure 2 - 4 The schematic represents various types of light source with direction of emitting A) Arc lamp B) Mercury vapor lamp C) LED ship (Sender & Ziegenbalg, 2017).	32
Figure 2 - 5 Drawing of an immersion well photoreactor (Lopez-Lopez et al., 2015)	33
Figure 2 - 6 Flow reactor made of FEP tube warp around medium pressure Hg lamp (Hook et al., 2005).	34
Figure 2 - 7 Multiprocess microreactor capable of mixing, extraction, and phase separation (Kralj et al., 2007).	35
Figure 2 - 8 (A) Photocatalytic spinning disc reactor, (B) Color mapping of the light intensity on a disc (Dionysiou et al., 2000).	37
Figure 2 - 9 The absorption of light of a solution with Ru(bpy) ₃ Cl ₂ is a photocatalyst with function and distance. This graph is obtained from the law of Lambert-Beer concentration $c = 0.5\text{mM}$, extinction coefficient = $13000\text{ cm}^{-1}\text{M}^{-1}$ path length l assume close to reactor wall (Su et al., 2014).....	38
Figure 2 - 10 Comparison of methylene blue degradation in (a) a microreactor and (b) a batch reactor (Wang et al., 2011).	39
Figure 2 - 11 Effect of a bulk reactant concentration and an agitation speed on the Da number. (Dionysiou et al., 2002).	40

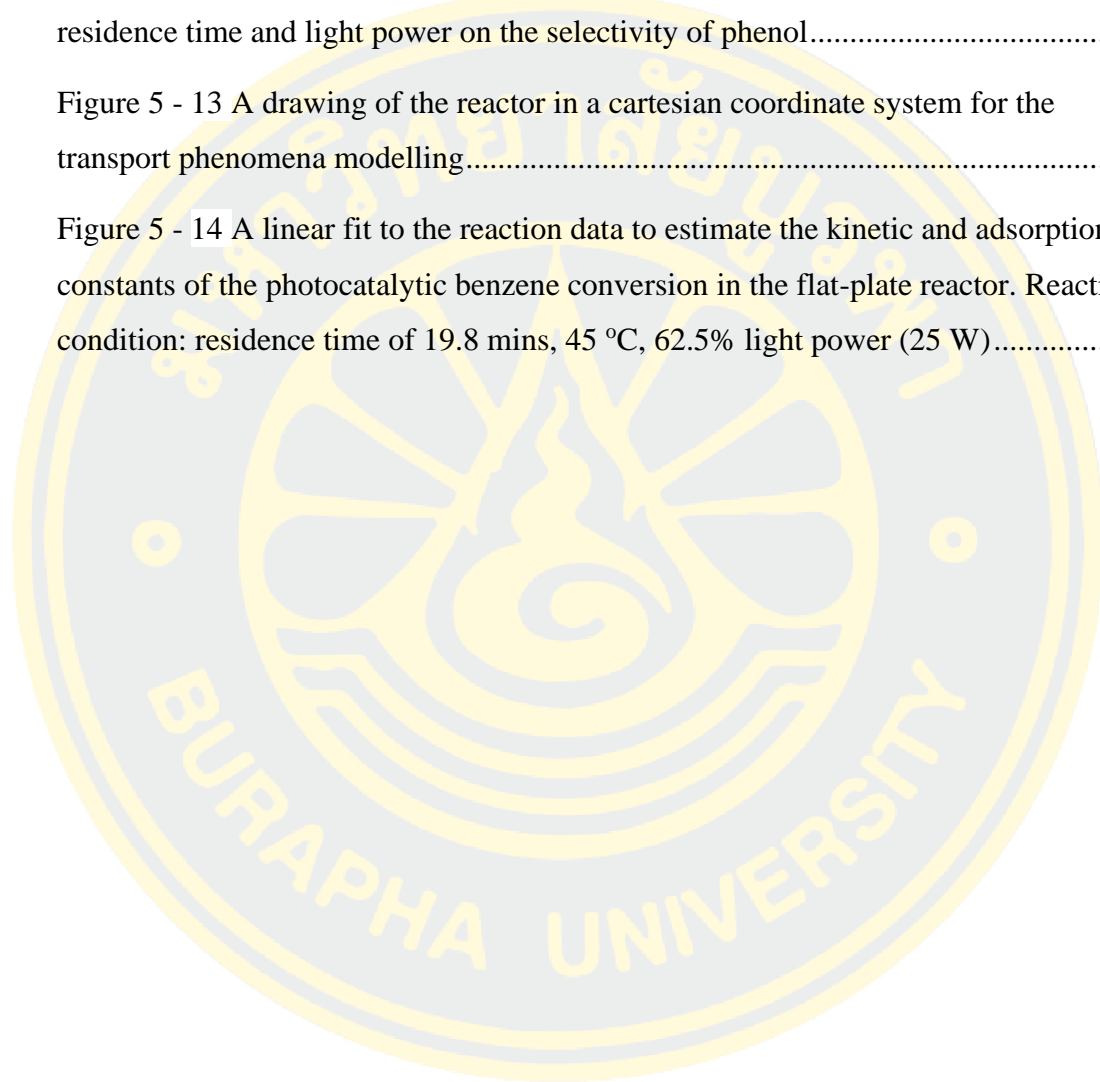
Figure 2 - 12 The process of dopamine polymerization (A) molecular of dopamine, (B) polydopamine coating method, (C) the polydopamine film thickness depended on time deposition and D) comparison XPS signal surface characterization (Lee et al., 2007).	43
Figure 2 - 13 Diagram represent (A) chemical pathway of the polydopamine formation and (B) polydopamine coating on the surface (Jiang et al., 2011).....	44
Figure 2 - 14 Scheme of the polydopamine formation (Liebscher et al., 2013; Ryu et al., 2018)	45
Figure 2 - 15 AFM images for polydopamine film roughness measurement with different reaction temperature (Jiang et al., 2011).	46
Figure 2 - 16 (A) plotting average polydopamine film thickness vs deposition time 0.1 (circle), 0.5 (black dot), 1.0 (red square), 2.0 (solid rhombus), 3.0 (open hexagons) and 5.0 (green triangle) 5mg/mL, (B) the lines correspond to fits of Equation (2-16) the maximal film thickness (black dot, left hand scale), and the rate constant (circle dash dot, right hand scale) (Ball et al., 2012)	47
Figure 2 - 17 SEM image of TFC membrane was immobilized by TiO ₂ nanoparticles on (A) without and (B) with polydopamine coating after rinsed deionized water, (C) SEM image of TFC membrane only coated with polydopamine (Zhang et al., 2013).	48
Figure 2 - 18 SEM-EDS image of TiO ₂ /polydopamine/polyurethane form at different locations on the surface (A) presence of TiO ₂ and (B) absence of TiO ₂ (Pardieu et al., 2016).	49
Figure 2 - 19(A) comparison the photocatalytic performance of TiO ₂ /polydopamine/polyurethane to degrade acid orange 7 (B) comparison percentage of reaction conversion before and after mechanical durability test (Pardieu et al., 2016).	50
Figure 2 - 20 FESEM image of β -FeOOH/polydopamine/PPNW (Zhang et al., 2015).	51

Figure 2 - 21 (A) Comparison of the catalytic performance of β -FeOOH/PDA/PPNW in methylene blue degradation in various conditions: under visible light (blue square), H_2O_2 and under visiblelight (red dot), H_2O_2 and under dark (inverted pink triangle), and β -FeOOH with H_2O_2 under visible light (orange triangle), (B) Reuse of β -FeOOH/polydopamine/PPNW for five runs (Zhang et al., 2015).	51
Figure 2 - 22 (A) The XPS spectra of PTFE, (B) After polydopamine coating, and (C) After coating PEI (Bi et al., 2017).	52
Figure 2 - 23 FESEM images of Pd/polydopamine/PTFE: (A) before reducing and (B) after reducing (Zhu et al., 2018).	53
Figure 2 - 24 Photograph of photocatalytic planar microreactor (Lei et al., 2010).	56
Figure 2 - 25 Different structures of planar microreactor (A) 1-channel, (B) 9-channel (channel wide 1 mm), (C)19-channel (channel wide 0.5 mm), and (D) the illustrate of planar microreactor (Lin et al., 2016).	57
Figure 2 - 26 (A) microreactor component, (B) SEM image of the cross section of microchannel (Gorges et al., 2004).	58
Figure 2 - 27 The photocatalytic microreactor was made of stainless steel, An experiment set up for TPA degradation (Eskandarloo et al., 2015).	58
Figure 3 - 1 Drawing to represent the two states of ligands: adsorbed and free. A purified sample may contain less ligands in both states.	64
Figure 3 - 2 The picture of the continuous-flow setup for solvent extraction of the ...	67
Figure 3 - 3 The picture of the integrated continuous-flow synthesis-purification setup	70
Figure 3 - 4 The UV-VIS absorption spectra of the samples from different purification methods	71
Figure 3 - 5 The representative TEM images of (A) the as-syn, (B) PR1, (C) SE1:1, and (D) F1:1 samples.	72
Figure 3 - 6 1H -NMR spectra of the as-syn, PR1, SE1:1, and F1:1 samples.	74

Figure 3 - 7 (A) The separated aqueous phase of the F1:1 sample, after being continuously separated from the membrane separator, (B) The mixture of the SE1:1 after mixing for 1 h. It required a significant amount of time for the mixture to separate into clear phases.....	75
Figure 3 - 8 Rate constants of the 4-NP degradation, using the AgNPs samples from different purification methods as catalysts	76
Figure 3 - 9 The UV-VIS absorption spectra of the as-syn_in flow and F1:3_in flow samples that were produced in the integrated continuous-flow synthesis-purification setup	77
Figure 4 - 1 A flow cell embedding a PFA flat sheet for validating our immobilization protocol.....	82
Figure 4 - 2 Schematic of the immobilization protocol for preparing the photocatalytic tubular reactor	85
Figure 4 - 3 Setup for a continuous-flow photocatalytic reaction	86
Figure 4 - 4 Appearance of a bare PFA and a “PEI-P25 _{5L} @PDA” sample.....	87
Figure 4 - 5 Transmission FTIR spectra of the surface-modified PFA sheets.....	88
Figure 4 - 6 SEM images of the surface-modified PFA sheets and EDX mapping with Ti atoms	89
Figure 4 - 7 Absorbances of different prepared samples	90
Figure 4 - 8 Possible mechanism of (A) PDA and PEI depositions and (B) layer-by-layer immobilization of P25.....	91
Figure 4 - 9 (A) Photos of the bare and coating PFA tubing (PEI-P25 _{5L} @PDA sample), (B) A cross-sectional SEM image showing a thickness of the deposition layers (PEI-P25 _{5L} @PDA sample).....	92
Figure 4 - 10 (A) Photocatalytic activity of different prepared tubings, (B) Photolysis and adsorption tests to validate the photocatalytic activity of the prepared tubing. The experimental condition: a tubular reactor setup, 10-min residence time and 0.0500 mM methylene blue	94

Figure 4 - 11 The effects of (A) inlet methylene blue concentrations and (B) light intensities on photocatalytic activity, as represented by percent decolorization. The maximum power of the light source is 10 W.....	95
Figure 4 - 12 A representative linear fit was to estimate the kinetic and adsorption parameters from the gradient and intercept.	100
Figure 5 - 1 Mechanism of benzene hydroxylation into phenol via radical formation from H ₂ O ₂	103
Figure 5 - 2 Three configurations of a photocatalytic flat-plate reactor: (A) Photocatalysts as suspensions, (B) Photocatalysts immobilized onto the reactor's surface, (C) Photocatalysts immobilized onto the glazing window.....	103
Figure 5 - 3 (A) Components of the flat-plate reactor assembly, (B) UV LED panel.	106
Figure 5 - 4 (A) LED irradiating the flat-plate reactor, (B) Setup of the continuous flow photocatalytic hydroxylation of benzene.....	107
Figure 5 - 5 (A) Images of the TiO ₂ suspensions with and without the smectite clay additions after 24 h of settling, (B) Image of the TiO ₂ layer on the glass surface with and without the template.....	109
Figure 5 - 6 (A) SEM image of the TiO ₂ layer with the clay addition and the use of the template, (B) the cross-section SEM image of the TiO ₂ showed a uniform layer thickness of 1.38 – 1.57 μm.....	110
Figure 5 - 7 The simulation result in terms of the mixing index at different initial mesh levels (1 – 7).....	111
Figure 5 - 8 The mixing index at the centerline along the length of the reactor.....	111
Figure 5 - 9 The progress of reaction over the time course of benzene concentration.....	112
Figure 5 - 10 The progress of reaction over the time course of phenol concentration.....	113

- Figure 5 - 11 Three-dimensional response surface plot for the effects of temperature, residence time and light power on the conversion of the benzene hydroxylation to phenol..... 117
- Figure 5 - 12 Three-dimensional response surface plot for the effects of temperature, residence time and light power on the selectivity of phenol..... 118
- Figure 5 - 13 A drawing of the reactor in a cartesian coordinate system for the transport phenomena modelling..... 120
- Figure 5 - 14 A linear fit to the reaction data to estimate the kinetic and adsorption constants of the photocatalytic benzene conversion in the flat-plate reactor. Reaction condition: residence time of 19.8 mins, 45 °C, 62.5% light power (25 W)..... 123



LIST OF TABLES

	Page
Table 2 - 1 Features of common light sources for photochemical applications (Su et al., 2014)	32
Table 2 - 2 Comparison kappa number of different photoreactor configurations (Van Gerven et al., 2007).....	36
Table 2 - 3 Comparison water contact angle on polymer films before and after dopamine coating (Jiang et al., 2011)	46
Table 2 - 4 Comparison of difference type of microreactor and with difference reaction model.....	60
Table 3 - 1 The measured wavelength at maximum absorbance (λ_{\max}) and full width at half maximum (FWHM) of AgNPs from different purification methods.....	71
Table 3 - 2 The calculated % SDS removal of different purification methods.....	74
Table 4 - 1 Specific densities of P25 of different immobilized tubular samples as estimated from the ICP-OES measurement.....	92
Table 4 - 2 Definitions of dimensionless numbers	97
Table 5 - 1 Five levels of values for each variable according to CCD.....	106
Table 5 - 2 Percentage benzene conversion and phenol selectivity at different feeding benzene to H ₂ O ₂ ratios. Reaction condition: residence time of 30 mins, 25 °C, 40 W light power	113
Table 5 - 3 ANOVA results of the percentage benzene conversion and phenol selectivity (A = Residence time, B = Temperature, C = Percent light power)	115
Table 5 - 4 Dimensionless parameters for the formulation of the transport phenomena inside the flat-plate reactor.....	121
Table 5 - 5 Comparison of the photocatalytic benzene hydroxylation in different setups, particularly in terms of the PSTY	125

CHAPTER 1

INTRODUCTION

Motivation

Continuous flow systems are widely used in chemical engineering application, such as organic synthesis, inorganic material synthesis, photochemical reactions, electrochemical reactions, and biocatalytic reactions. These systems are designed to handle a continuous stream of inputs, allowing for a constant and continuous process of chemical reactions. Unlike batch processing, where materials are added in batches and the entire batch must be processed before new materials can be added.

In addition to improving quality and productivity, continuous flow systems also offer benefits when it comes to safety and cost-effectiveness. The steady-state conditions allow for better control over the reaction parameters, leading to improved safety and reduced risk of accidents. Furthermore, the nature of continuous flow system often results in lower energy and raw material consumption, making them a more sustainable and cost-effective option for many chemical engineering applications.

In this thesis, we focus on two applications of the continuous flow systems: nanoparticle synthesis and photochemical reaction, both of which are relevant to the heterogenous catalysis.

In the third chapter, we establish a continuous flow system for purifying silver nanoparticles and integrating it with flow synthesis. The synthesis of silver nanoparticles presents challenges, as it typically involves a metallic precursor, a reducing agent, and capping ligands. While these capping ligands are crucial in controlling the growth and stabilization of the nanoparticles, they are often added excessively. This results in an excess of adsorbed ligands on the nanoparticle's surface as well as free ligands in the solution, which can negatively impact catalytic performance by restricting access to the nanoparticle's surface and causing detrimental effects. Traditional purification methods like multiple washing or precipitation-redissolution aim to remove these impurities but can be time-consuming and present various challenges. To address this issue efficiently without compromising their

catalytic activity and physical properties, our research focuses on developing continuous flow purification techniques for silver nanoparticles in an aqueous solution.

In the fourth chapter, we develop a photocatalytic flow reactor using fluoropolymer tubing, which is beneficial due to its transparency, availability, and affordability. However, the high hydrophobicity and chemical inertness of fluoropolymers make it difficult to coat them with photocatalysts. We successfully developed a protocol to immobilize photocatalysts, specifically titanium dioxide (P25), on the inner wall of a perfluoroalkoxy alkane (PFA) tubing. This was achieved by first depositing layers of polydopamine and polyethyleneimine to the tubing to facilitate the coating. The photocatalyst loading was maximized via a layer-by-layer assembly, resulting in enhanced photocatalytic activity. The reactor we created demonstrated the continuous-flow operation for the decolorization of methylene blue with minimal loss in photocatalyst activity over time and negligible leaching, showing the potential for practical photocatalytic applications

In the fifth chapter, we improve photocatalytic systems, by exploring a new type of reactors. The motivation of this work, phenol is typically produced through the cumene process. The cumene process has drawbacks including multiple reactive steps, high energy consumption, and use of aggressive chemicals. Alternatively, benzene hydroxylation can be achieved using photocatalysis with homogeneous and heterogeneous catalysts. This thesis merges continuous flow system with heterogeneous photocatalysis in a temperature-controlled flat-plate reactor to perform a photocatalytic benzene hydroxylation to phenol.

Despite their difference in reaction characteristics, the examples demonstrated throughout this thesis were relevant to heterogeneous catalysis, which can be used in forms of suspension (chapter 3) or immobilized catalysts (chapter 4 and 5)

Research Objective

1. To construct and perform a continuous-flow synthesis of silver nanoparticles integrated with in-line purification.
2. To develop a simple fabrication protocol for the PFA tube-based photocatalytic reactor using dopamine-assisted immobilizations of photocatalysts and perform continuous-flow photocatalytic dye degradation.
3. To construct a flat-plate reactor and develop a continuous-flow photocatalytic benzene hydroxylation into phenol.

Scope of Research

Project 1 (Refer to Chapter 3)

1. Process parameters to purify silver nanoparticle:
 - 1.1. Independent variable: purification method, including precipitation, batchwise solvent extraction and continuous-flow solvent extraction
 - 1.2. Precipitation method: microcentrifugation at 13,000 rpm at 25 °C for 20 mins
 - 1.3. Solvent extraction:
 - 1.3.1. As-synthesis to ethyl acetate ratio: 1:1 and 1:3
 - 1.4. Characterization of silver nanoparticles:
 - 1.4.1. Absorption: UV-VIS spectrometer
 - 1.4.2. Surface morphology: TEM
 - 1.4.3. Catalyst loading: ICP-OES
 - 1.4.4. Sample purity: $^1\text{H-NMR}$
2. Testing catalytic performance
 - 2.1. Independent variable studied: silver nanoparticles from differences purification methods.
 - 2.2. Reaction model: 4-nitrophenol degradation (0.05 mM)
 - 2.3. Sodium borohydride: 0.02 M, 1.5 mL
 - 2.4. Silver nanoparticle sample: 20 μL
 - 2.5. Characterization: UV-VIS spectrometer absorbance at 400 nm

Project 2 (Refer to Chapter 4)

1. Immobilization of photocatalysts onto PFA was studied based on following basis:
 - 1.1. Support: PFA sheet thickness 25 μm , PFA tube OD 1/8" and ID 1/16"
 - 1.2. Immobilization method: layer-by-layer, electrostatic immobilization agent
 - 1.3. Scale of immobilization: 0.02- 0.1 mL/min (laboratory scale)
 - 1.4. Process parameters to be studied:
 - 1.4.1. Number of layers: 1, 3 and 5 layers
 - 1.5. Characterization of immobilized materials
 - 1.5.1. Catalyst loading: ICP-OEX
 - 1.5.2. Catalyst film absorption: UV-VIS spectrometer
 - 1.5.3. Measurement light intensity: photometer
 - 1.5.4. Observation of surface morphology of coated PFA sheet: SEM-EDS
 - 1.5.5. Functional group on the surface of coated PFA sheet: FT-IR
2. Implementation of immobilized PFA tube into a flow reactor for continuous methylene blue degradation:
 - 2.1. Support: PFA tube (volume 1.75 mL)
 - 2.2. Independent variable studied:
 - 2.2.1. Number of coated layer of catalysts: 1, 3 and 5 layers
 - 2.2.2. Methylene blue concentration: 0.00625 – 0.05 mM
 - 2.2.3. % Light power (10 W maximum): 20 – 100 %
 - 2.2.4. Scale of study: 0.5 – 1 mL/min (laboratory scale)
 - 2.3. Characterization:
 - 2.3.1. Methylene blue concentration: UV-VIS spectrometer

Project 3 (Refer to Chapter 5)

1. Process parameters to immobilize photocatalyst on glass plate:
 - 1.1. Support: borosilicate glass
 - 1.2. Immobilization method: dropwise
 - 1.3. Characterization of immobilized glass plate
 - 1.3.1. Catalyst loading: ICP-OES

- 1.3.2. Light transmission of immobilized glass plate: photometer
- 1.3.3. Observation of catalyst film on glass plate: SEM-EDX
2. Implementation of immobilized glass plate into film reactor for continuous benzene hydroxylation:
 - 2.1. Independent variable studied:
 - 2.1.1. % Light power (40 W maximum): 40 – 100 %
 - 2.1.2. Process temperature: 30 – 60%
 - 2.1.3. Residence time: 30 – 60 mins
 - 2.2. Reactor volume: 2.25 mL (laboratory scale)
 - 2.3. Characterization benzene concentration and products: HPLC analysis.
Study reactor mixing performance: SolidWorks flow simulation

CHAPTER 2

LITERATURE REVIEW

In this literature study, we concentrated on three major areas, as relevant to the work developed in this thesis. First, we consider metal nanoparticles, including their synthesis, applications, and purification procedure. Second, we consider the fundamentals of heterogeneous photocatalysts, their applications, and the immobilization process. Third, we consider phenol synthesis and the possibility of using a continuous flow photocatalyst system for phenol's hydroxylation from benzene.

Metal nanoparticles

Metal nanoparticles are small particles, generally less than 100 nanometers in size, made up of metal atoms. Because of nano size, they have distinct physical and chemical properties compared to bulk material of same metal. These properties include high surface area, unique optical features, enhanced reactivity, and electrical conductivity (Astruc, 2020). Metal nanoparticles possess these qualities, making them applicable in wide range of areas including catalysis (Alam & Shon, 2021), electronics (Gracias et al., 2000), environmental remediation (Daghrir et al., 2013; Jo & Tayade, 2014), drug delivery and diagnostics in medicine (Chandrakala et al., 2022; Constantinou et al., 2022; Luo et al., 2024), as well as materials science research (Kundu & Patra, 2017).

There are various methods for preparing metallic nanoparticles. Commonly divided into two main groups: bottom-up and top-down. Bottom-up methods for the preparation of metallic nanoparticles involve synthesizing nanoparticles from smaller molecules or atoms, gradually building up to larger structures (You et al., 2013). These methods include chemical reduction, sol - gel, and hydrothermal (Jamkhande et al., 2019). On the other hand, top-down methods involve the breaking down of larger materials into nanoparticles. Some examples of top-down methods include grinding (Qiao et al., 2011).

The bottom-up approach to nanoparticle synthesis involves the production of nanoparticles from molecules, such as the combining of atoms, or molecules. In this

approach, nanostructured building block or the nanoparticles are first created and then combined to make the final nanoparticles(Vinnacombe-Willson et al., 2023).

1. Gas phase synthesis

1.1. Spray pyrolysis

Spray pyrolysis involves creating aerosol droplets from a precursor solution and then heating them to a high temperature, which leads to the formation of nanoparticles(Guild et al., 2014; Jung et al., 2010). To start the process, a precursor solution containing metal salts dissolved in an appropriate solvent is prepared. This solution is then atomized into tiny droplets, often using an atomizer like an ultrasonic nozzle. These droplets are carried through a reactor chamber or furnace by a carrier gas. In the reactor, the droplets undergo solvent evaporation followed by high-temperature breakdown and oxidation of the residual solute. The end result of this procedure is solid metal oxide nanoparticles, typically spherical in shape.

Spray pyrolysis is can be used to synthesis mixed metal oxide nanoparticles. For example, Maric et al. (2000) created spherical, nanoparticles with controllable morphology by using spray pyrolysis techniques to create ceramic powders straight from solutions. This technique produces powders with mixed oxide compositions that are intended for use as electrode materials in solar organic fuel cells (SOFCs), highlighting the significance of microstructure control for effective electrodes.

1.2. Flame pyrolysis

flame pyrolysis is similar to spray pyrolysis but it achieved by the direct spraying of a liquid precursor into the flame. This method can be used to deliver precursors in the form of vapor if their vapor pressure is not high enough. Gases, liquid, or solid precursors are exposed to the flame and given time to create nanoparticles in vapor-fed aerosol flame synthesis (Mädler et al., 2002; Wallace et al., 2013).

This method can be used to control particle size, composition, and morphology, as well as the scalability of the process. It is mostly used for synthesizing metal oxide nanoparticles(Jossen, 2006; Teoh, 2013; Teoh et al., 2010). for instance, by maximising the impact of precursor concentration, dispersion gas flow rate, and power production rate on the size and carbon content of the synthesised particle. The exact practice size is controllable (Mueller et al., 2003). Tani et al. (2002) used this method to synthesized homogenous zinc oxide nanoparticles by adjusting the solution feed rate during the

process, the average primary particle diameter of the zinc oxide can be controlled, range from 10 -20 nm.

2. Liquid state synthesis methods

2.1. Sol-gel methods

The Sol-Gel method is a widely used technique for producing metal oxide nanoparticles. This technique involves the transition of a system from a liquid “sol” (mostly colloidal) into a solid “gel” phase (Hench & West, 1990; Livage et al., 1988). There are simply three steps, hydrolysis and condensation: metal alkoxides or metal chlorides are used as precursors. it undergoes hydrolysis and polycondensation reaction to form a sol, which is a dispersion of nanoparticles in a liquid. Gelation process, upon further condensation, the sol transforms into a gel, which is a three-dimensional network encapsulation liquid within its pores. During gelation process, the liquid in the gel is removed through a drying process, often accompanied by further heat treatment, which leads to the formation of an amorphous or partially crystalline oxide network. Final process, additional heat treatment (calcination) is typically employed to remove any remaining organic components and to initiate the transformation of the amorphous oxide into a crystalline structure (Singh et al., 2014; Trewyn et al., 2007).

The Sol-Gel method has the ability to produce materials with high purity, homogeneity at relatively low temperatures (Macwan et al., 2011) and it can be used to formed thin film metal or metal oxide on a substate (Sonawane & Dongare, 2006; Ward & Ko, 1995; Znaidi, 2010). The drawback is that it can be a complex process requiring precise control over the reaction conditions, and it might involve lengthy aging times of the gel. The sol -gel method process is sensitive to factors such temperature, pH and drying conditions and deviations in these parameters can significantly affects the final nanoparticle characteristics (Parashar et al., 2020).

2.2. Hydrothermal method

The hydrothermal method involves the reaction of aqueous solution vapors with solid material at high pressure and temperature within a sealed vessel. This process leads to the deposition of small particles (Tavakoli et al., 2007). A precursor material is mixed in an aqueous solution and placed in a sealed vessel, often referred to as an autoclave. Next, the sealed vessel is subjected to high temperatures and pressures. The precise temperature and pressure condition depend on the desired characteristics of the nanoparticles (Tavakoli et al., 2007). Under these circumstances, the precursors' solubility and reactivity increase, allowing them to react and produce particles in the polymeric hydroxide form (Tavakoli et al., 2007). After dehydrating, these hydroxides become crystalline metal oxide nanoparticles. This process produces well-crystallized powder, which has a well-defined and ordered structure and improves the material's strength, durability, or catalytic performance depending on the application (Burda et al., 2005).

2.3. Chemical reduction

The chemical reduction method is a common technique used to synthesize metal nanoparticle. It involves the reduction of metal ions to metal atoms by a reducing agent in a liquid medium. The chemical reduction method includes the following steps, a metal's ionic salt is reduced in an appropriate medium. The various reducing agents are used such as sodium borohydride, glucose, ethylene glycol, ethanol, citrate of sodium, and hydrazine hydrate, among others (Cushing et al., 2004). Sodium borohydride is commonly used in an aqueous solution to prepare metal nanoparticle. To prevent the agglomeration of the formed nanoparticles and to stabilize them in the dispersion, capping agents like trisodium citrate or surfactants such as sodium lauryl sulphate may be added (Cushing et al., 2004).

The advantages of this method include simplicity and the possibility to control the size and morphology of the particles with continuous flow system by adjusting flow rate (Roberts et al., 2019). However, drawbacks include potential toxicity issues with some reducing agents used. The likelihood of impurities (Park et al., 2009; Wu et al., 2014), and limitations associated with the reducing agents' efficiency (Cushing et al., 2004). Application includes the preparation of various metal nanoparticles, such as silver, copper or gold nanoparticles (Panigrahi et al., 2004).

3. Solid state methods

3.1. Physical vapor deposition (PVD)

This technique used to deposit thin films of material onto a substrate or base material. This process occurs in a vacuum and involves vaporizing a solid material, which then condenses onto the substrates, forming a thin film (Gondoni et al., 2013). The source material, which could be a pure metal, is vaporized using techniques such as thermal evaporation or sputtering. The vaporized atoms or molecules travel through a vacuum toward the substrate. The vapor condenses on the substrate, forming a thin film whose properties can be controlled by adjusting the deposition parameters. Key physical vapor deposition techniques include sputtered deposition, where material is ejected from a target by ionized gas molecules and thermal evaporation, where material is heated until it sublimates (Pandey et al., 2011).

3.2. Chemical vapor deposition (CVD)

Chemical Vapor Deposition is a process utilized to produce high-purity, high-performance solid materials. Unlike Physical Vapor Deposition, CVD relies on chemical reactions between gaseous precursors and the substrate surface to deposit material in the form of a thin film (Pedersen & Elliott, 2014). It does not require as high a vacuum as physical vapor deposition because the process is based on chemical reactions that can occur at various pressures. CVD can yield high-quality, high-performance solid materials commonly used for wear-resistant coatings, semiconductors, and optics (Reina et al., 2009).

The applications of CVC range from producing films and coatings for semiconductors and optical devices to manufacturing wear-resistant coatings. It's also employed in synthesizing carbon nanotubes and graphene (Reina et al., 2009). Advantages of CVC include its relatively high deposition rate and ability to uniformly coat complex-shaped substrates (Vallejos et al., 2016). However, careful control of temperature, pressure, and chemical reactions are essential due potential toxicity or hazards associated with some precursors used in this process (Jamkhande et al., 2019). There could be significant costs involved in setting up this equipment making large-scale production less efficient compared other techniques (Ren & Cheng, 2014).

Nanoparticle purification process

The general method for removing ligands in the liquid phase is precipitation-redissolution, commonly used in laboratory settings. After centrifugation, excess ligands and other impurities can be retained in the supernatant while the nanoparticles are precipitated. The precipitated nanoparticles are then redissolved to undergo another two or three washing cycles. However, this method can affect the surface properties of nanoparticles due to strong g-force, leading to particle aggregation.

Shah et al. (2020) comparing two nanoparticle purification methods between centrifugation and TFF (tangential flow filtration), using acetalated dextran nanoparticles as a case study. The study aimed to explore the impact of TFF flow rate, transmembrane pressure, and initial drug loading on NP characteristics using a design of experiment approach. This some keys points of the advantages of TFF over centrifugation. TFF utilizes a dynamic filtration process where nanoparticle suspensions flow tangentially to the membrane, which helps reduce the potential for nanoparticle agglomeration. TFF allows for size-based separation, as the membrane used in TFF can retain nanoparticles larger than a certain size threshold, offering controlled purification. Flow systems can be more easily scaled up for manufacturing processes compared to centrifugation which is limited by centrifuge container sizes. Centrifugation can inadvertently alter nanoparticle properties due to high g-forces and difficulties in redispersing nanoparticle pellets. TFF avoids this issue through its mode of operation. They suggested that TFF offers a gentler and more controllable means of nanoparticle purification, which can result in more consistent quality and potentially higher purity of the final nanoparticle product.

There are many methods that used to purify nanoparticle in liquid phase such as filtration (Alele et al., 2016), dialysis (Alkilany et al., 2014), gel permeation chromatography solvent extraction (Shen et al., 2016)

Hollamby et al. (2010) presented a new method for the separation, purification, and recovery of high-value gold and silver nanoparticles. This method involves synthesizing nanoparticles in a supporting cetyltrimethylammonium bromide-stabilized water-in-oil microemulsion. Upon the addition of excess water to these microemulsions, a phase separation is induced that results in a strong preferential partitioning of the nanoparticles into an upper coexisting phase. The purified

nanoparticles can then be dried by removing the solvent and redispersed in other solvents, like pure octane. The described purification method has several advantages over existing techniques. It doesn't require additional organic solvents, operates with a low energy demand, and does not necessitate specialist surfactants or fine temperature control. Water is utilized as a green solvent, and surfactants may be collected and reused after purification, showing that the process is ecologically beneficial.

Shen et al. (2016) demonstrated that even in anhydrous solvents, GPC is efficient in separating colloidal nanoparticles from small molecules without the need for precipitation. This is useful when working with delicate samples in an atmosphere devoid of air. They employed GPC purification to track variations in quantum yield resulting from the removal and reintroduction of neutral ligands on the surface of CdSe/CdS quantum dots. Utilizing the ongoing removal of native ligands as the QDs passed down the column, they also investigated the use of GPC to promote ligand exchange with tiny and macromolecular ligands. They were able to study the kinetics of weakly and firmly bound ligands using this method. They also showed that GPC can regularly carry out several tasks in a single run, which may be useful for industrial uses such quick prototyping, discovery, and optimization of nanocrystal surface reactions.

Sweeney et al. (2006) discusses diafiltration for purifying gold nanoparticles base on size. They used diafiltration (Figure 2-1) utilizes a cross-flow mechanism that pushes a solution through a membrane, allowing smaller particles and impurities to pass, while retaining larger particles. It's particularly suited for dealing with water-soluble nanoparticles, where it can effectively remove small-molecule impurities and separate nanoparticles into groups of uniform size. This is essential for obtaining highly pure and monodisperse nanoparticle samples. Their study demonstrated that diafiltration could purify thiol-stabilized 3-nm gold nanoparticles more effectively than traditional methods. Tools like NMR, thermogravimetric analysis, and X-ray photoelectron spectroscopy underscored the high purity of the nanoparticles post-diafiltration.

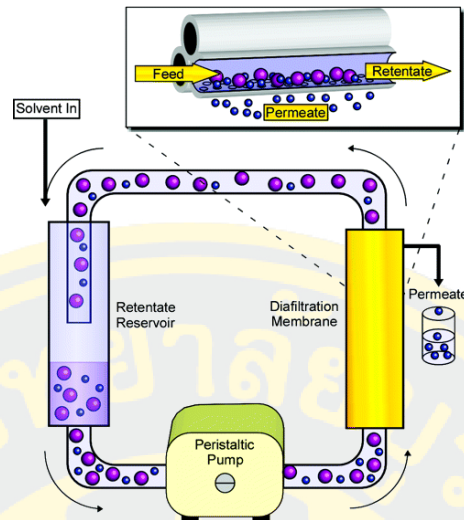


Figure 2 - 1 A diagram of the continuous diafiltration apparatus utilized. The retentate reservoir is filled with the sample and the makeup solution. The peristaltic pump pushes the fluid through the diafiltration membrane (Sweeney et al., 2006).

Photocatalyst

When photocatalyst are stimulated by light that has enough or more energy than the its band gap, the photocatalyst will create a free electron and a hole. Different photocatalysts will create different electron-hole pairs. Some of the photocatalysts can be activated in the visible light range. It gains popularity in recent years because it is a stable, harmless, and recyclable material that can be operated at mild condition (Bhatkhande et al., 2002).

1. Mechanism of photocatalysis

Most of photocatalyst involves semiconductor elements. It works on the principle of band gap energy. When projected with light that have enough energy, the photocatalyst will generate the electron-hole pair (Sudha & Sivakumar, 2015). The band gap energy can be estimated by Equation (2-1) (Mikaeili et al., 2018):

$$E_g = \frac{1240}{\lambda} \quad (2-1)$$

Where E_g is band gap energy, λ is the absorption edge wavelength in the spectra which obtained from UV-visible spectrometer for example in Figure 2-2 show the UV-visible spectra of pure TiO_2 and Ce-TiO_2 . The absorption edge wavelength is the wavelength which dash line draw along the curve and cut X axis. So, the absorption edge wavelength of TiO_2 and Ce-TiO_2 are approximately 405 nm and 510 nm, band gap energy is 3.06 eV and 2.43 eV, respectively. This mean that if photocatalyst has an absorption edge wavelength at UV spectrum region it will request higher energy than in Visible spectrum region.

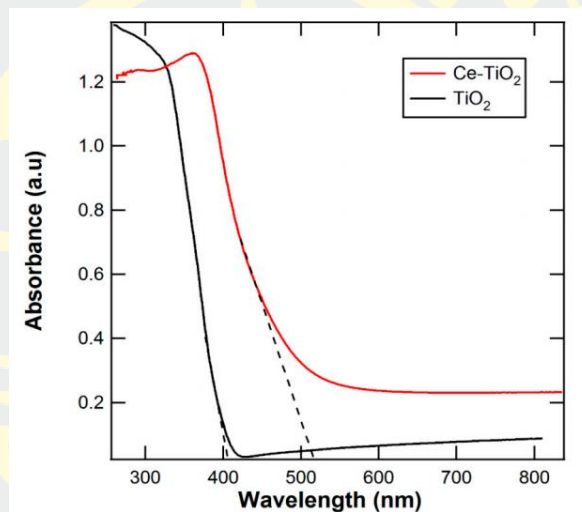
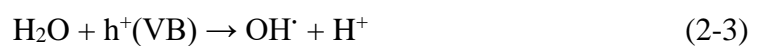
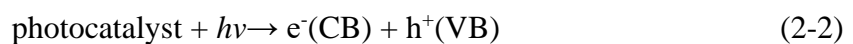


Figure 2 - 2 UV-visible spectra of pure TiO_2 and Ce-TiO_2 (Mikaeili et al., 2018)

When photocatalyst gains enough energy, an electron-hole pair will be generated. It can be summarized with a following set of chemical equations (Kumar & Chowdhury, 2018) and Figure 2-3



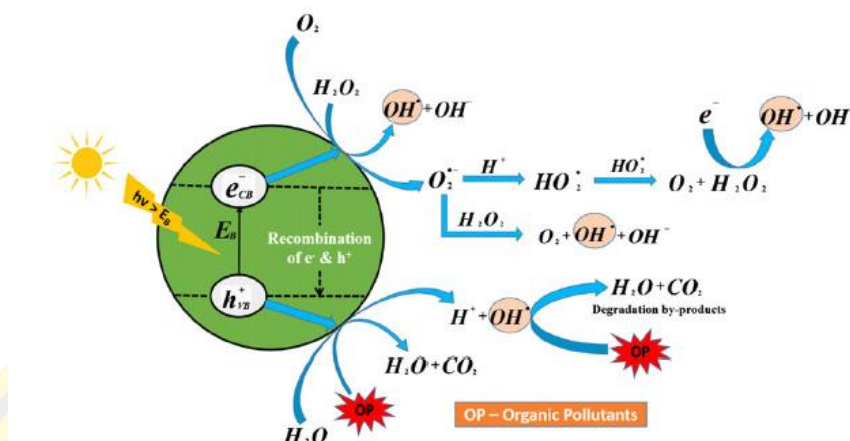


Figure 2 - 3 Schematic diagram of during photocatalysis process on the surface photocatalyst (Kumar & Chowdhury, 2018)

2. Photocatalytic reactor design considerations

To perform a photocatalytic reaction, a photoreactor is required. It is important to note that, throughout our discussion, the terms “the photocatalytic reactor” and “the photoreactor” will be used interchangeably. There are a number of design considerations for the photoreactor. The important considerations are light sources, solvents, reactor materials, and reactor configuration. There are also different light sources that can be employed, ranging from a UV lamp to sunlight. Currently, a number of researches are looking into utilization of direct sunlight. However, sunlight still has some limitations such as low portion of usable UV light (3-4%) (Bora & Mewada, 2017) and inconsistent intensity throughout a day. A choice of solvent is critical as different solvents are capable of absorbing lights in different wavelengths. The following subsection will be presented with these design considerations. The reactor materials must also allow the light to pass through and not to cause light scattering.

3. Selection of light sources

The light sources that have been used for photochemistry are commonly artificial such as arc lamp and fluorescent lamps. Depending on the continuity of the light output, artificial light sources can be categorized into three types: (a) a continuous, polychromatic spectrum, (b) a discrete, polychromatic spectrum, and (c) a narrow-band monochromatic spectrum (Sender & Ziegenbalg, 2017).

For the continuous, polychromatic spectrum, the light sources used are incandescence lamps, halogen lamps, Xenon arc lamps, standard and compact fluorescence lamps. In general, a light filter is required to specify a wavelength to be projected into the reaction so that side reactions and degradation of desired products can be prevented (Lu et al., 2001). The lamp can be in different forms including a globe bulb or a tubular bulb. In the case of radial radiation, a mirror can be installed to control the wavelength.

For the discrete polychromatic spectrum, the light sources used are mercury vapor lamps. They will emit UV light depending on the pressure of mercury vapor. They have similar applications to the continuous one. There are three types of the mercury vapor lamps: low pressure, medium pressure and high pressure. Commonly, the low and medium pressure ones are used since they last longer, and have a higher efficiency than the high pressure one (Sender & Ziegenbalg, 2017).

For the narrow-band monochromatic spectrum, the most common type is light-emitting diodes (LEDs). LEDs work on the principle of the semiconductor type PN junction. They have a very narrow energy band gap, about 20 nm. Therefore, they are particularly useful for photochemistry as a certain wavelength can be defined. LEDs are also advantageous in that they are small, highly efficient, and generate low amount of heat.

Sunlight is a natural source, considered as clean energy. In the past, it has been used for water treatment and air purification. Recently, they have been developments to use sunlight for photochemistry. Table 2-1 summarizes the features of different light sources.

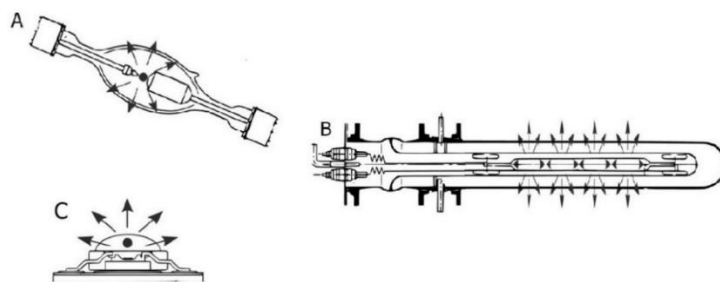


Figure 2 - 4 The schematic represents various types of light source with direction of emitting A) Arc lamp B) Mercury vapor lamp C) LED chip (Sender & Ziegenbalg, 2017).

Table 2 - 1 Features of common light sources for photochemical applications (Su et al., 2014)

Light source	Emission wavelength [nm]	Note
Low pressure Hg arc	>90 % emission at 254 nm, small fraction at 185 nm, mostly absorbed by glass ware	
Medium pressure Hg arc	prominent emission lines 313, 366, 405, 550 nm	10 times intensity than low pressure Hg
High pressure Hg arc	Continuous between 360-600 nm	expensive, short life time
Xenon arc	broadband spectrum continuous between 390-800 nm	expensive, high temperature
Black light	360 nm	cheap
Lasers	discrete wavelengths	high intensity
UV-LEDs	400 nm and down to 310-320 nm	Low-energy input, long lifetime, expensive, compatible with microreactors
Vis-LEDs	Variety of wavelengths between 400–700 nm	low-energy input, long lifetime, cheap, compatible with microreactors

4. Selection of reactor materials

The photoreactor can be made of different materials including polymer and glass. The reactor can be made light-transmitting either completely or partially. In this section, we focus on the materials for a light-transmitting side of the reactor. Glass is widely used due to its high transparency and high chemical compatibility. For better light transmission, quartz can be used for an operation with visible and UV regions, up to 170 nm. Pyrex, Corex, and Vycal allow lights with a wavelength that is longer than 275, 260, 220 nm, respectively. The glass reactor is typically demonstrated in batch, alternatively known as an immersion well photoreactor as depicted in Figure 2-5. The batch reactor comes with a cooling system to reduce heats from the lamp and control a reaction temperature.

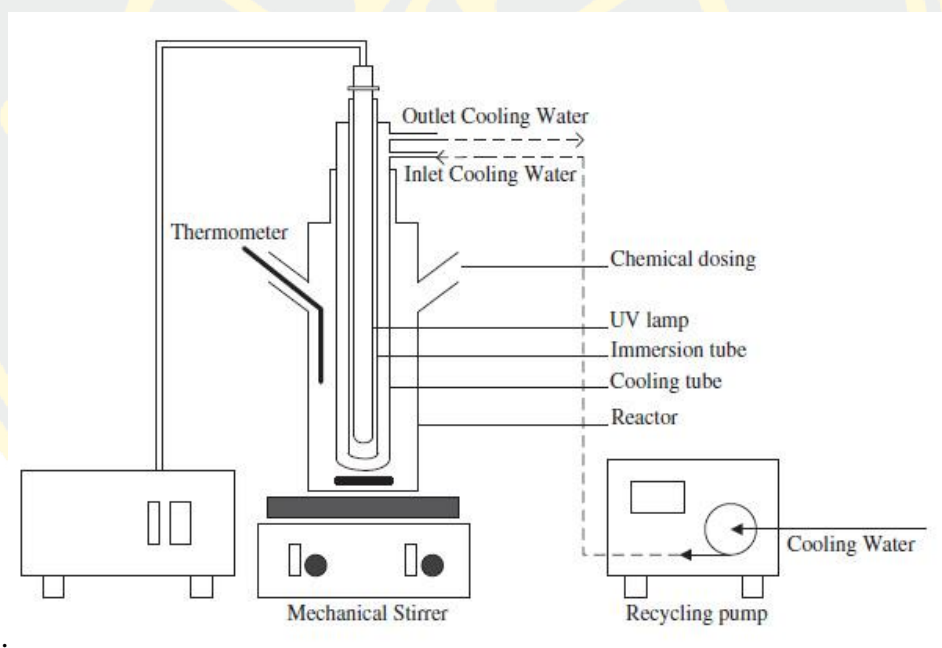


Figure 2 - 5 Drawing of an immersion well photoreactor (Lopez-Lopez et al., 2015)

Nowadays, there are many research groups try to reduce the energy consumption, time and system by applying the microfluidic technology to fabricate microreactor. If it is a plug-flow reactor, it is used as a glass tube, or if it is microreactor type, it can be done by using microcapillaries tubes or machining the glass substrate into small channel and bonding together. Microcapillary reactors are mainly used for

rapid chemical reaction to attain high conversion and yield. (Jolliffe & Gerogiorgis, 2015). Yen et al. (2003) recently study the synthesis of nanocrystal of CdSe colloidal in Microcapillary reactor which consisting of a heated glass reaction capillary and a convective mixer.

Polymer is alternative material which have been used to fabricate microreactor. Polymer exhibit several advantages including cheap, ease of fabrication and elastic flexibility property. There are many types of polymers such as polyvinyl chloride (PVC), polystyrene (PS), polycarbonate (PC), polyimide (PI), olefin-based polymer Poly(methyl methacrylate) (PMMA), Polydimethylsiloxane (PDMS). Perfluoroalkoxy alkanes (PFA) and Fluorinated ethylene propylene (FEP) such as Hook et al. (Hook et al., 2005) used FEP tube which warped around medium pressure UV-lamp as showed in Figure 2-6, Azouz et al. fabricated microreactor which made of olefin copolymer (Azouz et al., 2014), Kucuk et al. used microreactor which made of PMMA to synthesize polymer nanosphere (Kucuk & Edirisinghe, 2014).

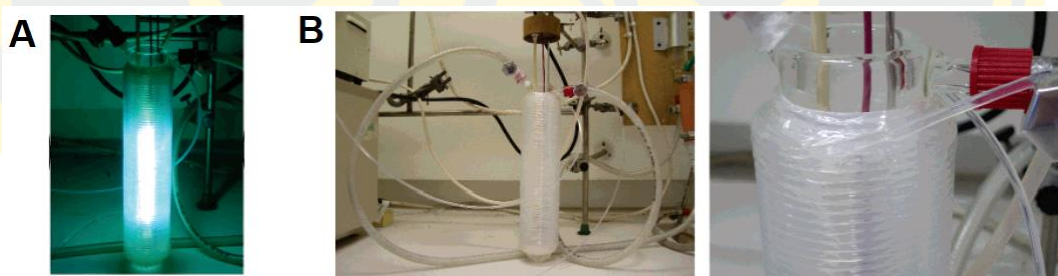


Figure 2 - 6 Flow reactor made of FEP tube warp around medium pressure Hg lamp (Hook et al., 2005).

PDMS is the most commonly used material for fabrication of microreactor because it can be easily molded from the microscale molding process. However, PDMS are not resistant to organic solvent and cannot withstand at high temperature, will easily slip off. They can only be used in some applications in which they are compatible, but PFA and FEP materials are highly flexible and can withstand acid and alkaline solvent at high temperatures and high pressures. Also, PFA and FEP have excellent light transmission properties. PFA allows visible light in the wavelength in range 400-700

nm pass through 91-96% and allows UV light in the wavelength range 250-400 nm, can pass 71-96%. FEP for visible is the same as PFA, but UV light is slightly better than PFA (Su et al., 2014).

Silicon is another material for the microreactor. Although silicon is widely used in the microelectronic chip industry, it has applied for the fabrication of the microreactor just over the last decade. It has been implemented for multiphase flow systems. Kralj et al. fabricated a microreactor in Figure 2-7 to perform a liquid-phase reaction that integrated laminar mixing, hydrodynamic aiming, rapid heat transfer, and temperature controlling (Kralj et al., 2007).

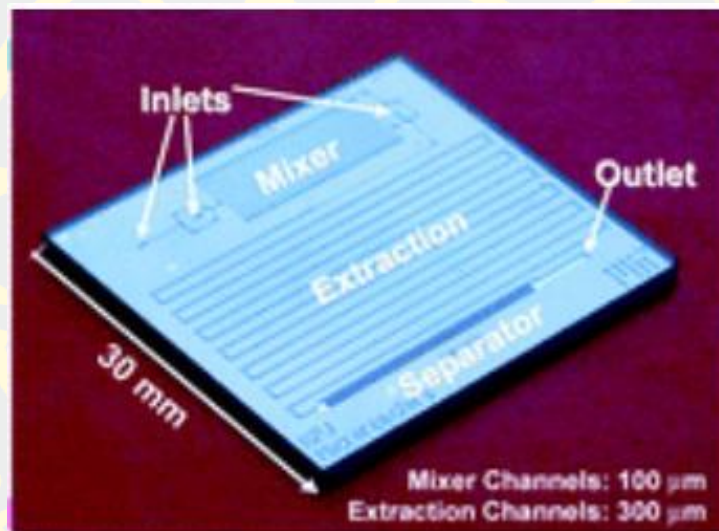


Figure 2 - 7 Multiprocess microreactor capable of mixing, extraction, and phase separation (Kralj et al., 2007).

Technical challenges in photoreactor design

During the photoreactor design, we may encounter two main challenges: photon and mass transfer limitations. The photon transfer will affect photon utilization, which may also result in lower reaction activity. The mass transfer specifically refers to mixing of different components, which can also affect a reaction yield.

1. Photon transfer limitation

To evaluate the extent of the photon transfer in a system, we can examine different process variables. For instance, we can look at a kappa (κ) number, which represents an amount of surface area being irradiated per a reaction volume (unit: $\text{m}^2 \text{m}^{-3}$). Different photoreactor configurations have significantly different κ numbers, as shown in Table 2-2. Microreactor has a high value of κ when compared to other reactors.

Table 2 - 2 Comparison kappa number of different photoreactor configurations (Van Gerven et al., 2007)

Reactor type	<i>kappa number</i>	References
Slurry reactor	2,631	(Mukherjee & Ray, 1999)
	8,500–170,000	(Augugliaro et al., 1997)
Monolith reactor	943	(Sauer & Ollis, 1994)
	1,333	(Lin & Valsaraj, 2005)
Spinning disc reactor	50-130	(Dionysiou et al., 2000)
Microreactor	7,300	(Van Gerven et al., 2007)
	12,000	(Gorges et al., 2004)
	250,000	(Takei et al., 2005)

Different photoreactor configurations may also experience different light uniformity. As an example, Dionysiou et al. (2000) measured the light intensity from two low-pressure mercury UV tubes in the spinning disc reactor as shown in Figure 2-8 with TiO_2 coated on the disc surface. From the measurement, we observed that the light

intensity was non-uniform, widely distributed between 30 and 1500 $\mu\text{W}/\text{cm}^2$. The average value of the light intensity was 895 $\mu\text{W}/\text{cm}^2$ (Dionysiou et al., 2000).

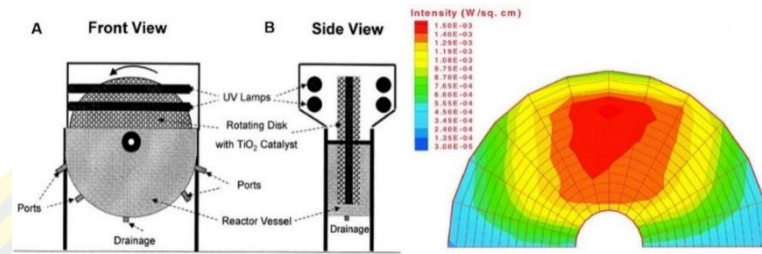


Figure 2 - 8 (A) Photocatalytic spinning disc reactor, (B) Color mapping of the light intensity on a disc (Dionysiou et al., 2000).

The average light energy emitted from the light source is depended on two parameters. First. The average of light intensity is inversely proportional to the distance between the lamp and the catalyst surface squared. Calculated from the Equation (2-2):

$$H_c = \frac{P_{lamp}}{l^2} \quad (2-2)$$

Where H_c is the average of light which irradiate on catalyst surface (Wm^{-2}), P_{lamp} is the emitted radiant power of lamp (W), and l is the distance from lamp to catalyst surface. Second, Light can be absorbed before it reaches the catalyst surface. This appears to be explained by the Lambert-Beer law, according to the Equation (2-3):

$$\log_{10} \frac{P_0}{P} = \epsilon lc \quad (2-3)$$

Where P_0 is the radiant power before absorption (W), P is the radiant power after absorption (W), ϵ is the molar absorptivity of the absorbing species ($\text{mol}^{-1}\text{m}^{-1}$), l is thickness of the material containing (m), and c is the concentration of the absorbing species (mol^{-1})

In order for light to reach the surface of the catalyst, it is absorbed by various media, the reactant air and the glass wall, and, moreover, difficult to make the uniformity of light intensity throughout the reactor.

Su et al. (2014) has shown that the light transmission is reduced by more than 50% when irradiated through a solution containing $\text{Ru}(\text{bpy})_3\text{Cl}_2$ as a catalyst in the 0.5mm depth range as showed in Figure 2-9.

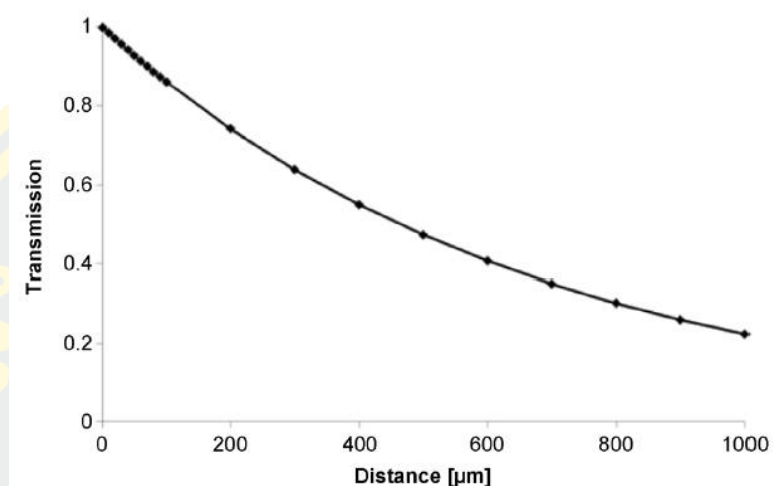


Figure 2 - 9 The absorption of light of a solution with $\text{Ru}(\text{bpy})_3\text{Cl}_2$ is a photocatalyst with function and distance. This graph is obtained from the law of Lambert-Beer concentration $c = 0.5\text{mM}$, extinction coefficient $= 13000 \text{ cm}^{-1}\text{M}^{-1}$ path length l assume close to reactor wall (Su et al., 2014)

2. Mass transfer limitation

Photocatalytic reaction is normally regarded as heterogeneous as the photocatalyst is typically insoluble solid. To achieve a high reaction yield, the catalyst needs to have well contact with a chemical species in the solution. The mass transfer efficiency can be improved by designing the reactor to have a larger contact area between the photocatalyst and the reactant.

Wang et al. (2011). showed the performance photocatalytic degradation of methylene blue in a batch reactor and a microreactor. The two reactors have different levels of mixing. The microreactor has a shorter length scale, which is beneficial for both the photon and mass transfers. As shown in Figure 2-10, using the reaction volume of 3 mL and dye concentration of 0.03 mM, they found that the microreactor achieved 50% degradation at 60 seconds while the batch reactor required more than 40 minutes to obtain the same 50% degradation.

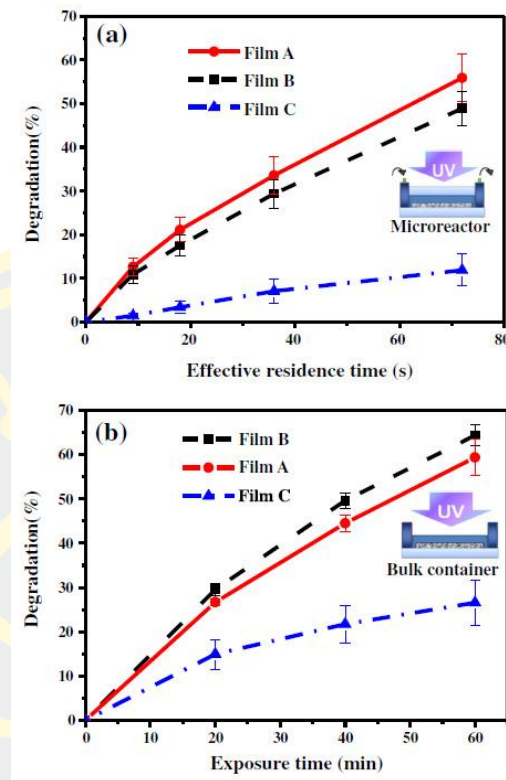


Figure 2 - 10 Comparison of methylene blue degradation in (a) a microreactor and (b) a batch reactor (Wang et al., 2011).

A dimensionless number can be used to provide some insight about the effect of mass transfer. For example, for the photocatalytic reaction that happens at the surface of the photocatalyst, Da , Damköhler number, can be evaluated. The Damköhler number, is a dimensionless ratio between the apparent reaction kinetics and the mass transfer rate. There are two barriers during the mass transfer. The first barrier occurs in a liquid film around the photocatalyst. The subsequent barrier is adsorption-desorption to the photocatalyst surface. The Damköhler number can be described in Equation (2-4):

$$Da = \frac{k_r}{k_{ma}a/K_{ads} + k_{ma}aC_b} \quad (2-4)$$

k_{ma} is the mass transfer coefficient, a is the interfacial area per unit volume of the immobilized catalytic film which can be calculated with BET surface, k_r is the reaction rate constant, and K_{ads} is absorption-desorption equilibrium constant which can be obtain for experiment.

To interpret the Damköhler number, we can see if the number is very low or very high. If $Da \ll 1$, the intrinsic reaction rate is a limiting step. In this case, further improvement in the mixing will not enhance the apparent rate. On the other hand, the process is limited by the mass transfer if $Da \gg 1$.

Dionysiou et al. has shown (Figure 2-11) the effect of Da number in the rotor disc photocatalytic reactor. They found that when they increased the angular velocity of the disc from 0 to 20 rpm, the Da number decreased significantly, meaning that that mass transfer coefficient was improved (Dionysiou et al., 2002). The effect was especially true for the low concentration of the reactant. At a higher concentration, this effect became less noticeable due to the high concentration gradient.

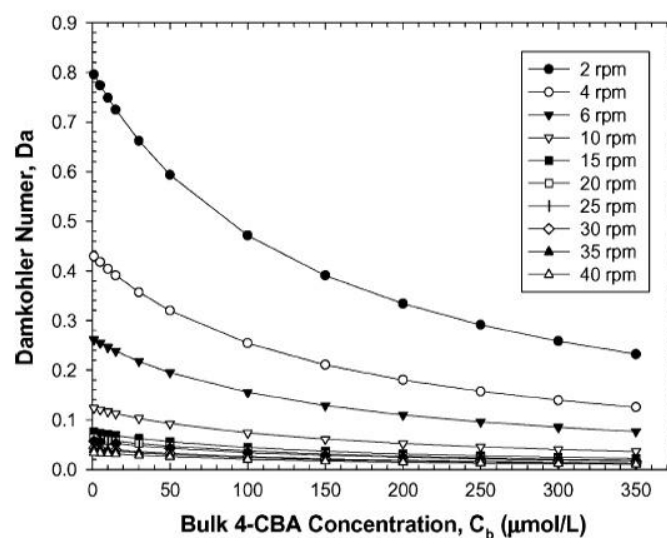


Figure 2 - 11 Effect of a bulk reactant concentration and an agitation speed on the Da number. (Dionysiou et al., 2002).

3. Kinetics of photocatalytic reactions

In heterogeneous photocatalyst system, the reaction rate constant is explained by the Equation (2-5) of Langmuir-Hinshelwood (L-H) kinetics. The L-H model work on following basic assumptions (Fox & Dulay, 1993) 1) at the equilibrium state the number of surface site is still remain 2) only one substrate in the system or non-competitive adsorption for the same surface site 3) The adsorption rate at the surface site is higher than the chemical rate reaction 4) No blocking of active site by product.

$$r = \frac{k_r K_{ads} C}{1 + K_{ads} C} \quad (2-5)$$

Where k_r is the reaction rate constant ($\text{mgL}^{-1} \text{min}^{-1}$), K_{ads} is absorption-desorption equilibrium constant or Langmuir constant of the pollutant molecule on the catalyst surface (L mg^{-1}) and C is the concentration of the reactant. The initial rate of a reaction as function of initial concentration C_0 can be given by Equation (2-6):

$$r_0 = \frac{k_r K_{ads} C_0}{1 + K_{ads} C_0} \quad (2-6)$$

The value of k_r and K_{ads} can be obtained from linearizing following Equation (2-7):

$$\frac{1}{r_0} = \frac{1}{k_r} + \frac{1}{k_r K_{ads} C_0} \quad (2-7)$$

The linearity of a plot of $1/r_0$ versus $1/C_0$ for testing the validation of the L-H model, where $1/k_r$ can be obtain as the Y-intercept and $1/k_r K_{ads}$ is the slope.

When integrating the Equation (2-7) between the boundary condition $C = C_0$ at time $t = 0$ and $C = C$ at $t = t$, we will get Equation (2-8):

$$\ln\left(\frac{C_0}{C}\right) + K_{ads}(C_0 - C) = k_r K_{ads} t \quad (2-8)$$

If the value of $K_{ads} C \ll 1$ when integrating Equation (2-7) again at the same boundary condition. We will get the following equation:

$$-\ln\left(\frac{C}{C_0}\right) = k_{app}t \quad (2-9)$$

Equation 2-9 is called the first order rate constant which can be used when the concentration of pollutant is very low (mM). Where k_{app} is apparent rate constant, $k_{app} = k_r K_{ads}$.

Immobilization via polydopamine

Catalyst can be immobilized onto solid supports via many techniques such as encapsulation (Akiyama & Kobayashi, 2009), entrapment (Avnir et al., 1994), electrostatic interaction (McMorn & Hutchings, 2004), and covalent binding (Brühwiler, 2010). Over the past decade, use of dopamine has received considerable attention for surface engineering, particularly to increase hydrophilic properties to help catalyst immobilization.

1. Polydopamine and its mechanism

Lee et al. first demonstrated that dopamine (Figure 2-12 (A)) allow deposition on various substrates such as stainless steel, glass, polymer film, and PTFE. A thin film of polydopamine is formed by simply immersing the substrate into a dopamine solution at pH ~ 8.5 as shown in Figure 2-12 (B). In Figure 2-12 (D) dash red bars are original signal substrates and solid red bars are signal substrates after polydopamine coating. The blue dot represents a signal of nitrogen and carbon ratio after the polydopamine coating. The signal ratio of 0.1 to 0.13 in most substrates was similar to the dopamine's characteristic ratio of 0.125. This means that the substrates were not affected by the polydopamine layer (Lee et al., 2007). Although this study could not provide conclusions about the mechanism.

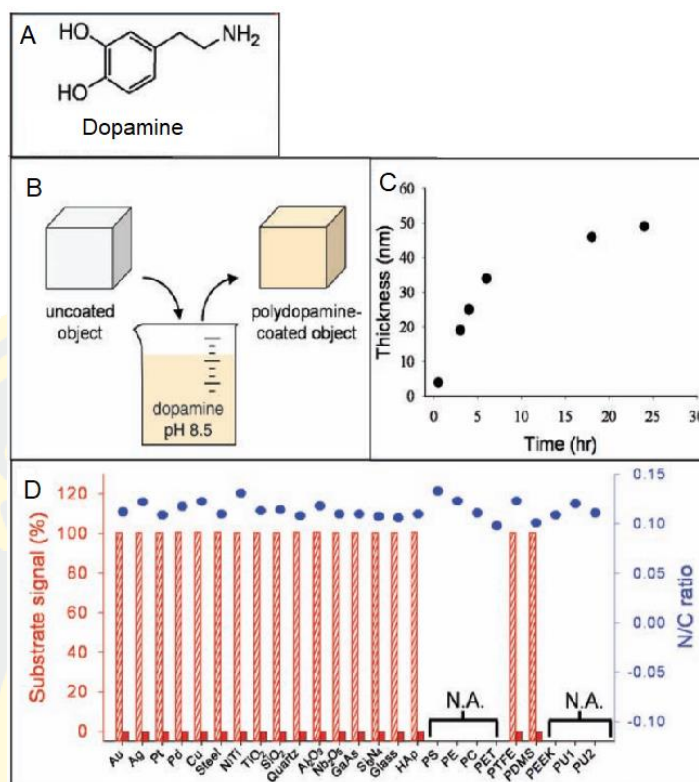


Figure 2 - 12 The process of dopamine polymerization (A) molecular of dopamine, (B) polydopamine coating method, (C) the polydopamine film thickness depended on time deposition and D) comparison XPS signal surface characterization (Lee et al., 2007).

To understand its formation mechanism, Jiang et al. has shown that the polymerization happened as dopamine was oxidized to quinone in presence of oxygen. The quinone molecule went through cyclization and rearrangement. The final product is 5,6-dihydroxyindole and 5,6-indolequinone at position 2, 3, 4 and 7 in these molecules is able to react each other to produce oligomer and assembly through Pi-Pi stacking to form nanoaggregates and form a polymer film on the surface substrate (Jiang et al., 2011) as show in Figure 2-13.

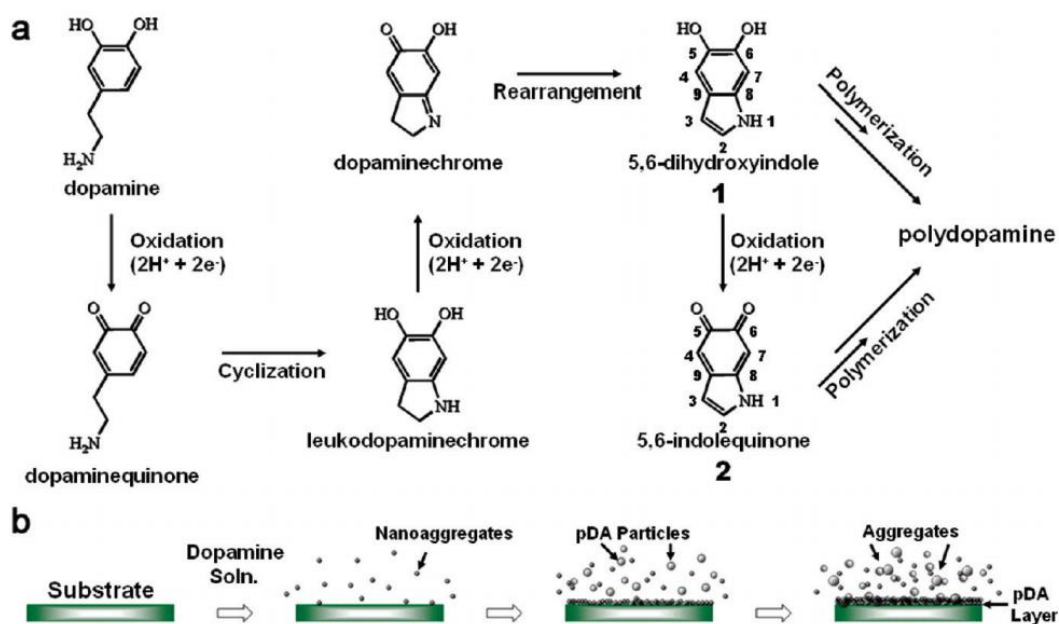


Figure 2 - 13 Diagram represent (A) chemical pathway of the polydopamine formation and (B) polydopamine coating on the surface (Jiang et al., 2011).

In line with the previous studies, Liebscher et al. used ^{13}C cross-polarization polarization–inversion magic angle spinning NMR (CPPI MAS NMR), magic angle spinning NMR (^1H MAS NMR), electrospray ionization high-resolution mass spectrometry (ES-HRMS) to observe structural changes (Liebscher et al., 2013). They found that dopamine can convert to quinone in presence of oxygen. The quinone can proceed further to form a heteropolymer. Alternatively, quinone may go through cyclization to form,6-dihydroxyindole which further polymerize to a eumelanin-like material as show in Figure 2-14.

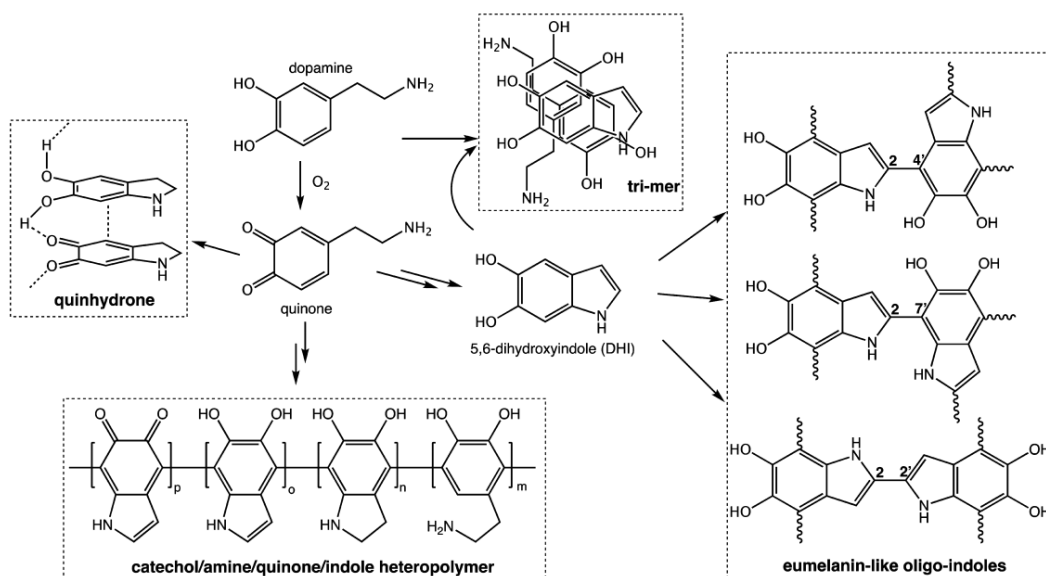


Figure 2 - 14 Scheme of the polydopamine formation (Liebscher et al., 2013; Ryu et al., 2018)

As mentioned earlier, polydopamine coating works in various types of substrates, including hydrophobic polymer, which is in general difficult to modify. In 2011, Jinhong Jiang et al demonstrated polydopamine coating in four types of polymer: polyethylene (PE), poly(vinylidene fluoride) (PVDF), polytetrafluoroethylene (PTFE). Using a general protocol (immersion of the film in Tri-base 10 mM pH 8.5 for 24 hours). As shown in Table 2-3, water contact angle decreased, meaning that the film had become more hydrophilic. The roughness was affected by the temperature. With increasing temperature, the film became rougher as shown in Figure 2-15.

Table 2 - 3 Comparison water contact angle on polymer films before and after dopamine coating (Jiang et al., 2011)

Polymer film	Before	After
PTFE	124.2±0.8	81.3±2.3
PVDF	91.6±2.6	54.8±3.4
PI	82.0±0.7	64.9±1.2
PET	85.8±1.5	59.8±2.8

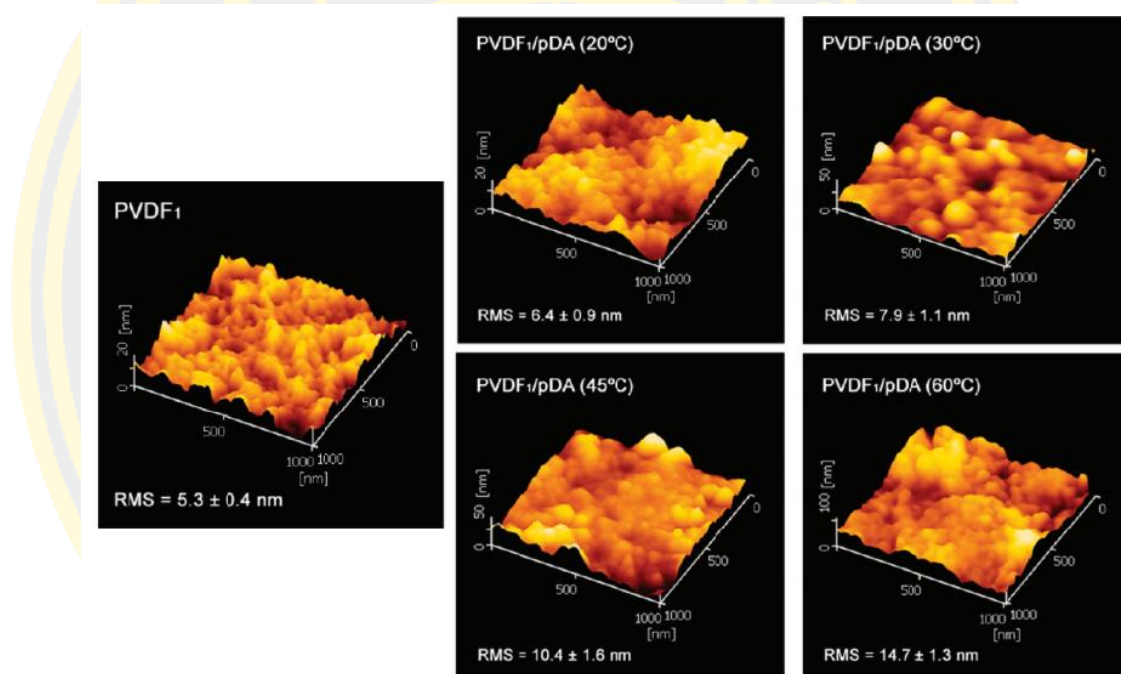


Figure 2 - 15 AFM images for polydopamine film roughness measurement with different reaction temperature (Jiang et al., 2011).

Ball et al. (2012) studied the kinetics of the polydopamine film as a function of dopamine concentration. The kinetics data was presented in term of the film thickness over time. As in Figure 2-16, the higher the concentration of the dopamine solution, the thicker the coating. Upon the 5 mg/ml solution, the film thickness reached about 85 nm. However, at the higher dopamine concentration, it required longer time to reach steady state. At 0.5, 1.0, and 2.0 mg/ml concentrations, the steady-state thicknesses were 20,

25 and 35 nm, respectively. They also proposed a kinetic equation as shown in Equation (2-16):

$$\frac{d d(t)}{dt} = d_{max}k(e^{-kt}) \quad (2-10)$$

d_{max} is a maximal polydopamine film thickness from AFM analysis, $d(t)$ is a polydopamine film thickness at time point t , and k is a kinetic constant. In Figure 2-16 (B), although d_{max} was greatly a function of dopamine concentration, the kinetic constant k depended on the concentration only at very low concentration (less than 1 mg/ml).

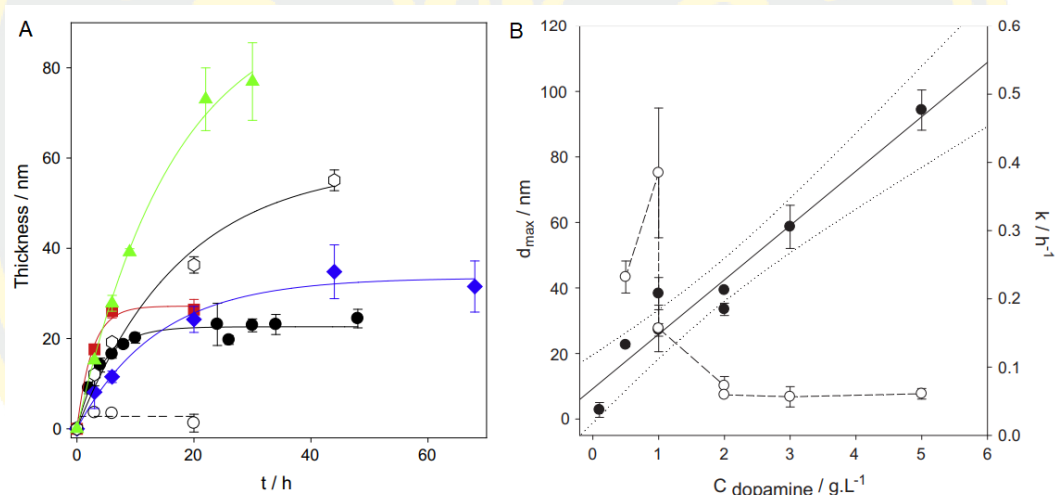


Figure 2 - 16 (A) plotting average polydopamine film thickness vs deposition time 0.1 (circle), 0.5 (black dot), 1.0 (red square), 2.0 (solid rhombus), 3.0 (open hexagons) and 5.0 (green triangle) 5mg/mL, (B) the lines correspond to fits of Equation (2-16) the maximal film thickness (black dot, left hand scale), and the rate constant (circle dash dot, right hand scale) (Ball et al., 2012)

2. Polydopamine layer as catalyst immobilization

Polydopamine has recently emerged as a technique for catalyst immobilization onto different substrates. Zhang et al. studied a simple method to binding TiO_2 nanoparticles (anatase, < 25 nm, 99.7%) on a thin film composite (TFC) membrane,

which was made of polyether sulfone, a non-woven fabric, and methyl-2-pyrrolidone. To bind TiO_2 with the TFC membrane, they first deposited polydopamine on the TFC membrane by mounting in a dead-end cell and poured the dopamine solution (2 mg/ml in Tris-base 10 mM pH 8.5) through the cell for 2 h. The TFC was rinsed with deionized water and dried with compressed air for 5 min. The TFC membrane was then mounted in a dead-end cell, and immersed in the TiO_2 suspension of nanoparticles (0.1 % w/v). They observed surface morphologies of TFC membrane with SEM analysis as show in Figure 2-17, polydopamine film act as a good adhesive layer between TiO_2 nanoparticles and TFC membrane even rinsed with water 2 h (Zhang et al., 2013). Although this research did not perform a photocatalytic reaction, it demonstrated that TiO_2 can be easily immobilized on a TFC membrane through a polydopamine layer.

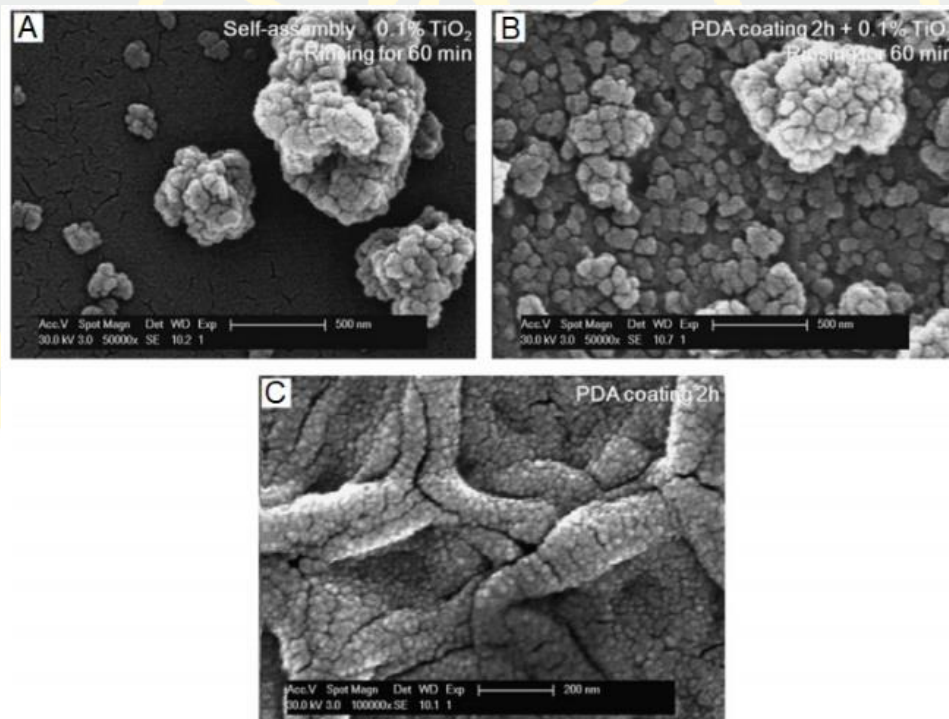


Figure 2 - 17 SEM image of TFC membrane was immobilized by TiO_2 nanoparticles on (A) without and (B) with polydopamine coating after rinsed deionized water, (C) SEM image of TFC membrane only coated with polydopamine (Zhang et al., 2013).

Pardieu et al. (2016) demonstrated a simple way to immobilize TiO₂ nanoparticles (anatase, 10 nm) on a commercial polyurethane foam. Polyurethane foam was cut in cubic shape with 0.5×2×2 cm, then immersed in dopamine solution for 12 h. To immobilize TiO₂ nanoparticle, polyurethane foam was immersed in aqueous solution of TiO₂ concentration 2%w/v for 12 h at 40°C with active stirring. In Figure 2-18, SEM-EDS was used to examine a surface component after coating with polydopamine and TiO₂ nanoparticles. The SEM-EDS indicated presence of the Ti element, but it was not uniformly distributed. The average Ti content was evaluated by inductively coupled plasma-optic emission spectrometry by revealing 607±80 mg/kg. Photocatalytic performance of TiO₂/PDA/polyurethane was tested by degradation of acid orange 7 (acid orange 7 solution 28.5 μM 40 mL has placed in a UV irradiation chamber 125 W). As shown in Figure 2-19, the sample with TiO₂ clearly performed in superior to other samples. The degradation performance was even maintained after the mechanical compression test.

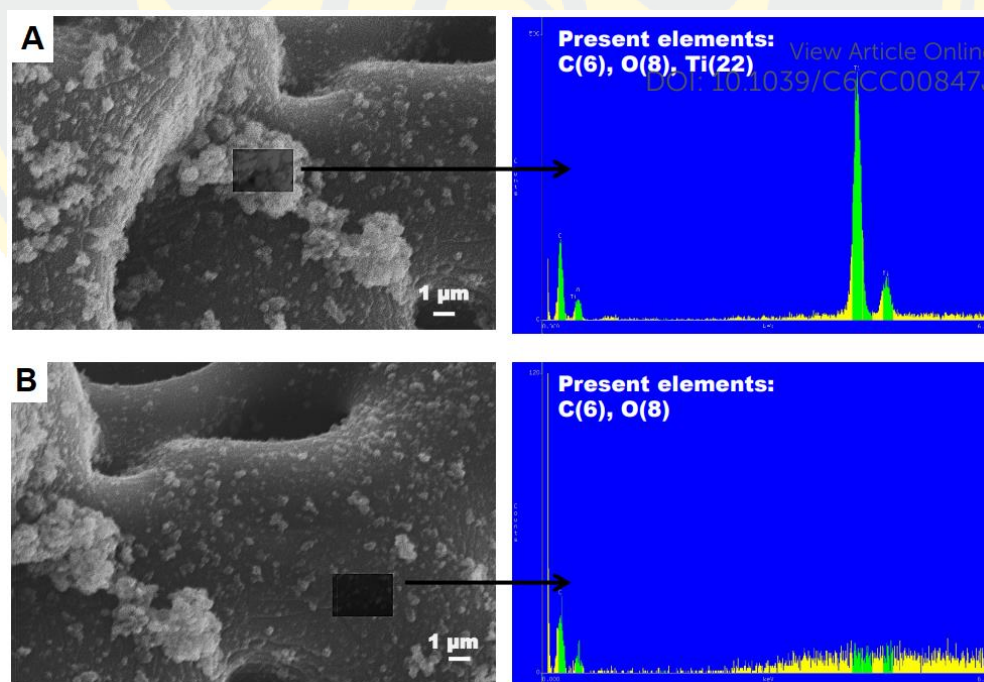


Figure 2 - 18 SEM-EDS image of TiO₂/polydopamine/polyurethane form at different locations on the surface (A) presence of TiO₂ and (B) absence of TiO₂ (Pardieu et al., 2016).

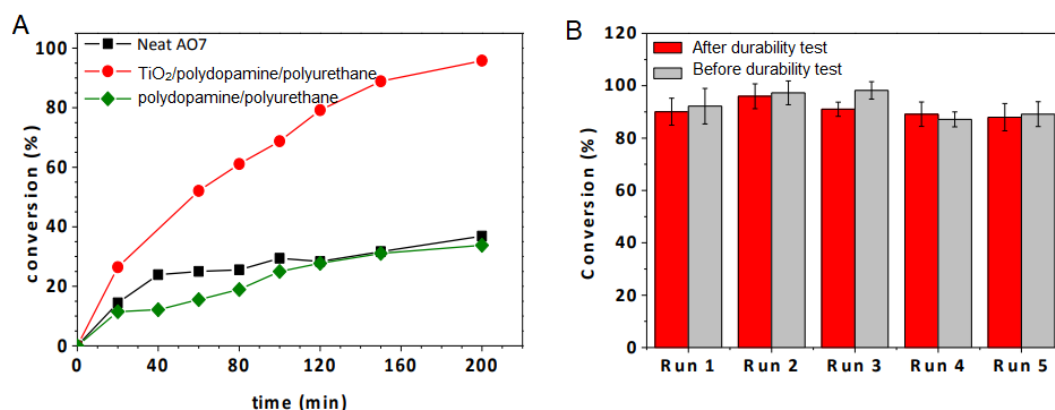


Figure 2 - 19(A) comparison the photocatalytic performance of TiO₂/polydopamine/polyurethane to degrade acid orange 7 (B) comparison percentage of reaction conversion before and after mechanical durability test (Pardieu et al., 2016).

Zhang et al. (2015) immobilized β -FeOOH nanorods on porous substrate, was made of polypropylene non-woven (PPNW). They used that this substrate to degrade various dyes including methyl blue, methylene blue, rhodamine B, and methyl orange under visible light (500 W Xe lamp which equipped cut-off filter of 420 nm). After coating with polydopamine, the membrane was immersed in a mixed solution of FeCl₃ 6H₂O (0.067 M, 20 ml) and HCL (0.01 M, 10 mL) at 60° for 24 h. In Figure 2-20, a FESEM image of β -FeOOH nanorods on polydopamine /PPNW was shown. The β -FeOOH nanorods appeared to be uniformly distributed on the porous substrate surface. The performance of β -FeOOH/polydopamine/PPNW in photocatalytic methylene blue degradation (20 mg/L methylene blue, pH 3, and H₂O₂ 9.8 mM, visible light) was close to 100% in 60 min, as shown in Figure 2-21.

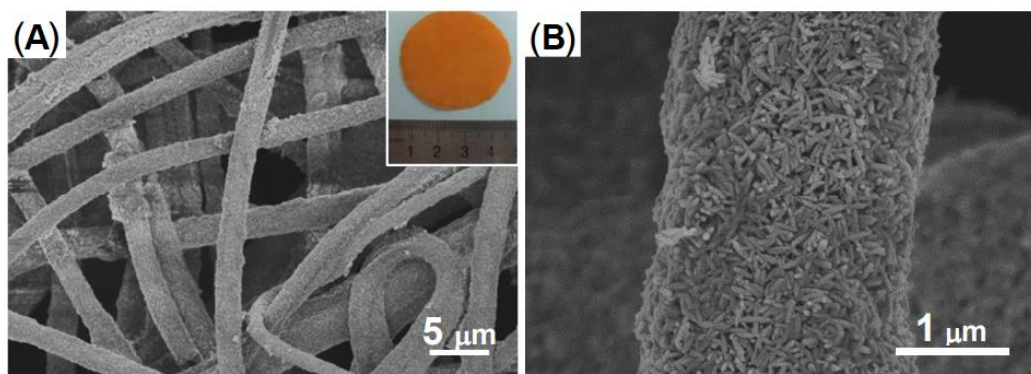


Figure 2 - 20 FESEM image of β -FeOOH/polydopamine/PPNW (Zhang et al., 2015).

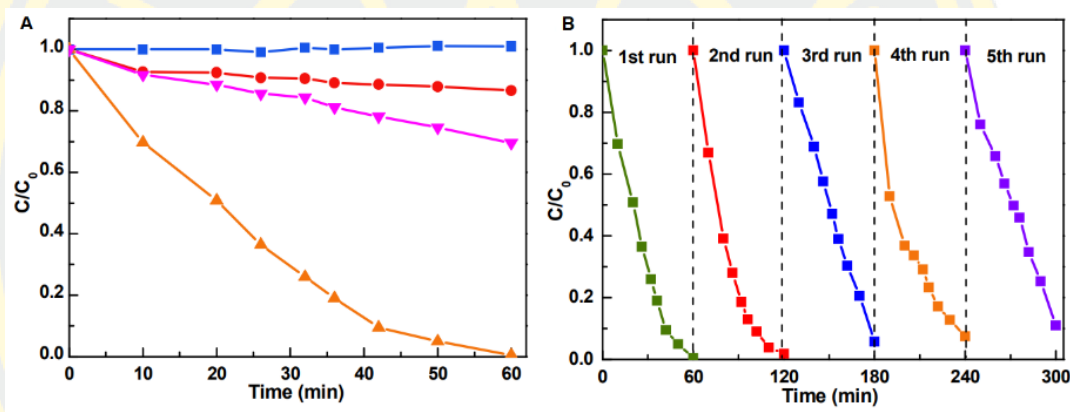


Figure 2 - 21 (A) Comparison of the catalytic performance of β -FeOOH/PDA/PPNW in methylene blue degradation in various conditions: under visible light (blue square), H₂O₂ and under visible light (red dot), H₂O₂ and under dark (inverted pink triangle), and β -FeOOH with H₂O₂ under visible light (orange triangle), (B) Reuse of β -FeOOH/polydopamine/PPNW for five runs (Zhang et al., 2015).

3. Polydopamine Coating on Perfluorinated Polymer

As mentioned previously, a PFA / FEP tube is a promising candidate for a photoreactor. However, the catalyst was difficult to immobilize due to low hydrophilicity. There are many methods for surface treatment of materials such as plasma treatment or chemical treatment. However, such techniques require advanced instruments, and can be difficult to operate. For example, the chemical treatment

requires ammonia gas and sodium metal (Nemani et al., 2018); (Qian et al., 2016); (Ebnesajjad, 2015), which is extremely dangerous to handle.

Bi et al. (2017) used polydopamine as an adhesive layer to immobilize enzyme onto an inner wall of a PTFE tube by flowing dopamine solution through the PTFE tube at flow rate 5 $\mu\text{m}/\text{min}$ for 12 h. After the polydopamine coating, they subsequently filled the mixture solution of polyethylenimine (PEI) and lipase in the PTFE tube, and the solution stayed in the tube for 1 h to reach adsorption equilibrium. The PTFE tube was then washed with Tri-base to remove unattached PEI and lipase. The surface composition was characterized by XPS as shown in Figure 2-22. It appeared that the F1s signal of PTFE was decreased after polydopamine coating, meaning that the inner wall of PTFE tube was already covered by polydopamine.

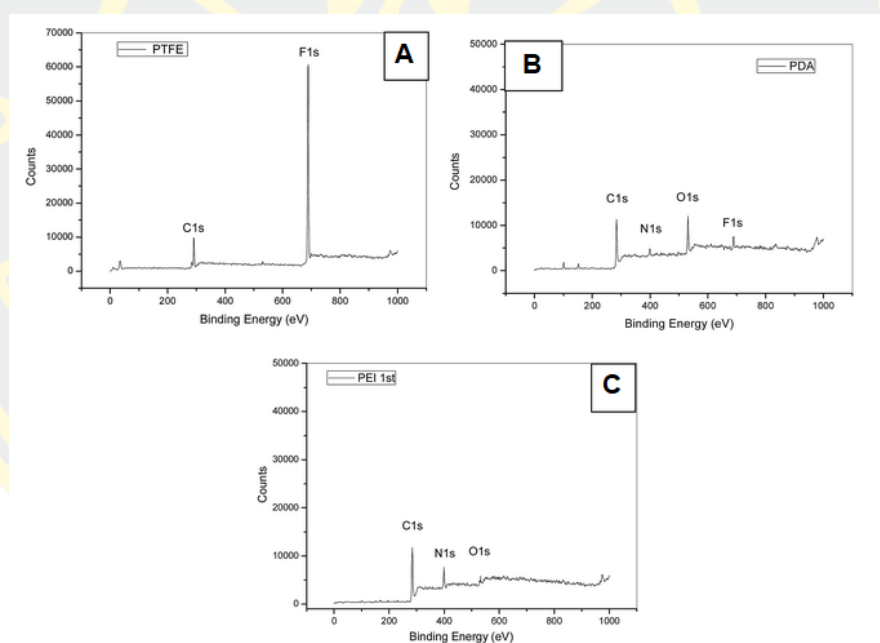


Figure 2 - 22 (A) The XPS spectra of PTFE, (B) After polydopamine coating, and (C) After coating PEI (Bi et al., 2017).

Zhu et al. (2018). demonstrated to immobilize Pd nanoparticles onto the inner wall of PTFE tube via polydopamine coating. First, the dopamine solution was flowed in a PTFE tube with a flow rate of 1ml/h for 5 h via a syringe pump. Then, the tube was washed with deionized water. Then, the aqueous solution of K_2PdCl_4 (prepared by

dissolving PdCl₂ and KCl) flowed into the PTFE tube at a flow rate of 0.1 μL/min for 12 h. To form the Pd ions to nanoparticles, the resulting PTFE tube was placed into a vacuum-tube resistance furnace and heated in the H₂ under 473K for 4 h. The Pd nanoparticles on the PTFE tube was characterized by FESEM as shown in Figure 2-23; the Pd nanoparticles were found to be uniformly dispersed onto the PTFE tube.

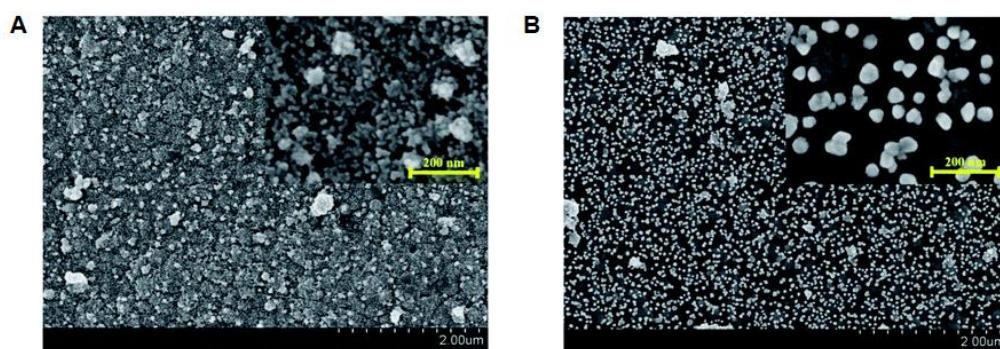


Figure 2 - 23 FESEM images of Pd/polydopamine/PTFE: (A) before reducing and (B) after reducing (Zhu et al., 2018).

Photocatalytic benzene oxidation to phenol

Phenolic compounds are used in many application, including the synthesis of salicylic acid (Kirimura et al., 2010), the starting material of phenolic resin (Hirano & Asami, 2013), which have been using in board range in industry (Jin et al., 2019; Pizzi & Ibeh, 2014). More than 95% of phenol production is done through the cumene oxidation process, with the remaining percentage being produced via toluene oxidation or recovered from coal tar (Schick & Weber, 2001) The cumene process start with Benzene and propylene are combined in the presence of a catalytic substance, typically phosphoric acid, to form cumene(isopropylbenzene). Next, cumene is oxidized with air to form cumene hydroperoxide (CHP) through a radical chain mechanism. CHP is then subjected to an acid-catalyzed cleavage (usually using sulfuric acid) where it is decomposed into phenol and acetone. This step requires precise temperature control to prevent further oxidation. The resulting mixture is then distilled to separate phenol and acetone from unreacted cumene and other byproducts (Schick & Weber, 2001). The

cumene process suffers from a number of drawbacks including several reactive steps, excessive downstream processing (e.g., fractional distillation and separation), high energy consumption, and use of aggressive chemicals (e.g., strong inorganic acids) (Schmidt, 2005)

Alternatively, phenol can be synthesized through the hydroxylation of benzene. This process presents a challenge due to the tendency of phenol to undergo over-oxidation. Despite the use of various oxidants like H_2O_2 and O_2 in thermal catalytic reactions, there is low selectivity towards producing phenol. The reactivity of phenol oxidation is enhanced by heating, making thermal catalysis unsuitable for this reaction (wang).

Photocatalysis has become an appealing approach due to its ability to facilitate the formation of radicals, such as hydroxyl radicals, necessary for hydroxylation through electron-hole generation. Various types of photocatalysts, both homogeneous and heterogeneous, have been shown to be effective for this process

Park and Choi (2005) explores an alternative, environmentally friendly approach to synthesize phenol from benzene using photocatalytic oxidation processes. This study focuses on the direct synthesis of phenol by generating hydroxyl radicals on ultraviolet-illuminated TiO_2 photocatalysts, which then hydroxylate benzene to phenol, as well as other products like hydroquinone and catechol. The authors found that adding Fe^{3+} , H_2O_2 , or both, significantly improves both the yield and selectivity of phenol production in a TiO_2 suspension. Surface modifications to TiO_2 , such as depositing platinum nanoparticles or fluorinating the surface, also had a substantial positive impact on the production yield and selectivity of phenol. Notably, fluorination doubled the phenol yield due to the increased production of mobile OH radicals.

Furthermore, polyoxometalates were employed in the study, playing a dual role as a photocatalyst and a reversible electron acceptor, ultimately enhancing the yield of phenol further when added to the TiO_2 suspension. The study discusses various reaction mechanisms, suggesting means to take advantage of photocatalytic systems for more efficient phenol synthesis.

Shiraishi et al. (2005) focused on improve the catalytic selectivity of TiO_2 . Traditionally, TiO_2 catalyzes reactions that generate hydroxyl radicals which nonspecifically oxidize substrates, leading to low selectivity in products. The study

proposes using mesoporous TiO₂, which has been synthesized by surfactant-templating or an aggregation method, to enhance catalytic activity. mesoporous TiO₂, which is driven by the degree of adsorption of molecules on the catalyst surface. This process of adsorption encourages the selective transformation of molecules that are well-adsorbed. This is referred to as a "stick-and-stay" conversion, enabling the high-selectivity conversion of benzene into phenol at over 80%.

Yuzawa et al. (2012) synthesized phenols by directly hydroxylating aromatic rings using water as an oxidant. The process demonstrates high selectivity under specific wavelength light over a platinum-loaded titanium oxide photocatalyst, with two types of electrophilic active species involved based on pH conditions: surface oxygen radical under neutral or acidic conditions and hydroxyl radical in basic conditions. Both radicals are generated from holes on the titanium oxide surface and attack the aromatic ring to form an intermediate that is then transformed into a hydroxylated product via addition-elimination mechanism. The study also highlights how the platinum-loaded titanium oxide system overcomes limitations seen in other catalysts and oxidants previously investigated for selective direct hydroxylation of aromatic rings. Key factors for success include the wavelength of light, absence of oxygen, and amount of platinum loading. Additionally, the photogenerated electron's role involves reducing protons to form a hydrogen radical which further enhances formation of both the hydroxylated product and molecular hydrogen.

Ide et al. (2011) enhanced the photocatalytic oxidation of benzene using gold nanoparticles supported on titanium dioxide under sunlight. They found that conducting the reaction in a carbon dioxide atmosphere significantly improved the yield and selectivity for converting benzene to phenol. Two types of commercially available TiO₂, P25 and Tynoc A-6, were modified with gold nanoparticles to create the photocatalysts, named 3%Au@P25 and 4%Au@Tynoc, respectively. Experiments used water as the solvent and a solar simulator as the light source within a closed system equipped with Pyrex glass for sunlight irradiation. The use of 3%Au@P25 in air resulted in a mixture of oxidation products along with 8% yield and 62% selectivity for phenol. Under a CO₂ atmosphere, production of by-products was suppressed, and the yield of phenol jumped to 13% with 89% selectivity. A similar enhancement was observed using 4%Au@Tynoc, achieving 12% yield and 95% selectivity under CO₂.

Application of continuous flow system for photocatalytic reaction

A microreactor has been a promising tool to perform a photocatalytic reaction due to its high surface area to volume ratio, which was beneficial for both photon and mass transfers. Over the past decade, there have been a considerable number of developments of the photocatalytic microreactor. For instance, Lei L et al. demonstrated a planar photocatalytic microreactor for water treatment using solar energy (Lei et al., 2010) as show in Figure 2-24. The microreactor had a planar chamber enclosed by two TiO₂-coatd glass substrates as the top and bottom layers, which were sealed via UV curation. Methylene blue degradation was used as a reaction model. Different protocols were studied: film preparation methods, film thickness, and flow rate. 30% degradation was obtained within 5 min for the solution of 3×10^{-5} M methylene blue.

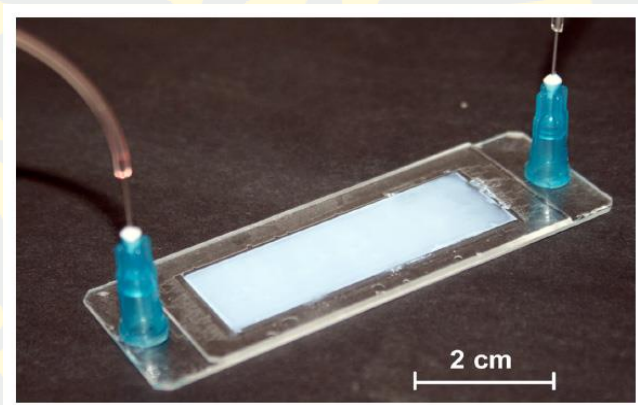


Figure 2 - 24 Photograph of photocatalytic planar microreactor (Lei et al., 2010).

Lin et al. (2016) compared the performance between a planar photocatalytic microreactor (PPM) and a microchannel-type photocatalytic microreactor (MPM) (Lin et al., 2016) in Figure 2-25. The microreactor wall was immobilized with metal ion-doped TiO₂. The photocatalytic activity was evaluated by the degradation of methylene blue (MB) under UV- visible light and sunlight. A Xenon lamp was used as light source and used a light filter to choose a specific wavelength. The initial concentration of MB was 20 mgL⁻¹ and the solution were controlled flow rate by syringe pump. Their result

show that at the same resident time the degradation ratio of PPM was about 0.35 and 0.62 times higher than that of the MPM.

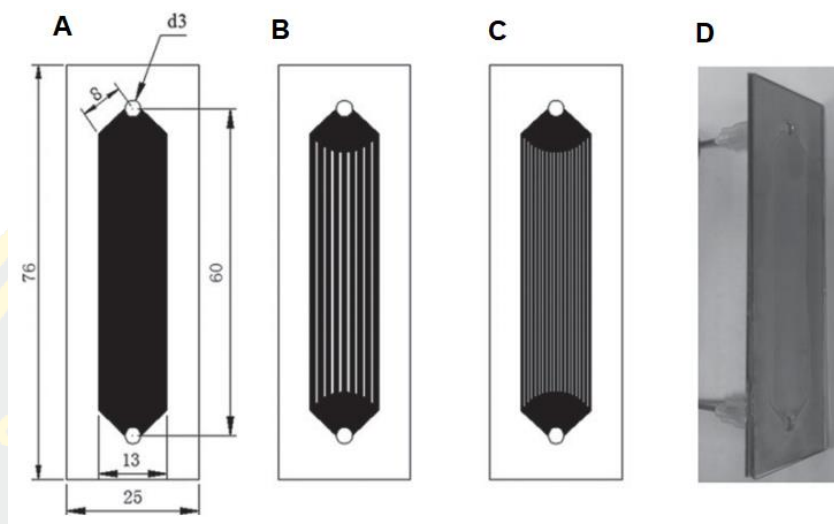


Figure 2 - 25 Different structures of planar microreactor (A) 1-channel, (B) 9-channel (channel wide 1 mm), (C)19-channel (channel wide 0.5 mm), and (D) the illustration of planar microreactor (Lin et al., 2016).

Gorges et al. (2004). studied the degradation of 4-chlorophenol (4-CP) by using a photocatalytic microreactor with immobilized TiO_2 (P-25 Degussa) as a photocatalyst and illuminated by UV-A LEDs (~ 385 nm in wavelength) The microreactor, which was made of a low temperature co-firing ceramic (LTCC), consisted of 19 parallel channels with a cross-section dimension of $200 \mu\text{m} \times 300 \mu\text{m}$ (Fig.6A). The total volume was 0.032 cm^3 . The channels were deposited titanium film a thickness of $5 \mu\text{m}$ and then subsequently to the deposition of TiO_2 film by anodic spark deposition (Figure 2-26). The microreactor was used to study the kinetic of degradation of 4-CP reaction as well as the effect of mass transfer. The result showed that the microreactor gave a low value of Da between 0.33×10^{-7} and 3.83×10^{-7} . This showed that the use of the microreactor could enhance the mass transfer.

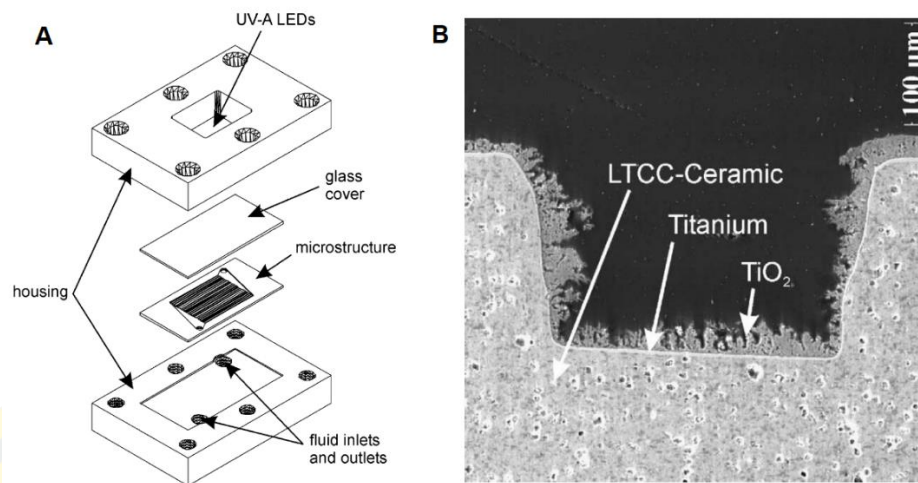


Figure 2 - 26 (A) microreactor component, (B) SEM image of the cross section of microchannel (Gorges et al., 2004).

Eskandarloo et al. (2015) presented a photocatalytic microreactor, which was made of stainless steel with an internal volume of $10.8 \mu\text{l}$, and had the deposition of Ag/TiO₂ on the channel wall. (Figure 2-27) The photocatalytic activity was evaluated with removal of terephthalic acid (TPA) under UV-LEDs light source. When the average residence time was increased from 7.2 to 64.8 s, the removal of TPA was increased from 60.83% to 93.19 % due to a longer radiation time. The microreactor was also tested in terms of reusability. The authors have demonstrated five reuse times without significant decrease in removal efficiency.

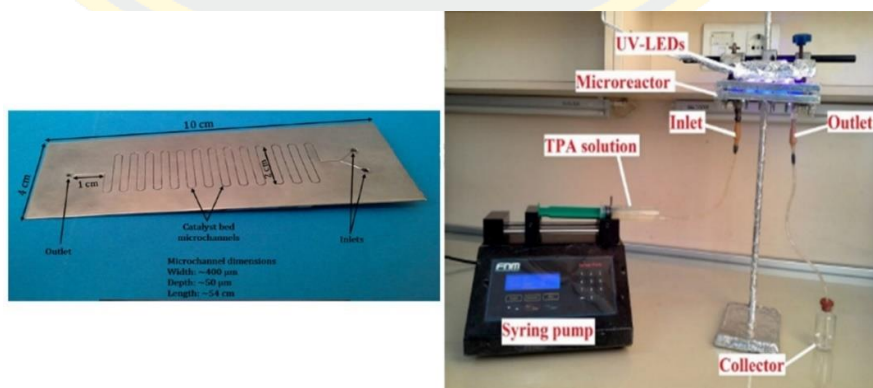


Figure 2 - 27 The photocatalytic microreactor was made of stainless steel, An experiment set up for TPA degradation (Eskandarloo et al., 2015).

Pu et al. (2019) demonstrated the synthesis of aniline in a microreactor via reduction of nitrobenzene. TiO_2 (P-25 Degussa, particle size 5-10 nm) was used as catalyst. Instead of using a fabricated microreactor, they used a capillary PFA tube with an inner diameter of 1 mm as a microreactor. The tubing was coiled around a Pyrex immersion well with an outer diameter of 50 mm and a height of 350 mm. The well was inserted with a 500 W high pressure mercury lamp. Upon their optimization on the synthesis, they found that the conversion of nitrobenzene dramatically increased from 25.5% to 87.8% when the mass ratio of TiO_2 to nitrobenzene increased from 0 to 0.4, but after that ratio, the trend became the opposite. When increasing the residence time more than 10 min, the conversion of nitrobenzene could reach up to 95.4% but the yield of aniline significantly decreased. Due to aniline is easy oxidized polymerized with the existence of oxidants as initiator.

Apart from the development of the photoreactor configurations, there have also been studies in photocatalyst immobilization techniques. Shen et al (2016) proposed a simple method to immobilize TiO_2 nanoparticles on the inner wall of glass capillaries (0.5 mm inner diameter and 10 cm long). They used NaOH to treat the inner wall of glass capillaries, and then flowed the aqueous solution of TiO_2 , which was prepared from $\text{Ti}(\text{OBu})_4$, ethanol and hydrochloric acid. The photocatalytic activity was performed by discoloration of methyl orange (MO) and oxidation of dibenzothiophenen (DBT) which have same concentration 20 mg/L. The result showed a promising performance; 87 % discoloration of MO was achieved in 40 s and the oxidation of dibenzothiophenen was complete within 2.8 min (Shen et al., 2015).

Nakamura et al. (2004) developed the uniform TiO_2 and $\text{SiO}_2/\text{TiO}_2$ film coated on inner wall of glass capillaries (0.53 mm or 0.2 mm I.D. and 60 cm long). To achieve the coating, the inner wall of glass capillaries was first modified by mixture of HSO_4 and H_2O_2 . Then, the glass capillaries were filled with the aqueous solution of TiO_2 or $\text{SiO}_2/\text{TiO}_2$ closed end both sides and dried at 88°C for 12 hours. The photocatalytic activity was performed by degradation of methylene blue (MB) 0.1 M. The microcapillaries reactor showed the high percentage of degradation was achieve more than 90 % for $\text{SiO}_2/\text{TiO}_2$ film and 80% for TiO_2 film in 60 s because SiO_2 increased the surface area reaction while 0.2 mm I.D. capillaries offer reaction time 20 s which is less than 0.53 mm I.D. 40 s.

Table 2 - 4 Comparison of difference type of microreactor and with difference reaction model.

Microreactor	dimension	Reaction model	Initial concentration [mM]	Residence time [s]	Degradation ratio [%]	Ref.
Planar microreactor made from glass slides and immobilized with TiO ₂ film	5 mm X 1.8 mm X 0.04 mm	Methylene degradation	0.03	300*	30	(Lei et al., 2010)
Planar microreactor made from stainless steel which TiO ₂ -coated and cover with glass slide on top	60 mm X 13 mm X 0.5 mm	Methylene degradation	0.06*	90	63 %	(Lin et al., 2016)
Planar microreactor made from co-fired ceramic which deposited TiO	19 channels cross section area 0.3 m X 0.2 mm	4-chlorophenol degradation	0.05	600*	40 %	(Gorges et al., 2004)
Microchannel made from stainless steel		terephthalic acid	0.07*	64.8	94 %	(Eskandarloo et al., 2015)
Microcapillary reactor made for PFA tube suspended TiO ₂	0.5 mm I.D.	oxidation nitrobenzene to aniline	0.03 M*	600*	95 %	(Pu et al., 2019)
Glass capillaries immobilized TiO ₂ on the inner wall	0.5 mm I.D. 100 mm long	Methylene degradation	0.06*	40	87 %	(Shen et al., 2015)
Glass capillaries immobilized TiO ₂ or SiO ₂ /TiO ₂ at inner wall	0.53 mm I.D. and 0.2 I.D. 60 mm long	oxidation of dibenzothiophene	0.11	168*	100 %	
		Methylene degradation	0.1	20	90 %	(Nakamura et al., 2004)

*These data were calculated via given data.

Merging the combination of heterogeneous photocatalysis and flow chemistry is appealing (Thomson et al., 2020). Heterogeneous photocatalysts enable simple catalyst separation, while flow chemistry enhances photon transfer and process scalability. Using a film reactor with a large irradiation area and short photon transmitting length results in uniform light distribution across the reactor's cross section (Puma & Yue, 2003). Some researcher designed a pack bed photocatalytic reactor which immobilize photocatalyst on glass beads to enhance surface area for light penetration (Claes et al., 2019).

Giusi et al. (2021) presented a new type of reactor designed for converting carbon dioxide into useful chemicals using sunlight. The main components of this reactor are nanomembranes made of titanium dioxide nanotubes that are aligned on a microperforated metallic substrate. This substrate acts as an electron collector and provides structural robustness to the reactor. These nanotubes are then functionalized with copper oxide through a process known as electrodeposition. Unlike traditional photocatalytic approaches, this new reactor can selectively convert CO₂ into C1-C2 carboxylic acids without producing unwanted by-products like hydrogen (H₂), carbon monoxide, methane, or other hydrocarbons. The presence of copper oxide allows for an additional reaction pathway leading to the production of C1-C3 alcohols or their derivatives.

The best performance is achieved using p-type copper(I) oxide (Cu₂O) on n-type TiO₂ nanotubes. This combination forms a p–n-type heterojunction which enhances the reactor's ability to harness visible light, leading to an approximate quantum yield of 21% with solar illumination. The reactor has shown exceptional Faradaic efficiency, with up to 47% for methanol and 73% for acetic acid production, which points to a promising avenue for CO₂ conversion into higher-value chemicals. This not only presents a potential pathway for sustainable chemical synthesis but also contributes to fundamental understanding in CO₂ photoreduction mechanisms.

Reilly et al. (2017) developed a new approach to improve hydrogen production through photocatalytic water splitting using a fluidized bed reactor with Pt-loaded TiO₂ spheres. Typical issues like the parasitic back reaction, mass transport, and radiation distribution limitations in conventional photocatalysts are addressed. The new method employs Pt-loaded TiO₂ spheres fluidized in Na₂CO₃ solution and exposed to UV light,

leading to a significant increase in hydrogen production rates and apparent quantum efficiency—up to 211 $\mu\text{mol/h}$ and 1.33% respectively. This marks a 44% quantum efficiency enhancement compared to traditional photocatalysts.

Puma and Yue (2003) presented a mathematical model to aid in the design and optimization of thin-film slurry photocatalytic reactors used for water purification. These reactors utilize the photocatalytic properties of titanium dioxide slurry suspensions under illumination to generate hydroxyl radicals for decomposing pollutants in water and wastewater.

The industrial application of these systems has been limited due to a lack of mathematical models for design and scale-up. They address this gap by introducing a generic model that simulates steady-state, continuous flow conditions using solar or UV lamps. The model assumed three flow regimes: falling film laminar flow, plug flow, and slit flow, with falling film and plug flow showing higher performance than slit flow. The model is dimensionless, facilitating scaling through dimensional analysis, and parameters can be easily estimated from real-world systems. It suggests that falling film laminar flow outperforms plug flow at higher reactor conversions (>80%).

CHAPTER 3

CONTINUOUS-FLOW PURIFICATION OF SILVER NANOPARTICLES AND ITS INTEGRATION WITH FLOW SYNTHESIS

The work in this chapter has been published in Journal of Flow Chemistry, volume 10, pages 353-362, (2020).

DOI: <https://doi.org/10.1007/s41981-020-00084-8>

Introduction

Metal nanoparticles have been increasingly utilized in heterogenous catalysis. Upon their production, they can be synthesized by chemical or biological methods. Chemical reduction is one of the most convenient methods due to its simple setup and effective control of their morphology. The chemical reduction involves a metallic precursor, a reducing agent, and capping ligands. The ligands have an important role in controlling a growth process as well as stabilizing the nanoparticles. Typically, they are added in excess. After the synthesis, some of the ligands are adsorbed to a surface of the nanoparticles while the other is free in solution, as shown in Figure 3-1 Both modes of the ligands are also known to affect the catalytic performance of the nanoparticles. Although the adsorbed ligands are important in protecting the nanoparticles from aggregation, they can be viewed as a physical shell that limits access of reactant to the surface of the metal nanoparticles (Park & Choi, 2005; Wu et al., 2014). In similar, the free ligands, which are solvated in the solution, can also have some detrimental effect on the performance of the nanoparticles. Shen et al. (2013) demonstrated that the excess ligands affected surface modifications such as shell growth and ligand

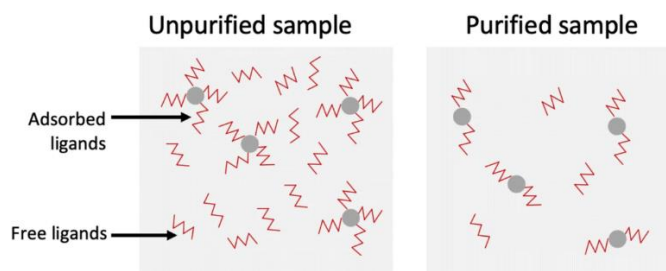


Figure 3 - 1 Drawing to represent the two states of ligands: adsorbed and free. A purified sample may contain less ligands in both states

There are multiple methods to remove these ligands from the solution. Some methods focus on removing the adsorbed ligands. For example, thermal annealing and UV-ozone exposure can be used to decompose the ligands, and then the fragmented ligands can be washed off by solvents or gas (Cargnello et al., 2015; Niu & Li, 2014). Other methods are aimed to remove the ligands in general, whether they are in adsorbed or free state. These two states are dynamic. By removing the free ligands, more ligands will get desorbed as to shift towards an equilibrium between the two states.

As a method for removing ligands, multiple washing or precipitation-redissolution (PR) is commonly employed in the laboratory. Upon the centrifugation, the excess ligands and other impurities can be retained in the supernatant while the nanoparticles are precipitated. The nanoparticles are then re-dissolved to go through another two or three washing cycles. Usually, anti-solvent is added for effective precipitation. However, the PR method has been reported with some challenges. For instance, Hassinen et al. (2012) showed that the use of a protic solvent as the anti-solvent induced the stripping of ligands from the colloidal nanocrystals or quantum dots (QD). Similarly, Morris-Cohen et al. (2010) found that repeated exposure to methanol during the PR method caused a nearly complete removal of L-type ligands, which in turn decreased the PL quantum yield as the L-type ligands were important for passivating the QD surfaces as well as facilitating the QD dispersion. Moreover, the nanoparticles smaller than 5 nm are also difficult to precipitate due to their low density, so the PR method could be unsuitable. Therefore, alternative purification methods have been proposed (Hühn et al., 2017; Shen, Gee, et al., 2017). These include filtration

(Alele et al., 2016), dialysis (Alkilany et al., 2014), gel permeation chromatography (GPC) (Shen et al., 2016) and solvent extraction (Yang et al., 2015).

Among different methods, GPC and solvent extraction are promising technologies for large production as they can be operated in continuous mode, and simply scaled up. By its nature, GPC is a batchwise process as different components elute from the column at different time points. However, multiple columns can be operated in parallel such that the solution can be sequentially fed into columns, and the overall purification can be viewed as continuous. On the contrary, the continuous mode of solvent extraction is more straightforward than that of GPC. It can be enabled by a membrane separation or a level sensor (Martini et al., 2019; Weeranoppanant, 2019). Our recent work has constructed a multistage extraction for continuous purification of nanocrystals, and demonstrated the operation with two examples: cadmium selenide nanocrystals and gold nanoparticles (Shen, Weeranoppanant, et al., 2017).

The continuous purification can also be useful for many applications in the field of nanoparticle synthesis. It can be used as in-line purification for multistep processing. Flow synthesis of nanoparticle has been demonstrated in many articles (Baek et al., 2011; Emmanuel et al., 2017; Lin et al., 2004), but is often followed by batchwise purification. Potentially, the continuous purification can enable a fully-continuous system from the flow synthesis to other downstream steps such as shell growth and ligand exchange. In addition, the purified nanoparticles tend to be less stable due to the absence of the capping ligands. Therefore, they may aggregate during storage. To address this issue, the continuous purification can be used for on-demand production of nanomaterials.

In this work, we demonstrated the continuous nanoparticle purification. The ligands were removed by a continuous-flow solvent extraction (F). The two phases from the extraction were separated by the membrane-based device (Adamo et al., 2013). The samples from the continuous-flow purification were characterized and evaluated in terms of their purity and physical qualities. They were compared with an as-synthesized or unpurified sample as well as samples purified with a conventional PR method and batchwise solvent extraction (SE). In this article, silver nanoparticles (AgNPs) with sodium dodecyl sulfate (SDS) as capping ligands were used as a case study. AgNPs from different purification methods were tested for their catalytic activity in

degradation of 4-nitrophenol (4-NP) (Hervés et al., 2012). With the promising results, we also applied this flow extraction system to demonstrate its integration with a flow synthesis of AgNPs.

Methods

1. Preparation of the AgNPs solution

The AgNPs solution was synthesized from two solutions, which were prepared separately. Silver nitrate (AgNO_3) solution was prepared at 2 mM. A solution of sodium borohydride (NaBH_4) and SDS was prepared such that the NaBH_4 : AgNO_3 molar ratio was 10:1 and the SDS: AgNO_3 weight ratio was 20:1. The synthesis procedure was similar to the one reported by Song et al. (2009). Both solutions were prepared in deionized water. Then, 50 mL of the AgNO_3 solution was added dropwise to 50 mL of the NaBH_4 and SDS solution. The dropwise addition was operated via a syringe pump, which was set a flow rate at 5 mL/min. The mixture was stirred continuously during the addition and an hour after the last drop. This as-synthesized, unpurified solution was referred to as “as-syn” throughout this article.

2. Purification of the AgNPs solution

There were three different purification methods studied in this work: precipitation-redissolution (PR), batchwise solvent extraction (SE), and continuous-flow solvent extraction (F).

2.1. Precipitation-redissolution (PR)

The as-syn sample was precipitated in a centrifuge (Force 1624 microcentrifuge) at 13,000 rpm at 25 °C for 20 mins. The supernatant was removed in each round of precipitation. The remaining AgNPs were re-dispersed by adding deionized water. The samples were notated as “PR1,” “PR2,” and “PR3” for the samples that were purified by one, two, three cycles of precipitation-redissolution, respectively.

2.2. Batchwise solvent extraction (SE)

The as-syn sample was added with ethyl acetate, which served as an extraction solvent. Two different amounts of ethyl acetate were studied: 1:1 and 1:3 of the as-syn: ethyl acetate volumetric ratio. The extraction was done by mixing in a shaking water bath (Hanyang Scientific Equipment) at 250 rpm and 30 °C for 20 mins.

After the mixing, the mixture was let to settle at 30 °C for an hour, and the two layers appeared. A top layer was ethyl acetate-rich, and it was removed. The bottom layer was an aqueous solution containing the purified AgNPs were collected. The samples were notated as “SE1:1” and “SE1:3” for the samples that were purified with 1:1 and 1:3 of the as-syn: ethyl acetate volumetric ratio, respectively.

2.3. Continuous-flow solvent extraction (F)

In this method, the as-syn sample was purified in continuous-flow manner. The flow system was setup as shown in Figure 3-2. The as-syn sample and solvent were delivered to the system by two syringe pumps (New Era Pump System and Chemyx). The two phases were mixed at a T-junction (IDEX Health & Science, USA), and flowed into a perfluoroalkoxy alkanes (PFA) tubing (1/16” ID) with an internal volume of 4 mL. The two phases were then separated in a membrane-based device (SEP-10, Zaiput Flow Technologies, USA). The membrane used as polytetrafluoroethylene (PTFE) with 0.5 µm in pore size. In the membrane separator, the ethyl acetate-rich phase will permeate through the membrane while the aqueous phase was retained. The aqueous phase was collected after three residence times to ensure a steady-state extraction. Two different ratios (by volume) of the as-syn to ethyl acetate were tested (1:1 and 1:3). The samples were notated as “F1:1” and “F1:3” for the samples that were purified with 1:1 and 1:3 of the as-syn: ethyl acetate volumetric ratio, respectively.

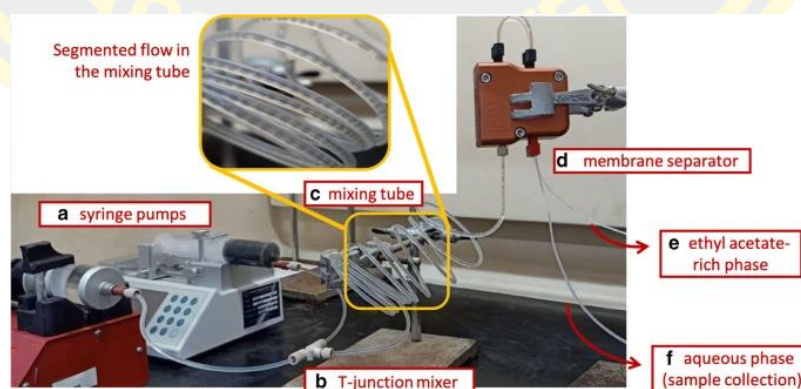


Figure 3 - 2 The picture of the continuous-flow setup for solvent extraction of the nanoparticle solution. The flow regime in the PFA mixing tube is a segmented flow

3. Characterization of the AgNPs samples

There are eight samples in total: as-syn (unpurified), PR1, PR2, PR3, SE1:1, SE1:3, F1:1, and F1:3. The samples were adjusted to similar concentrations by diluting until the final UV-VIS absorbance was 2.735. Then, the samples were examined by the following characterizations. First, the samples were characterized with UV-VIS spectrometer (Varian Cary 1E). All of the samples were diluted with deionized water to the same final absorbance of 2.75 AU. The spectrometer was operated between 300 and 800 nm with a resolution of 1 nm. Second, the samples were evaluated in terms of whether the purification affected their morphology. The samples were taken with a high-resolution transmission electron microscope (TEM, JEOL, JEMARM200F, operated at 200 kV). Prior to the TEM measurement, the colloidal suspensions of AgNPs were diluted in methanol and subjected to the sonication. The diluted suspensions were dropped on Cu-grids and let dried at room temperature prior to the TEM measurement. Third, the samples were also studied in terms of AgNPs concentration using ICP-OES measurement (Optima 8300, PerkinElmer, a working range 0.05–5 mg/L). For this measurement, the sample was prepared by being centrifuged until a clear supernatant was obtained. This was done to remove all silver ions that might affect the ICP-OES results. The pellet was then diluted with 1 mL of DI water. A 0.5 mL of the solution was digested using microwave digestion with 10 mL of 67% nitric acid. The microwave digestion was as follows: 160 °C, 5 min ramp, 5 min hold; 190 °C, 3 min ramp, 35 min hold; 50 °C, 1 min ramp, 15 min hold. The digested solution was adjusted to a final volume of 100 mL before ICP-OES measurement. Finally, the purity of the samples were analyzed by ¹H-NMR (400 MHz, Bruker avance III HD). For quantitative analysis, a 0.125 M potassium hydrogen phthalate (KHP) was used as an internal standard. The NMR samples were prepared by adding 300 μL of the AgNPs samples, 20 μL of the KHP in 250 μL of D₂O. The NMR results were used to estimate the concentration of the ligands (SDS) in each sample, as following:

$$C_{SDS} = \frac{I_{SDS}}{I_{KHP}} \times \frac{N_{KHP}}{N_{SDS}} \times C_{KHP} \quad (3-1)$$

where C_{SDS} is the concentration of SDS in each sample; I_{SDS} and I_{KHP} are interested integral peak areas of SDS ($\delta = 3.96$) and KHP ($\delta = 7.45$), respectively; N_{SDS} and N_{KHP} are interested number of nuclei of SDS and and KHP at the interested peak locations; C_{KHP} is the known concentration of KHP added to each sample.

The percent SDS removal could be calculated as following:

$$\%SDS\ removal = \frac{C_{SDS,as-syn} - C_{SDS}}{C_{SDS,as-syn}} \times 100 \quad (3-2)$$

Where $C_{SDS, as - syn}$ is the original concentration of SDS in the as-syn sample and C_{SDS} is the concentration of SDS in each sample (normalized such that the AgNPs concentration of the sample is equal to that of the as-syn sample).

4. Study of the catalytic performance of the AgNPs samples in 4-NP degradation

The 4-NP degradation was studied in the UV-VIS spectrometer. An aqueous 4-NP solution (0.05 mM, 1.5 mL) was mixed with a freshly prepared $NaBH_4$ solution (0.02 M, 1.5 mL) in a glass cuvette. Then, 20 μ L of the AgNPs samples was added to the cuvette, and the timer started. The absorbance was taken at every 1 min. The absorbance at 400 nm was plotted against time to calculate the rate constant. The experiment was repeated three times for each AgNPs sample.

5. Integration of flow synthesis of AgNPs with continuous-flow purification

The flow synthesis of AgNPs was demonstrated with similar reaction condition as the previous section. Silver nitrate ($AgNO_3$) solution was prepared at 2 mM. A solution of sodium borohydride ($NaBH_4$) and SDS was prepared such that the $NaBH_4$: $AgNO_3$ molar ratio was 10:1 and the SDS: $AgNO_3$ weight ratio was 20:1. The two solutions were loaded into two separate syringe columns. Then, the two solutions were flowed at a rate of 0.1 mL/min each. They were mixed at a T-junction (IDEX Health & Science, USA), and flowed into a PFA tubing (1/8"OD, 1/16" ID) with an internal volume of 3.96 mL. This was equivalent to the residence time of about 20 mins. The sample was collected after three residence times from this flow synthesis, and notated as "As-syn_in flow." In another experiment, the continuous-flow purification was

integrated. The outlet from the flow synthesis was connected directly to another T-junction at which ethyl acetate was flowed at a rate of 0.6 mL/min and mixed. The ratio of the as-syn to ethyl acetate was approximately 1:3 (by volume). Ethyl acetate served as a solvent to extract out SDS from the as-syn phase. After the T-junction, the two phases formed a segmented flow in a PFA tubing (1/16"OD, 0.02"ID) with an internal volume of 0.06 mL. The two phases were separated by the membrane separator as discussed earlier. The aqueous phase was collected after three residence times to ensure a steady state. The sample collected was notated as "F1:3_in flow". The picture of the integrated continuous-flow synthesis-purification setup was shown in Figure 3-3.

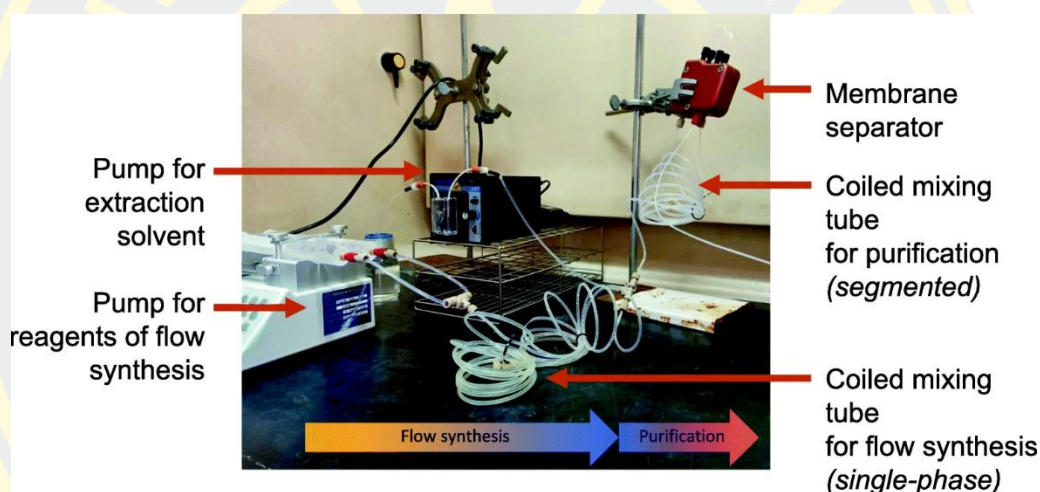


Figure 3 - 3 The picture of the integrated continuous-flow synthesis-purification setup

Result and discussions

Physical properties of the AgNPs samples The characterizations from the UV-VIS spectroscopy showed that all the samples have similar absorption spectra. As shown in Figure 3-4, the PR samples were found with a slight red-shift of the absorption maximum with $\lambda_{\max} = 400\text{--}402$, compared to the as-syn sample ($\lambda_{\max} = 393$). This may be an effect of changed density of capping ligands on the surface of AgNPs (Ansar et al., 2013). The larger full width at half maximum (Table 3-1) for the PR samples also pointed out possible aggregation. As discussed later, the PR method provided the greatest removal of the ligands, which had an important role in keeping AgNPs stable in colloidal state. On the other hand, the samples from the solvent extraction, either

batchwise (SE) or continuous-flow (F), showed constant absorption spectra with the as-syn sample. This emphasized that the solvent extraction was a mild and non-destructive method to purify the nanoparticles.

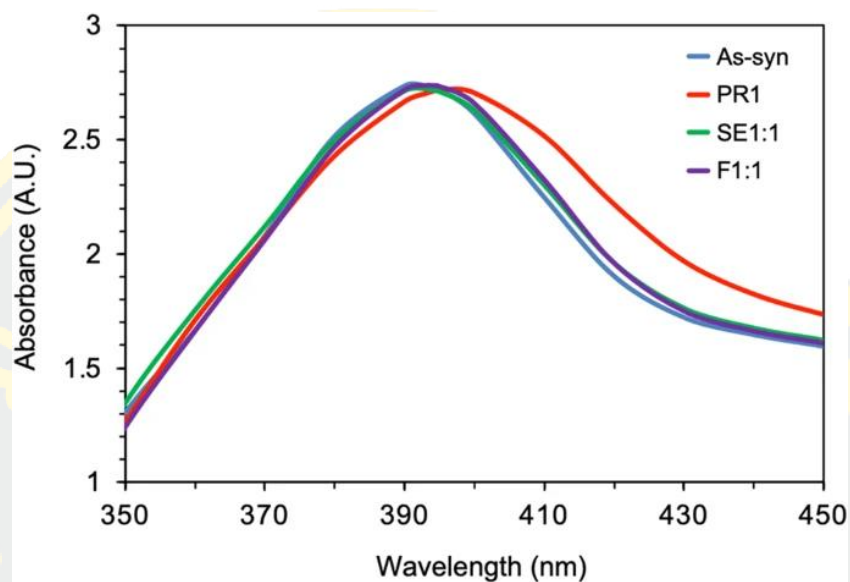


Figure 3 - 4 The UV-VIS absorption spectra of the samples from different purification methods

Table 3 - 1 The measured wavelength at maximum absorbance (λ_{\max}) and full width at half maximum (FWHM) of AgNPs from different purification methods.

Sample	λ_{\max} (nm)	FWHM (nm)
As-syn	393	135
PR1	400	144
PR2	400	147
PR3	402	148
SE1:1	393	136
SE1:3	393	131
F1:1	395	133
F1:3	395	134

The TEM image, taken for the as-syn sample, is shown in Figure 3-5. The AgNPs have a spherical shape. Using an image analysis, we found that the AgNPs from this synthesis had the sizes about 15.63 ± 4.34 nm. In comparison, the representative TEM images of the samples purified by three different methods (PR, SE, and F) are shown. The shapes and particle sizes from other purification methods were not significantly different with the average sizes of 16.38 ± 4.34 nm, 15.94 ± 2.64 nm, and 16.22 ± 2.65 nm, for PR1, SE1:1, and F1:3, respectively. This was true even when more cycles of precipitation-redissolution or more solvent were employed. This suggested that both PR and solvent extraction methods (batch and flow) did not affect the morphology of the AgNPs.

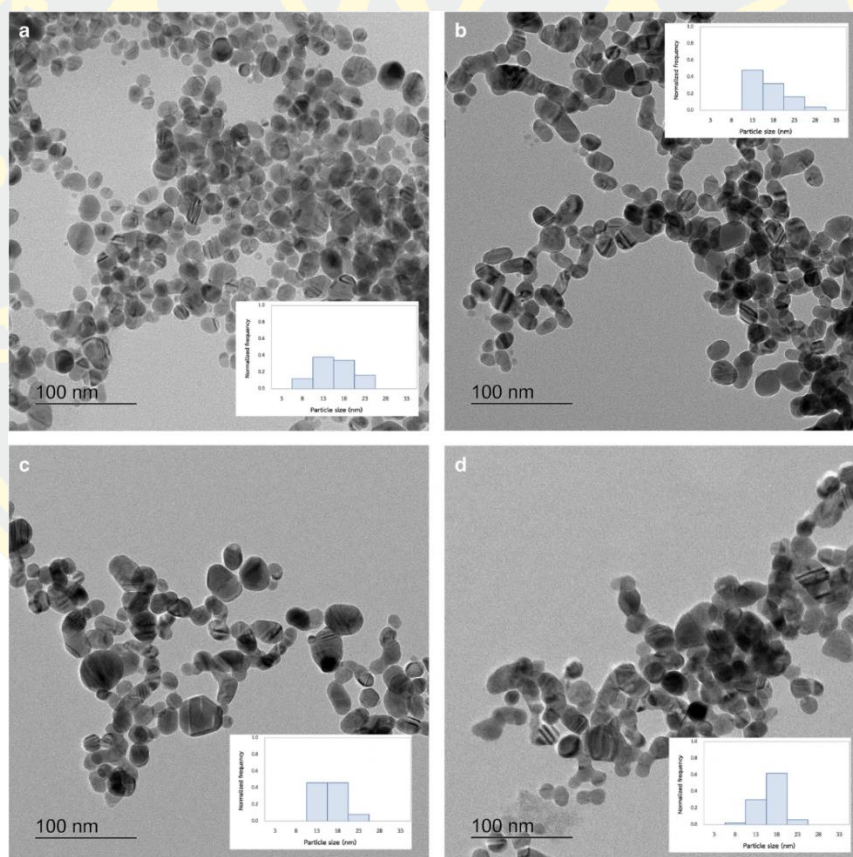


Figure 3 - 5 The representative TEM images of (A) the as-syn, (B) PR1, (C) SE1:1, and (D) F1:1 samples.

1. Percent SDS removal of different purification methods

The as-syn sample showed that the NMR peaks of SDS at $\delta = 3.96$, 1.50, 1.25, and 0.86. The intensity at $\delta = 3.96$ was selected to represent the concentration of SDS in the sample. There was no shift in the peaks of SDS; therefore, we were unable to distinguish between two states of SDS (adsorbed and free). For the quantitative analysis, the intensity of the internal standard, KHP, at $\delta = 7.45$ was used as a calibrant peak. As shown in Figure 3-6, the $\delta = 3.96$ peak of the PR sample disappeared, indicating the complete removal of the ligands. A 100% SDS removal of ligands was achieved within two cycles of PR (i.e. PR2). Note that the % SDS removal was calculated in comparison to the amount of SDS in the as-syn sample, and normalized by the concentration of AgNPs of each sample. The calculation was described in the Experimental Section. For the SE and F samples, the SDS were not completely removed. However, the intensities of the peak at $\delta = 3.96$ were significantly reduced from the as-syn sample, suggesting the partial removal of the SDS from the sample. The additional peaks at $\delta = 4.1$ and 2.0 were due to the partially miscible ethyl acetate from the extraction. The increasing ratio of the ethyl acetate, from 1:1 to 1:3, improved the percent SDS removal considerably. As shown in Table 3-2, for SE, about 62.39% SDS removal was obtained when the ratio of as-syn to solvent is equal to 1:3. The flow extraction (F) yielded a similar % SDS removal (56.73% when a ratio of as-syn to solvent is equal to 1:3).

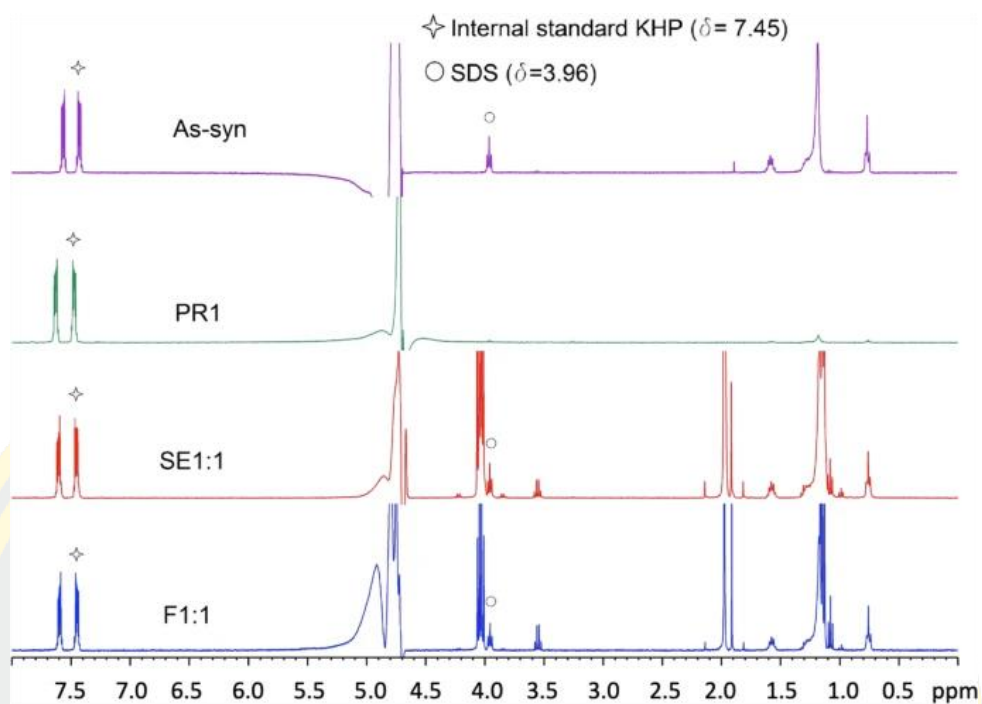


Figure 3 - 6 $^1\text{H-NMR}$ spectra of the as-syn, PR1, SE1:1, and F1:1 samples.

Table 3 - 2 The calculated % SDS removal of different purification methods

Samples	% SDS removal
PR1	92.23%
PR2	100.00%
PR3	100.00%
SE1:1	19.63%
SE1:3	62.39%
F1:1	9.33 %
F1:3	56.73%

2. Comparison between batchwise (SE) and flow (F) extraction methods

As discussed in the previous section, the performances of the SE and F were not much different. However, the SE method will require a significantly longer purification time than the F method. As depicted in Figure 3-7, even after 60 mins, the layers from the SE method were not clearly separated. This is a common phenomenon since most of the capping ligands are amphiphilic, and can serve as a surfactant. Therefore, an emulsion layer tends to form and remains stable for a long time. However, by using the membrane separator, the two phases could be separated instantly by virtue of surface phenomena. As presented earlier, % SDS removal of the SE and F methods were comparable. This indicated that the phase separation in the continuous membrane separator was also close to complete. This emphasized an advantage of the continuous-flow purification because it could shorten the experiment time. In our experiment, the PR method could take 30–90 min while the SE could take 2 h.

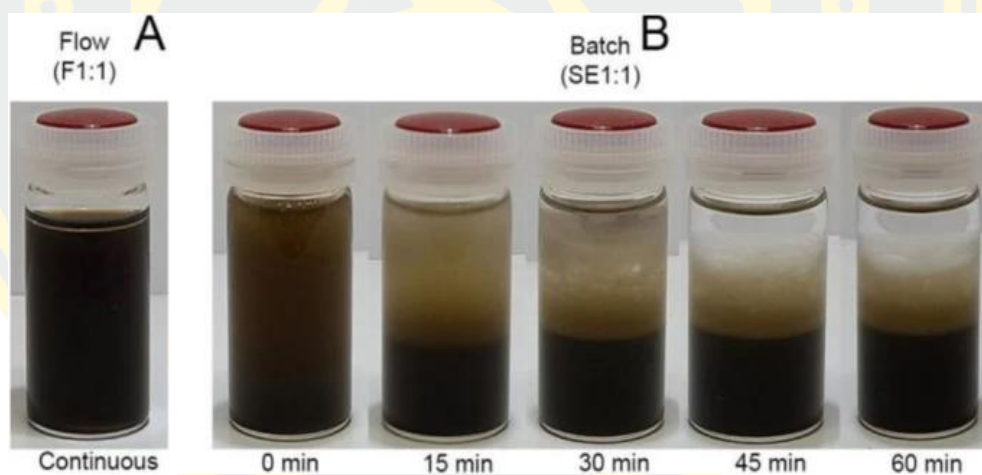


Figure 3 - 7 (A) The separated aqueous phase of the F1:1 sample, after being continuously separated from the membrane separator, (B) The mixture of the SE1:1 after mixing for 1 h. It required a significant amount of time for the mixture to separate into clear phases

3. Catalytic performance of the AgNPs samples

This section was aimed to highlight an importance of nanoparticle quality in catalysis. The AgNPs samples were evaluated for their catalytic performance in the degradation of 4-NP. The AgNPs can serve as a catalyst to mediate electron transfer from BH_4^- to the 4-NP molecule (Pradhan et al., 2020). This reaction has often been used as a model reaction for studying catalysis of AgNPs. Here, we compared only the samples with similar AgNPs concentration. As shown in Figure 3-8, the rate constant of the experiment with the as-syn sample gave the lowest rate constant. This indicated that the density of the capping ligands significantly affected the active area of the catalyst, and highlighted the importance of the nanoparticle purification. The PR sample performed fairly well with the average rate constant of 0.425 min^{-1} . The SE and F samples had lower catalytic performances. This was in line with the previous results that the SE and F samples were less pure than the PR sample. These results suggested that the purification method may have an effect on catalysis of AgNPs. To further improve the quality of the AgNPs, more cycles of extraction (i.e. multistage extraction) should be implemented.

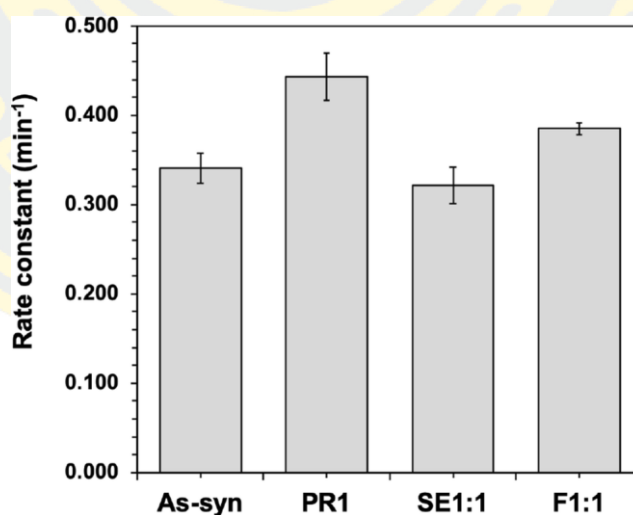


Figure 3 - 8 Rate constants of the 4-NP degradation, using the AgNPs samples from different purification methods as catalysts

4. Integrated flow synthesis of AgNPs with continuous-flow purification

The flow synthesis of AgNPs was demonstrated using the same chemical reaction as the batchwise synthesis. However, instead of dropwise addition of reagents (reaction time = 2 h), the reagents (AgNO_3 , NaBH_4 , and SDS) were flowed together into a tubing with residence time of 20 mins. Two pumps were required. One pump was for the aqueous solution of AgNO_3 while the other pump was for the solution of NaBH_4 and SDS. The as-syn sample (notated as “as-syn_in flow”) was collected and characterized with UV-VIS absorbance. The absorbance peak was found to be at 410 nm, as depicted in Figure 3-9. In another experiment, the as-syn stream from this flow synthesis was sent directly to the continuous-flow purification setup. The as-syn sample was mixed in flow with ethyl acetate, an extraction solvent, at a flow ratio of 1:3 (as-syn: ethyl acetate). The sample was named as “F1:3_in flow”. The UV-VIS absorbance peak of this F1:3_in flow sample was 404 nm, indicating slight blue shift probably due to changes of ligand density on the AgNPs surface. The two samples were characterized in terms of SDS concentration using $^1\text{H-NMR}$ (Figure 3-10). Using the same calculation as the previous section, we found that this integrated continuous-flow synthesis-purification setup yielded 73.27% SDS removal.

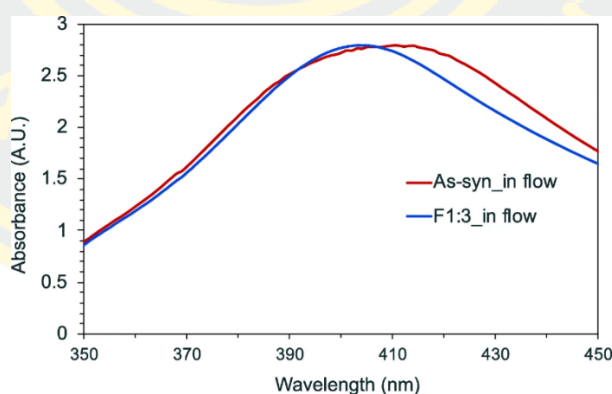


Figure 3 - 9 The UV-VIS absorption spectra of the as-syn_in flow and F1:3_in flow samples that were produced in the integrated continuous-flow synthesis-purification setup

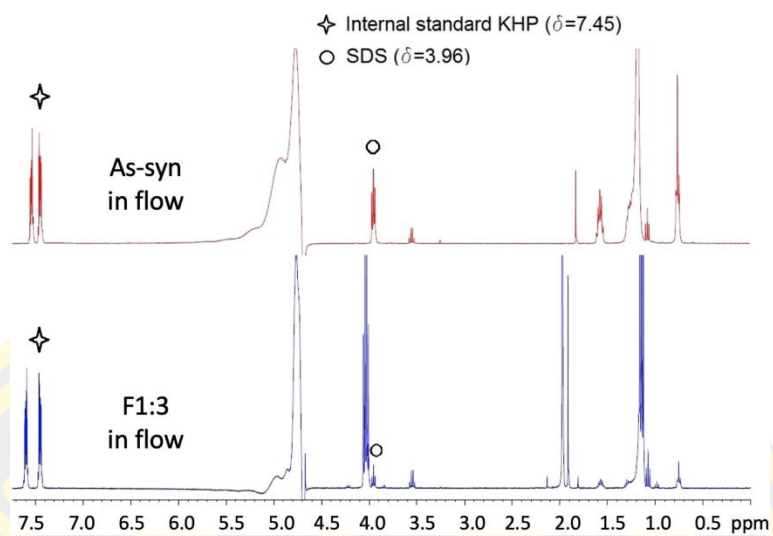


Figure 3-10 ^1H -NMR spectra of the as-syn in flow and F1:3 in flow samples that were produced in the integrated continuous-flow synthesis-purification setup

CHAPTER 4

A SIMPLE FABRICATION OF A CONTINUOUS-FLOW PHOTOCATALYTIC REACTOR USING DOPAMINE-ASSISTED IMMOBILIZATION ONTO A FLUOROPOLYMER TUBING

The work in this chapter has been published in *Industrial & Engineering Chemistry Research*, volume 3, page 1322-1331, (2022).

DOI: <https://doi.org/10.1021/acs.iecr.1c04303>

Introduction

Heterogeneous photocatalytic systems can use light energy to generate an electron-hole pair, which can then induce reduction and oxidation. They have a wide range of applications such as water splitting for hydrogen evolution (Maeda & Domen, 2010), reduction of CO₂ to hydrocarbons (Ola & Maroto-Valer, 2015), environmental remediation (Chong et al., 2010) or organic synthesis (Hoffmann, 2015). The common materials are metal oxides, metal sulfides (Tahir et al., 2020), and metal free and organic photocatalysts (Rahman & Davey, 2018; Rahman et al., 2020). Their characteristic band gaps allow them to work under a UV to visible light range. Among different materials, titanium dioxide (TiO₂) has been the most commonly-used one due to its chemically inert, non-toxic properties as well as low cost.

Aside from the type of catalysts and light source, reactor design is another important consideration for designing a photocatalytic system (Visan et al., 2019). Conventionally, these systems are performed in a suspension glass vessel with a submerged chamber for a light source. It has advantages of a simple setup and an easy control of catalyst loading. However, its long light penetration depth causes significant photon absorption. Also, with its low specific surface area, heat transfer can be inefficient, resulting in a non-uniform temperature distribution. A number of flow photoreactor designs have been proposed as alternatives to the suspension batch reactor (Buglioni et al., 2022; Cambié et al., 2016; Thomson et al., 2020), including a monolith reactor (Carneiro et al., 2009), a pack bed reactor (Claes et al., 2019; Claes, Gerven, et al., 2021), and a microfluidic reactor (de Sá et al., 2018; Leblebici et al., 2015). While many of these designs enable a continuous operation with a short path of light, they

require tedious fabrications, and may cause an excessive pressure drop for a reaction with a long residence time.

A mesoscale tubular reactor emerges as a promising option, and it has been used widely in flow chemistry (Khositanon et al., 2020; Plutschack et al., 2017; K. Wang et al., 2018; Zhang et al., 2018). Its characteristic diameter of 500 μm – 2 mm is beneficial for the photon transfer. In this work, we are interested in a commercially available fluoropolymer tubing such as PFA (perfluoroalkoxy alkane), or FEP (fluorinated ethylene propylene). PFA exhibits superior light transparency (up to 96% for visible and up to 91% for UV light) and excellent chemical compatibility (Su et al., 2014). A key advantage of using a PFA tubing over an inorganic tubing (e.g. glass) is its high flexibility. A PFA tubing can be easily bent into different shapes such as a helical coil wrapping around a light source to maximize photon utilization. The uses of PFA tubings have been demonstrated for continuous-flow homogeneous-catalyzed photochemical reactions (Vidyacharan et al., 2019). Nevertheless, the tubings have been rarely employed with heterogeneous catalysts as the solid suspension may cause a clogging problem and require time-consuming separation (e.g., ultracentrifugation). To alleviate such problems, photocatalysts should be immobilized onto tubing walls.

A fluoropolymer is chemically inert, so the immobilization onto this type of tubings can be challenging. Previous methods used thermal processing (near a melting point of PFA of 285°C) (Ramos et al., 2014). and ultrasound treatment (Colmenares et al., 2018; Pradhan et al., 2020) to facilitate the adhesion of photocatalysts to the fluoropolymer. However, these physical methods may cause irregular surface etching and non-homogeneous coating (Colmenares et al., 2018). To address these issues, a surface modification via a wet chemical processing has been proposed (Richardson et al., 2015). In the wet processing, the surface can be functionalized or modified by a chemical agent to accommodate either covalent or ionic interactions with catalyst particles. Nevertheless, the agent for a fluoropolymer is quite limited due to the hydrophobic and chemically inert nature of a fluoropolymer. Among different agents, polydopamine (PDA) is a compatible and versatile choice as it has been reported to form a stable layer onto different surfaces (Ryu et al., 2018). Its adhesive nature is attributed to its amine and catechol groups. Particles can be subsequently deposited onto the surface-bound PDA. The examples include the immobilizations of graphene

(Zhang et al., 2014), and enzymes onto polytetrafluoroethylene (Bi et al., 2017), which is a common fluoropolymer. Such dopamine-assisted immobilization can be achieved at mild preparation and minimal destruction to fluoropolymer.

The deposition of photocatalysts onto PDA relies on physical interactions such as electrostatic force and hydrogen bonding (Wang et al., 2020). However, in order to achieve a high particle-PDA affinity, a mediating agent may be required. In this work, polyethyleneimine (PEI), a cationic polymer, can be directly grafted onto the PDA layer via a Michael reaction (Liu et al., 2020). As an interlayer between PDA and photocatalysts, the PEI layer offers a strong ionic interaction with photocatalysts, resulting in a higher particle density. Overall, we proposed a protocol to immobilize P25 onto a PFA tubing. PFA was first modified with PDA and further grafted with PEI. Instead of in situ synthesis or use of a PEI/P25 mixture as in previous reports (Cheng et al., 2018; Li et al., 2019), a sequential layer-by-layer assembly of PEI and P25 was developed to obtain multiple layers and more loadings of immobilized P25. This prepared tubing was employed as a tubular reactor, which was demonstrated with the photocatalytic methylene blue decolorization in a continuous flow. A reactor design modelling was also performed to reveal kinetic and adsorption properties of this photocatalytic reactor.

Methods

1. Materials

Titanium dioxide (Degussa P25), polyethyleneimine (PEI) (MW = 10,000, branched), and dopamine hydrochloride, and 2-amino-2-(hydroxymethyl)-1,3-propanediol (Tris base) were purchased from Sigma Aldrich. A general-grade 6% (w/v) solution of sodium hyperchlorite (NaOCl) was purchased. A smectite (a synthetic hectorite, Sumecton SWF) was kindly donated from Kunimine Industrial Co., Ltd. Methylene blue (MB) was purchased from Ajax Finechem. The PFA sheet (thickness 5 μ m) and tubing (1/8" O.D., 1/16" I.D.) were purchased from Misumi (Thailand).

2. Fabrication of a flow cell for surface characterization

Since a PFA tubing has a cylindrical shape, its curvature makes it challenging to perform the surface characterization (e.g., electron microscopy). To simply validate our immobilization protocol, we designed a flow cell to embed a flat PFA sheet. As shown in Figure 4-1, the flow cell was made of poly(methyl methacrylate) or PMMA. It had an overall dimension of 30 mm x 70 mm. The top plate was grooved by a CNC milling machine to make a rectangular channel (1.5 mm x 1.5 mm x 50 mm) for a fluidic path, which was sealed by a Viton™ o-ring to prevent the sideways leakage. The inlet and outlet ports were attached with IDEX nanoport fittings.

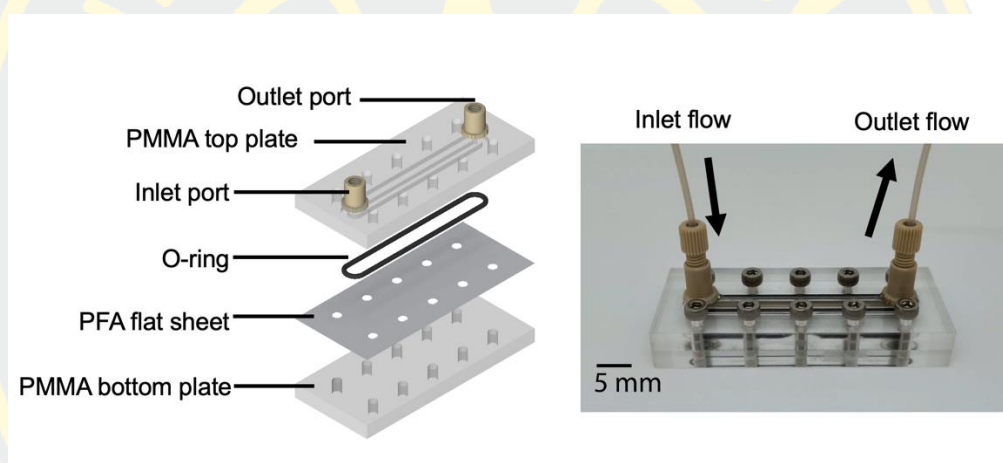


Figure 4 - 1 A flow cell embedding a PFA flat sheet for validating our immobilization protocol

3. Immobilization in a flow cell

A flat PFA sheet was cut to a size of 30 mm x 70 mm. The sheet was cleaned with acetone and sonicated for 10 min, then washed with DI water to remove any acetone. The sheet was installed into the flow cell. The immobilization protocol was as follows. First, a 2 mg/mL dopamine solution in a 10 mM Tris base (pH 8.5) solution was flowed into the flow cell at a flowrate of 0.028 mL/min for 24 h. Second, the DI water was flowed to wash any residual dopamine or un-adsorbed PDA. The sheet was dried at 60 °C for 2 h. This sample was denoted as a “PDA” sheet.

To further coat a poly(ethyleneimine) or PEI layer, the sheet was installed back into a flow cell. A 10 mM PEI solution was flowed to a flow cell. The inlet and outlet were capped to keep the solution in a channel for 30 min. After that, the DI water was flowed at a flowrate of 0.1 mL/min for an hour in order to wash any weakly adsorbed PEI. The sheet was dried at 60 °C for 2 h. The sample was denoted as a “PEI@PDA” sheet.

Subsequently, the photocatalysts could be immobilized onto the prepared sheets by flowing a suspension of P25 into the flow cell. However, to maintain P25 as colloidal, a synthetic hectorite or SWF was added to adjust rheology of the suspension (See appendix B1). Therefore, the suspension of P25 was prepared by mixing 0.1 g of P25 and 0.1 g of SWF in 100 mL of DI water. Before use, it was sonicated for 10 min to ensure colloidal dispersion throughout the volume. The suspension was flowed into the flow cell embedding the prepared sheets at a flow rate 0.027 mL/min for 12 h. The sheet was then dried at 60 °C for 2 h. The immobilizations of P25 using the previously prepared “PDA” and “PEI@PDA” sheets were denoted as “P25@PDA” and “PEI-P25_{1L}@PDA” sheets, respectively. We repeated the steps of PEI coating and P25 immobilization in a layer-by-layer approach for 3 and 5 layers. The samples were denoted as “PEI-P25_{3L}@PDA” and “PEI-P25_{5L}@PDA” sheets, respectively.

4. Surface characterization of the PFA sheets with immobilized photocatalysts (from the flow cell)

The surface morphology and elemental analysis of the PFA sheets were characterized using a JEOL JSM-7610F scanning electron microscope (SEM) and an energy-dispersive X-ray (EDX) probe, respectively. The SEM images were taken at a low landing energy of 1.5 kV on a gentle-beam high mode. The sheets were platinum-sputtered at 10 mA for 300 s to increase the surface conductivity before the measurement. In addition, a Fourier-transform infrared spectroscopy (FT-IR) (PerkinElmer) was conducted in the wavenumber range of 400-4000 cm⁻¹ in order to examine presence of functional groups on the surface and, thereby, confirm formations of PDA and PEI layers. The transmission of the sheets with immobilized photocatalysts was measured using a UV-Vis spectrometer (PerkinElmer, Lambda 1050) at wavelengths between 300 – 800 nm.

5. Immobilization in a PFA tubing to fabricate a photocatalytic tubular reactor

A PFA tubing (1/8" O.D. and 1/16" I.D.) from Misumi (Thailand) was used. To maintain a similar fluidic phenomenon to that in the flow cell, the linear velocities of immobilizing solutions were kept at the same value for the two setups. As shown in Figure 4-2, a 2 mg/mL dopamine solution in a 10 mM Tris base (pH 8.5) solution was first flowed into the tubing at a flowrate of 0.0235 mL/min for 24 h. The tubing was washed with DI water, flushed with nitrogen gas and dried at 60 °C for 2 h. The tubing was then filled with a PEI solution and capped for 30 min. The tubing was washed with DI water, and dried at 60 °C for 2 h. Subsequently, the solution of P25 and SWF was flowed into the tubing at a flowrate of 0.0235 mL/min for 12 h. The sheet was then dried at 60 °C for 2 h. The immobilizing steps could be repeated to form 3 and 5 layers. The tubing coated with only a PDA layer was denoted as a "PDA" tubing. The tubing coated with a PDA, PEI, and P25 for 1, 3, and 5 layers (PEI-P25 layer-by-layer approach) were denoted as "PEI-P25_{1L}@PDA," "PEI-P25_{3L}@PDA," and "PEI-P25_{5L}@PDA" tubing, respectively.

The tubing samples were also characterized with the inductively coupled plasma - optical emission spectrometry (ICP-OES) for quantifying a specific loading density of photocatalysts. Prior to ICP-OES, the immobilized tubing was washed by filling its internal volume with a 0.6% NaOCl solution, which could cast off the primary PDA layer, and sonicated for 10 min. The washing solution, containing released P25, was collected and adjusted to a final volume of 10.0 mL. The sample was taken to the ICP-OES measurement for the amount of total titanium ions. The specific density was calculated with the following Equation:

$$\text{Specific density of TiO}_2(\text{mg}/\text{cm}^2) = \left(\frac{C_{Ti} \times 0.01}{2\pi RL} \right) \left(\frac{MW_{TiO_2}}{AW_{Ti}} \right) \quad (4-1)$$

Where C_{Ti} is a measured concentration of titanium ions from the ICP-OES (mg/L), R is a radius of the tubing sample (cm), L is a length of the tubing sample (cm), AW_{Ti} is the atomic weight of titanium (47.867 g/mol), and MW_{TiO_2} is the molar weight of TiO_2 (79.866 g/mol).

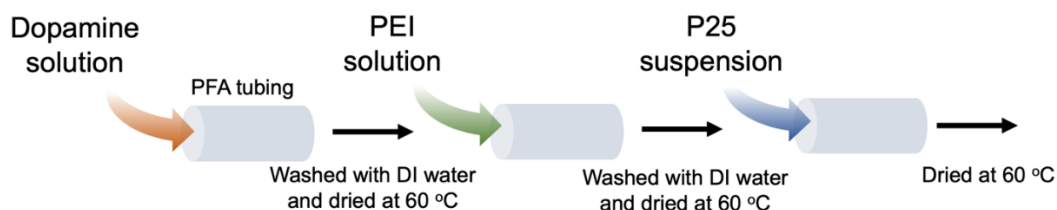


Figure 4 - 2 Schematic of the immobilization protocol for preparing the photocatalytic tubular reactor

6. Photocatalytic activity of a tubular reactor

The photocatalytic reactor was set up as shown in Figure 4-3. The reactor was irradiated by a 10 W UV-LED with a wavelength of 365 nm. The light source was located at a specific distance from the reactor. The actual light intensity was measured using a photometer (Hopoocolor, OHSP 350P). Here, a photocatalytic methylene blue degradation was chosen as a model reaction. The volume of the reactor was 1.76 mL. Prior to illumination, the solution was flowed in to fill the reactor completely in the dark. When the light is turned on, the timer starts as $t = 0$. The samples were collected at every three residence times (e.g., for 10-min residence time condition, we collected at 30, 60, 90 min and so on). The concentrations of the methylene blue at the outlet at each time interval were collected and monitored using a UV-Vis spectrometer (absorbance at 664 nm). In this experiment, the tubular reactors fabricated with different layers (“PEI-P25_{1L}@PDA,” “PEI-P25_{3L}@PDA,” and “PEI-P25_{5L}@PDA”) were tested. The inlet methylene blue concentration was kept at 0.0500 mM, and the flowrate of the methylene blue solution was maintained at 0.176 mL/min, corresponding to a residence time of 10 mins. In order to confirm that the decolorization occurred primarily due to the photocatalytic activity, we also performed additional sets of experiments including (i) the methylene blue decolorization under illumination in the absence of immobilized P25 (photolysis experiment) and (ii) the methylene blue decolorization in the dark in the presence of immobilized P25 (adsorption experiment). The percent decolorization is defined as below:

$$\text{Percent decolorization} = \frac{(C_{in} - C_{out})}{C_{in}} \times 100 \quad (4-2)$$

Furthermore, the effects of inlet concentrations and power of the light source were examined. The concentration of the methylene blue was varied at 0.00625, 0.0100, 0.0125, 0.0250, 0.0375 and 0.0500 mM. The power of the light source was also varied to 20%, 40%, 60%, 80%, and 100% of the maximum output (10 W). In the last part, the steady-state concentrations were fitted to a tubular reactor modelling to determine the reaction and adsorption rate constants.

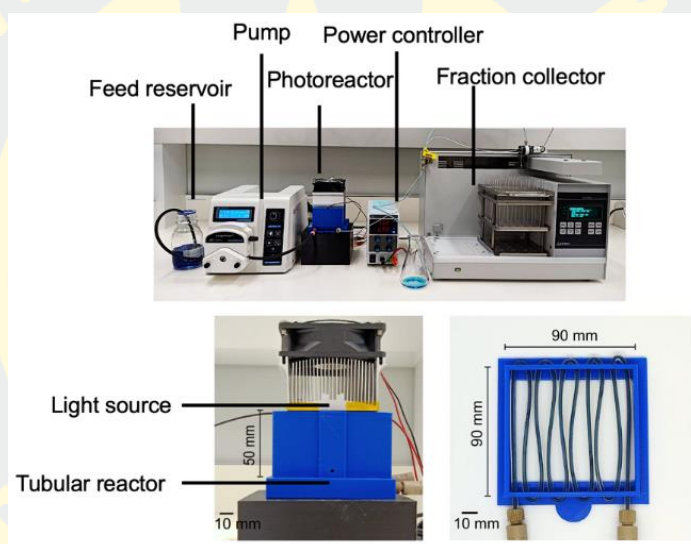


Figure 4 - 3 Setup for a continuous-flow photocatalytic reaction

Results and discussions

1. Characterization of the deposition and immobilization using a flow cell

The flow cell provided a simple way to characterize the surface modification as the PFA was flat. The samples of the PFA sheets before and after the modification are shown in Figure 4-4. The surfaces became apparently white after the depositions of PDA, PEI layers and immobilizations of P25. As shown in Figure 4-5, the FTIR result of the “PDA” sheet sample exhibited two minor peaks at 1596 and 1510 cm^{-1} , belonging to $\nu_{\text{ring}}(\text{C}=\text{C})$ and $\nu_{\text{ring}}(\text{C}=\text{N})$ stretching modes, respectively, representing the aromatic amine ring of the polydopamine. The presence of the deposited PDA was also

confirmed by a broad peak centered at 3300 cm^{-1} , which represented $\nu(\text{N-H})$ stretching mode of the secondary amine formed. The center of the broad peaks should locate at ~ 3400 and 3500 cm^{-1} ($\nu(\text{N-H})$ stretching of the primary amines) if non-deposited dopamine species were presented (Zangmeister et al., 2013). The emerging peaks at 2875 and 2920 cm^{-1} , which were characteristics of $\nu(\text{C-H})$ stretching of the aliphatic CH_2 group, verified the formation of the PEI layer in the PEI@PDA sheet sample. For the “PEI-P25_{1L}@PDA” sheet, we observed the intensity increases in the broad peak above 3000 cm^{-1} as well as the peak around 1630 cm^{-1} . These two peaks represent $\nu(\text{O-H})$ stretching and $\delta(\text{O-H})$ bending modes, respectively. These were probably due to the surface OH-groups of adsorbed water molecules on the P25 (Jensen et al., 2005). However, the FTIR results could not confirm the presence of the immobilized P25, so further surface characterization (SEM-EDX) was performed subsequently.

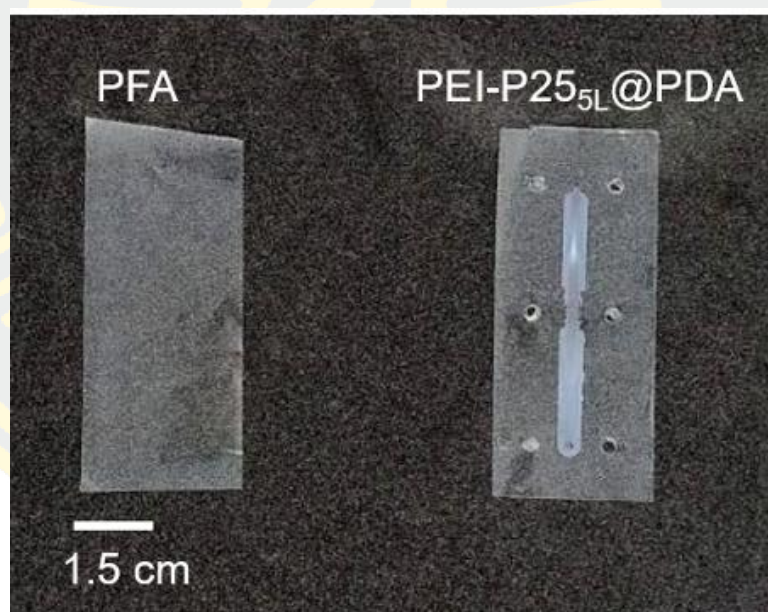


Figure 4 - 4 Appearance of a bare PFA and a “PEI-P25_{5L}@PDA” sample

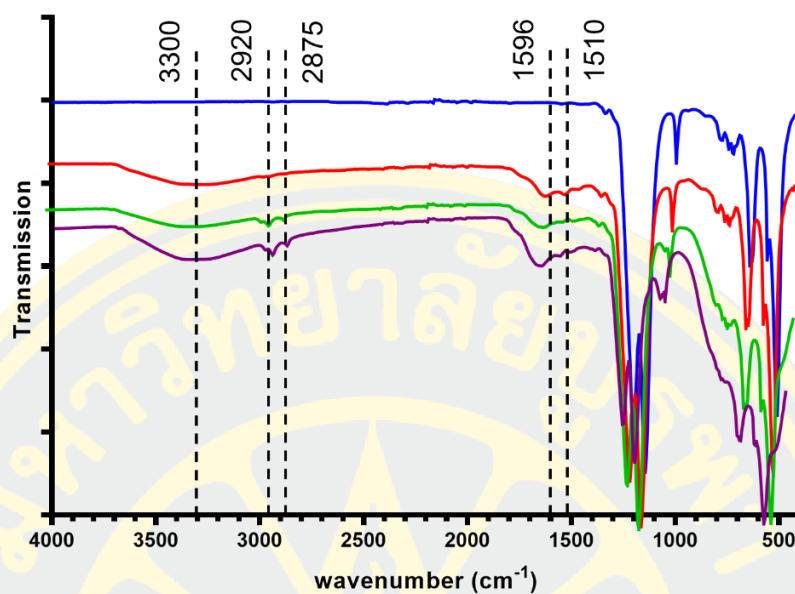


Figure 4 - 5 Transmission FTIR spectra of the surface-modified PFA sheets

Figure 4-6 shows the SEM images of different samples with immobilized P25. Fine particles were observed in the “P25@PDA” sheet. The EDX, mapping on titanium, confirmed the presence of the immobilized P25 TiO₂. However, using only the PDA adhesive layer resulted in a very low density of the immobilized P25. On the contrary, the samples with the layer-by-layer assembly of PEI-P25 showed a significantly higher density of P25. The surface of the “PEI-P25_{SL}@PDA” sheet sample revealed the most dense dispersion of P25.

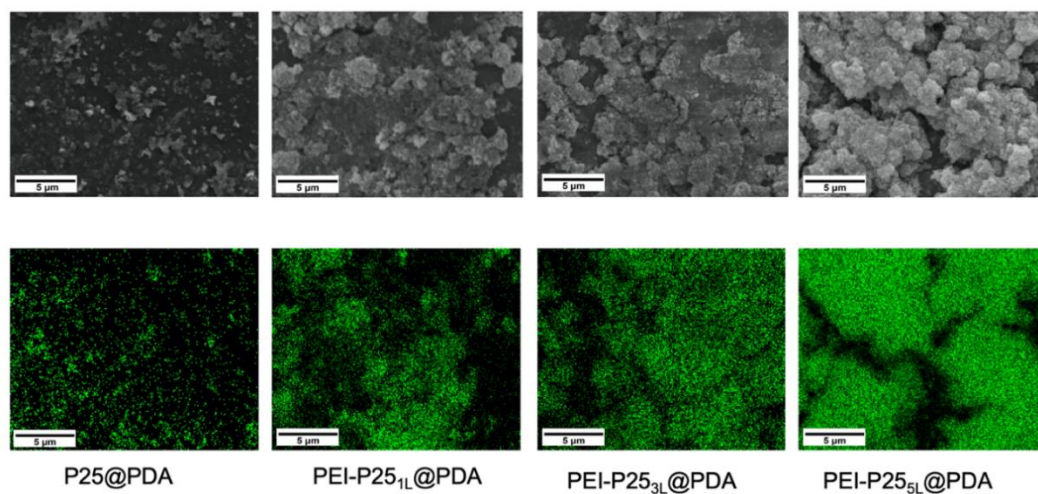


Figure 4 - 6 SEM images of the surface-modified PFA sheets and EDX mapping with Ti atoms

The samples were characterized by UV-vis spectroscopy (Figure 4-7). The “P25@PDA” sheet sample showed a similar absorbance spectrum of that of the PDA film alone, probably due to a low density of the immobilized P25 as confirmed previously by the SEM-EDX result. Upon the sequential deposition of PEI and P25, the absorptions at wavelengths below 500 nm increased. PEI itself has no absorption in the range of 300 – 800 nm. The increase in absorbance, especially in the UV range, was likely a result of the immobilized P25. The absorbance increased with the number of PEI-P25 bilayers, corresponding to the increasing density of the immobilized P25.

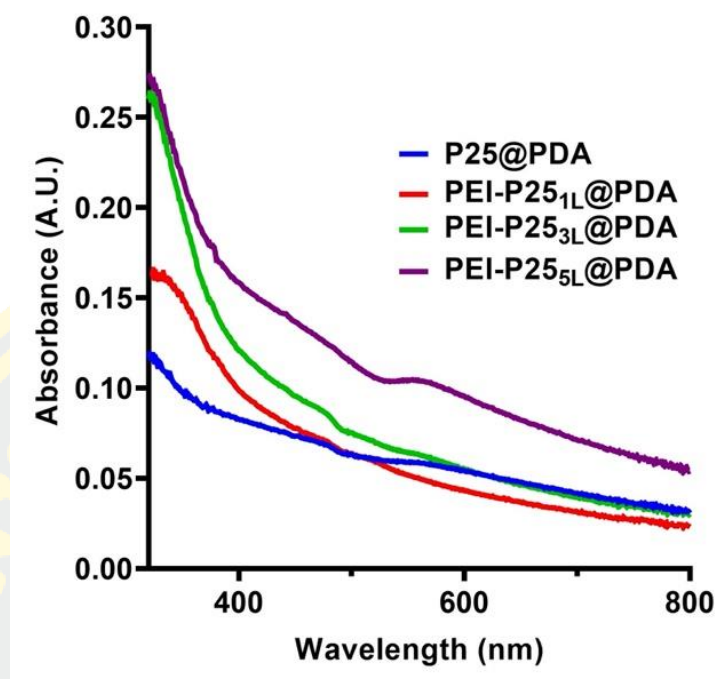
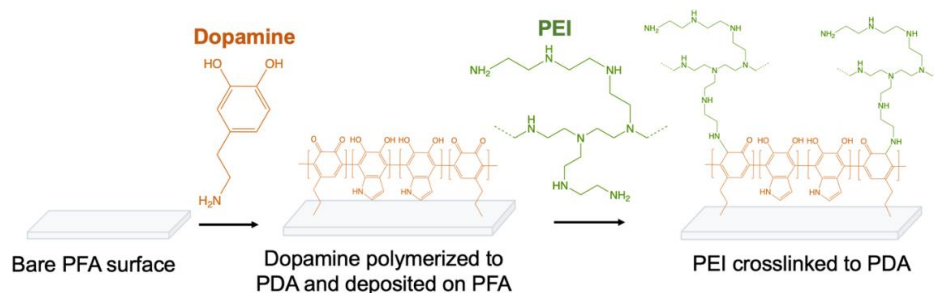


Figure 4 - 7 Absorbances of different prepared samples

The FTIR and SEM/EDX results confirmed the presence of different layers (PDA, PEI, and P25) as they were deposited and immobilized onto the PFA sheets. Although the mechanism of the PDA deposition onto substrates remains in dispute, we hypothesized that the amine moiety of dopamine or PDA is adsorbed onto the PFA surface. Dopamine can undergo cyclization and oxidation to become 5,6-indolequinone, which can be polymerized under a mild alkaline condition to give indole/catechol heteropolymer on the PFA surface. The PEI chains can subsequently be crosslinked to the deposited PDA via the Michael addition (Figure 4-8(A)). When P25 was prepared in DI water, its suspension had a pH value around 6.3. At this pH, the PEI and P25 are positively and negatively charged, respectively. Therefore, P25 can be bound to the layer of PEI through the electrostatic interactions. Multi-layer assembly can be achieved by layer-by-layer depositions of PEI and P25 (Figure 4-8(B)).

(A)



(B)

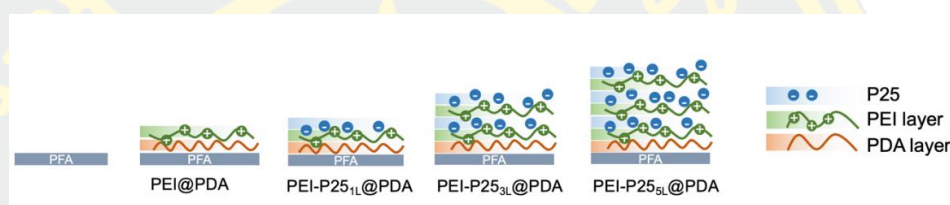


Figure 4 - 8 Possible mechanism of (A) PDA and PEI depositions and (B) layer-by-layer immobilization of P25

2. Immobilization in a PFA tubing: specific density of photocatalysts and photocatalytic activity of the photocatalytic tubular reactor

In the previous section, we used the flow cell setup to validate the deposition and immobilization protocol using PDA followed by a layer-by-layer assembly of PEI and P25. Moreover, we also found that the number of PEI-P25 bilayers significantly affected the amount of P25 being immobilized as well as the absorption of the film. In this section, we implemented the deposition and immobilization protocol to the PFA tubing. Aside from similar dimensions, we maintained the same linear velocity as the one in the flow cell setup in order to preserve a similar fluid phenomenon (e.g., shear force). The “PFA-P255L@PDA” tubing appeared as brownish, mainly to the multiple layers of PEI (Figure 4-9(A)). The thickness of the layer was measured to be approximately 600-700 nm for the “PFA-P255L@PDA” tubing (Figure 4-9(B)). We measured the specific density of P25 using ICP-OES. As shown in Table 4-1, the density of the immobilized P25 increased with the number of layers of PEI-P25 assembly. The highest density of P25 obtained was 0.107 ± 0.009 mg/cm² with the “PEI-P255L@PDA” tubing sample.

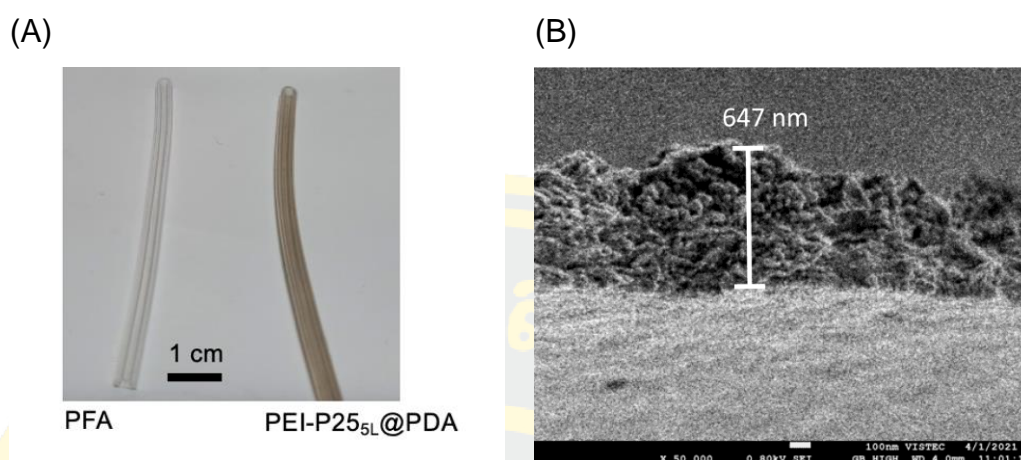


Figure 4 - 9 (A) Photos of the bare and coating PFA tubing (PEI-P25_{5L}@PDA sample), (B) A cross-sectional SEM image showing a thickness of the deposition layers (PEI-P25_{5L}@PDA sample)

Table 4 - 1 Specific densities of P25 of different immobilized tubular samples as estimated from the ICP-OES measurement

Sample	Specific density of P25 (mg/cm ²)
P25@PDA	0.013 ± 0.007
PEI-P25 _{1L} @PDA	0.018 ± 0.004
PEI-P25 _{3L} @PDA	0.071 ± 0.006
PEI-P25 _{5L} @PDA	0.107 ± 0.009

The surface deposited with only PDA (i.e., in the absence of the PEI layer) was not further examined in the tubular setup as it exhibited a very low amount of the immobilized P25. Figure 4-10(A) shows the photocatalytic activities of these tubings. The “PEI-P25_{1L}@PDA” tubing showed very low activity, almost comparable to the sample without photocatalysts (“PEI@PDA” sample). The “PEI-P25_{3L}@PDA” and “PEI-P25_{5L}@PDA” tubing gave significantly higher activities with 27.41% and 37.07%, respectively, thanks to the higher density of the photocatalysts (Figure 4-10(A)). Although the light intensity “PEI-P25_{5L}@PDA” was reduced considerably due

to the absorption of the layers, the electrons and holes at the surface were probably compensated by those that diffused from the inner layers (Zhang et al., 2009). Their activities were also observed to be steady ($< 11.76\%$ RSD) over the course of the experiment (300 mins).

We also performed the photolysis and adsorption experiments to confirm that the decolorization was primarily resulted from the photocatalytic activity of the immobilized P25. For the photolysis experiment, the solution of methylene blue was flowed through a bare tubing (“Bare PFA”) in the absence of deposited PDA, PEI, or immobilized P25. In the adsorption experiment, the solution of methylene blue was flowed through the “PEI-P25_{5L}@PDA” tubing in dark. For all the tests, a steady state was obtained (See appendix B3). Both tests with “Bare PFA” and “PEI-P25_{5L}@PDA” in dark gave much lower activities than the “PEI-P25_{5L}@PDA” under light (Figure 4-10(B)), confirming that the methylene blue disappearance was mainly due to the photocatalytic activity of P25.

In addition, PDA has a broad light absorption, and can be used as a photosensitizer for a photocatalytic reaction (T. Wang et al., 2018). To confirm minimal interferences of PEI and PDA on the photocatalytic activity, the tubings deposited with only “PDA” and “PEI@PDA” were tested under illumination. Their percent decolorization were found to be comparable to that of the adsorption testing (Figure 4-10(B)), implying that PEI and PDA could only adsorb a small portion of methylene blue, but had negligible effects on the photocatalytic activity.

We also examined the effect of the inlet concentration and light intensity, as shown in Figure 4-11. The inlet concentrations exhibited a slight decrease in the percent decolorization at higher inlet methylene blue concentrations. This may be due to the limited available photocatalytic sites. On the other hand, the light intensity has a direct effect on the intrinsic photocatalysis. We found that the percent decolorization increased with increasing intensities of the light source (Figure 4-11(B)). This indicated that our operation was below a photon saturation region (e.g., use of extremely high light intensity). Therefore, the reactor design is particularly important for our operation since the degrees of photon transfer will directly affect the number of incident photons and electron-hole generation events needed for the photocatalytic activity.

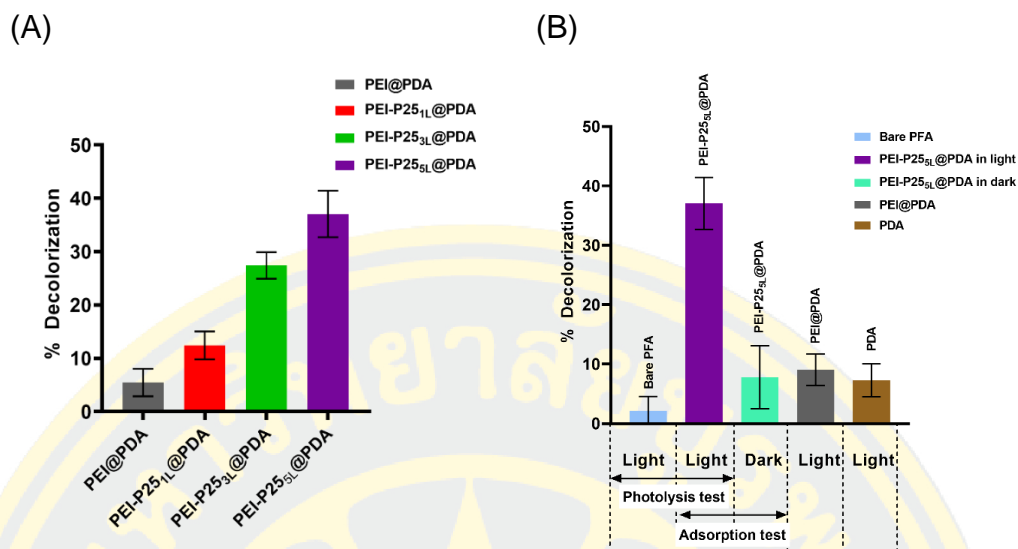


Figure 4 - 10 (A) Photocatalytic activity of different prepared tubings, (B) Photolysis and adsorption tests to validate the photocatalytic activity of the prepared tubing. The experimental condition: a tubular reactor setup, 10-min residence time and 0.0500 mM methylene blue

The degradation was reasonably stable over a continuous operation. According to a previous literature, PDA may undergo photodegradation at some conditions such as high temperature and limited oxygen concentration (T. Wang et al., 2018). However, in our work, such conditions were not implemented, so the degradation of the polymer layers should be minimal. This is in line with our ICP-OES measurement of the reactor effluent, which showed negligible amount of photocatalyst being leached, implying stability of the immobilization matrix. We also found that the photocatalytic activity was also maintained after a repeated use. Nevertheless, it must be noted that the performance of the reused reactor could vary among different reaction conditions. For example, if a pH during the flow reaction is not optimal, the photocatalysts may be prone to be leached due to a weaker coordination with the polymer layers. Therefore, we may observe a decrease in activities over a repeated use of the reactor. Therefore, the reaction conditions should be optimized if the reactor is to be reused.

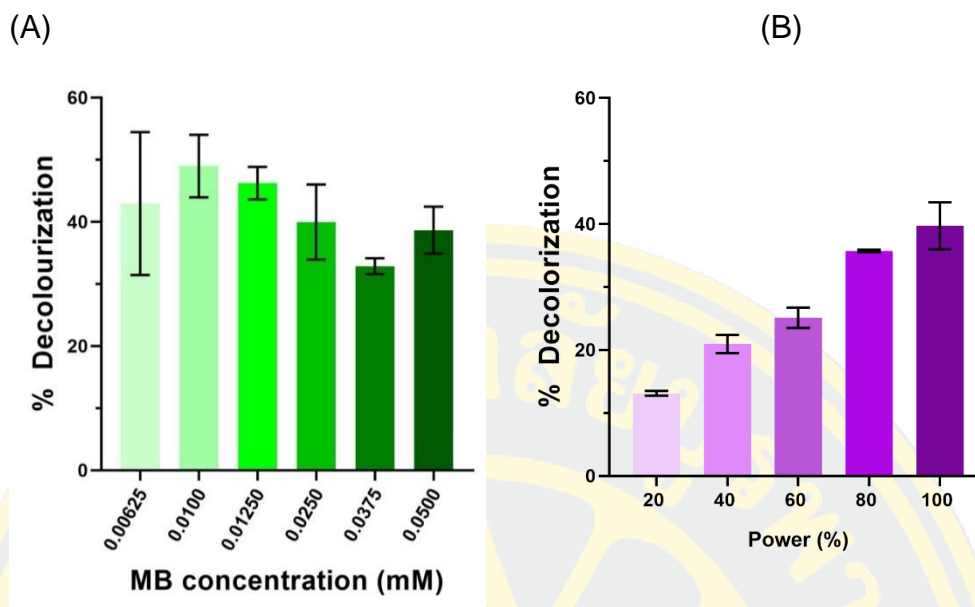


Figure 4 - 11 The effects of (A) inlet methylene blue concentrations and (B) light intensities on photocatalytic activity, as represented by percent decolorization. The maximum power of the light source is 10 W.

If we consider the type of dye, it can be divided into two types: cationic dye and anionic dye, whose decolorization efficiency is influenced by pH. pH has two effects on decolorization. First, dye adsorption; pH can also affect the chemical structure and charge of the dye molecules themselves, influencing their ability to adsorb onto the catalyst surface (Gomathi Devi et al., 2009). Second, in terms of the surface charge of TiO₂, it becomes charged depending on the pH of the solution. At low pH (acidic conditions), the surface is positively charged, attracting negatively charged anionic dyes. While at high pH (alkaline conditions), it becomes negatively charged, attracting positively charged cationic dyes (Awais et al., 2022).

3. Photocatalytic tubular reactor modelling: evaluation of kinetic and adsorption constants

To model this tubular reactor, we consider a steady state species transfer in a cylindrical coordinate. We assume an axial symmetry, meaning that the concentration of a species is independent of the angular position. The flow field is one-dimensional

and fully developed. To justify the latter assumption, we estimate the momentum entrance length ($L_{entrance}$) (Deen, 1998) as:

$$\frac{L_{entrance}}{R} = 1.18 + 0.112Re \quad (4-3)$$

Where R is the radius of the tubular reactor and Re is the Reynolds number. In our setup, the fluid has flowed in a tubing before the reactor section with a much longer distance than the calculated $L_{entrance}$. Therefore, the fully-developed flow field in the tubular reactor is justified (i.e., the axial velocity was independent of the axial position). The species (mass) transfer in the radial direction relies on the molecular diffusion of methylene blue in water while the species transfer in the axial direction occurs via both advection and diffusion. With these assumptions, we can write the species conservation equation as follows:

$$v_z(r) \left(\frac{\partial C_{MB}}{\partial z} \right) = D_{MB} \left(\frac{1}{r} \frac{\partial}{\partial r} \left(r \frac{\partial C_{MB}}{\partial r} \right) + \frac{\partial^2 C_{MB}}{\partial z^2} \right) + R_{V,MB} \quad (4-4)$$

Since the photocatalytic reaction only occurs at the surface, the term related to the reaction within a fluid volume ($R_{V,MB}$) can be neglected. The flow field is a parabolic velocity profile with an average flow velocity of U .

$$2U \left(1 - \left(\frac{r}{R} \right)^2 \right) \left(\frac{\partial C_{MB}}{\partial z} \right) = D_{MB} \left(\frac{1}{r} \frac{\partial}{\partial r} \left(r \frac{\partial C_{MB}}{\partial r} \right) + \frac{\partial^2 C_{MB}}{\partial z^2} \right) \quad (4-5)$$

The first and last terms of the equation represent the advection and diffusion (i.e., dispersion) along the axial direction. To assess the relative importance of the two effects, we formulate the equation into a dimensionless form using dimensionless parameters as defined in Table 4-2:

$$2Pe(1 - \eta^2) \frac{\partial \varphi}{\partial \lambda} = \frac{1}{\theta^2} \left(\frac{1}{\eta^2} \frac{\partial}{\partial \eta} \left(\eta \frac{\partial \varphi}{\partial \eta} \right) \right) + \frac{\partial^2 \varphi}{\partial \lambda^2} \quad (4-6)$$

Table 4 - 2 Definitions of dimensionless numbers

Dimensionless parameter	Definition	Note
ϕ	$\frac{C_{MB}}{C_{in}}$	Dimensionless concentration
λ	$\frac{z}{L}$	Dimensionless axial position
η	$\frac{r}{R}$	Dimensionless radial position
θ	$\frac{R}{L}$	Reactor's aspect ratio
Pe	$\frac{UL}{D_{MB}}$	Peclet number

The *Péclet* number (Pe) is estimated to be in order of 10^3 , implying that the advection dominates over the axial diffusion. Therefore, the axial diffusion term can be neglected from the equation.

$$2U \left(1 - \left(\frac{r}{R}\right)^2\right) \left(\frac{\partial C_{MB}}{\partial z}\right) = D_{MB} \left(\frac{1}{r} \frac{\partial}{\partial r} \left(r \frac{\partial C_{MB}}{\partial r}\right)\right) \quad (4-7)$$

Because the measured concentration of methylene blue is the average value along the axial direction, we convert $C_{MB}(r, z)$ to the bulk concentration or $C_b(z)$ via a velocity-weighted average.

$$C_b(z) = \frac{\int_A C_{MB}(r, z) v_z dA}{\int_A v_z dA} = \frac{\int_0^R C_{MB}(r, z) \cdot 2U \left(1 - \left(\frac{r}{R}\right)^2\right) \cdot 2\pi r dr}{\pi R^2 U} \quad (4-8)$$

We can integrate the left term of Equation (4-5) over $r dr$, and use the definition of the velocity-weighted average to express the term in terms of $C_b(z)$:

$$\int_0^R 2U \left(1 - \left(\frac{r}{R}\right)^2\right) \left(\frac{\partial C_{MB}}{\partial z}\right) r dr = \frac{UR^2}{2} \frac{dC_b}{dz} \quad (4-9)$$

Similarly, we can perform the integration of the right term of Equation (4-5) over rdr as following:

$$\int_0^R D_{MB} \left(\frac{1}{r} \frac{\partial}{\partial r} \left(r \frac{\partial C_{MB}}{\partial r} \right) \right) r dr = R D_{MB} \frac{\partial C_{MB}(R,z)}{\partial r} \quad (4-10)$$

The right term of the Equation (4-5) is related directly to the normal flux at the tube wall. This surface is photocatalytic-active, but impermeable to the species. Therefore, the normal mass transfer flux can be related to the molar rate of degradation in the flow reactor, as represented by a Langmuir-Hinshelwood form (Gora et al., 2006; Nisar et al., 2020).

$$D_{MB} \frac{\partial C_{MB}(R,z)}{\partial r} \cdot (2\pi RL) = - \left(\frac{k_r K C_b}{1 + K C_b} \right) \cdot (2\pi RL) \quad (4-11)$$

k_r indicates the extent of the intrinsic kinetics and the adsorption capacity while K indicates the strength of the adsorption. The equation can be re-arranged to give:

$$D_{MB} \frac{\partial C_{MB}(R,z)}{\partial r} = - \left(\frac{k_r K C_b}{1 + K C_b} \right) \quad (4-12)$$

Combing the forms in Equation (4-7) and Equation (4-10), the species conservation equation becomes:

$$\frac{UR^2}{2} \frac{dC_b}{dz} = -R \left(\frac{k_r K C_b}{1 + K C_b} \right) \quad (4-13)$$

The boundary conditions are $C_b(z = 0) = C_{in}$ and $C_b(z = L) = C_{out}$. Integrating this equation, we can obtain the equation for the methylene blue degradation in this tubular reactor:

$$\frac{\ln\left(\frac{C_{out}}{C_{in}}\right)}{(C_{out} - C_{in})} = \frac{-2k_r KL}{UR} \frac{1}{(C_{out} - C_{in})} - K \quad (4-14)$$

Equation (4-14) has a linear form that allow us to estimate the reaction rate constant (k_r) and adsorption constant (K) from its slope and y-intercept. The results from varying inlet concentrations as discussed previously were used to fit with the tubular reactor model as show in Figure 4-12, the experimental condition: PEI-P255L@PDA reactor, 10 min residence time, 10 W light source (5.830 W/cm² incident intensity), varying inlet methylene concentrations (0.00625 – 0.0500 mM). According to the linear fit, the estimated adsorption constant (K) was 4.111 m³.mol⁻¹, which is independent of the light intensity. The estimated kinetic constants (k_r) were 2.623×10^{-8} , 4.365×10^{-8} , 5.351×10^{-8} , 8.099×10^{-8} , and 8.477×10^{-8} mol.m⁻² s⁻¹ for the incident light intensities of 0.468, 2.048, 3.529, 4.228, and 5.830 W/cm², respectively (light intensities as measured with a photometer, more details: See appendix B5). This revealed the dependence of the intrinsic kinetics on the light intensity (i.e., operating region below photon saturation). These kinetic parameters also represent photo-degradation ability of the system (up to 8.477×10^{-8} mol of methylene blue degraded per m² surface per seconds), which was found to be in a similar order of magnitude to the relevant systems reported in the literature that used a higher light source power(Bosc et al., 2005; Zhou et al., 2015). The parameters are essential for the scale-up of this tubular reactor in the future.

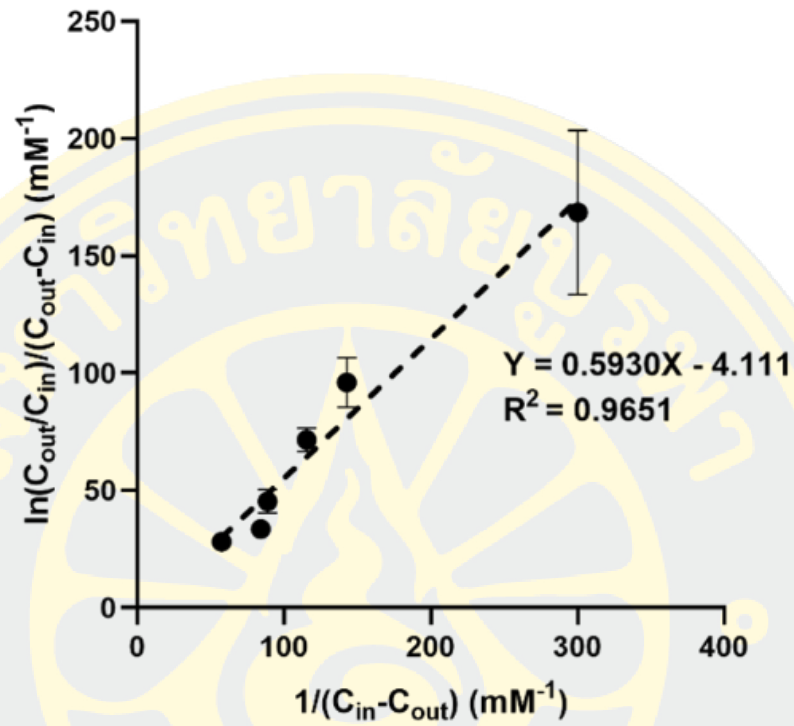


Figure 4 - 12 A representative linear fit was to estimate the kinetic and adsorption parameters from the gradient and intercept.

CHAPTER 5

CONTINUOUS FLOW PHOTOCATALYTIC BENZENE HYDROXYLATION INTO PHENOL IN A FLAT-PLATE REACTOR: DESIGN AND PROCESS OPTIMIZATION

Introduction

Phenol is a widely used precursor for different industrial products ranging from pesticide to dyes to pharmaceuticals (Jin et al., 2019; Knop et al., 1989; Pospíšil, 1988; Schick & Weber, 2001). Phenol can be synthesized by different reactions such as oxidation of benzene and hydrolysis of phenol derivatives. However, the most common process is the cumene process, involving a partial oxidation of cumene (isopropyl benzene), which is produced from the alkylation of benzene with propylene (Pechini, 1967). The products of the cumene process are phenol and acetone, both of which must be in demand to make the process economically feasible. The cumene process suffers from a number of drawbacks including several reactive steps, excessive downstream processing (e.g., fractional distillation and separation), high energy consumption, and use of aggressive chemicals (e.g., strong inorganic acids) (Schmidt, 2005).

Alternatively, phenol can be produced via benzene hydroxylation. This reaction is challenging as phenol is prone to over-oxidation (Figure 5-1). Although multiple oxidants such as H_2O_2 and O_2 have been employed for the thermal catalytic reaction, the reaction exhibits a low selectivity towards phenol. The reactivity of phenol oxidation increases upon heating, so the thermal catalysis is considered unsuitable for this reaction (H. Wang et al., 2022). Photocatalysis emerges as an attractive method (Higashimoto et al., 2023; Wei et al., 2021; Zhang et al., 2011) where photoexcited electron-hole produced (photo)catalyst allows for the generation of radicals (e.g., hydroxyl radicals) required for the hydroxylation. While significant progress has been made in the development of novel photocatalysts for this reaction (Goto & Ogawa, 2016; Han et al., 2023; Han et al., 2022; Ide et al., 2010; Ide et al., 2011; Shiraishi et al., 2005; Yuzawa et al., 2012), new reactor designs have been rarely explored.

Merging heterogeneous photocatalysis and flow chemistry is attractive (Rehm, 2020; Thomson et al., 2020). Heterogeneous photocatalysts facilitate easy catalyst separation, while flow chemistry improves photon transfer and scalability of the process. Recently, there have been developments of various types of flow photoreactors (Sundar & Kanmani, 2020) such as tubular reactors (Khositanon et al., 2022), channel flow reactors (Goto & Ogawa, 2015), packed bed reactors (Claes, Van Gerven, et al., 2021), and spinning disk reactors (Chaudhuri et al., 2022). A flat-plate reactor is a promising option due to its large irradiation area and short photon transmission length. Consequently, it tends to have a uniform light distribution over the cross-section of the reactor (Salvadó-Estivill et al., 2007). The flat-plate reactor is considered as scalable, and has been demonstrated for a production-scale photocatalytic panel system (Nishiyama et al., 2021). Over the past decades, various configurations of flat-plate reactors have been studied. A falling film reactor has one of its surfaces left open to the atmosphere, while a flat-plate reactor is covered with a light-transmitting glazing. Photocatalysts can be used in suspension form (Figure 5-2(A)), immobilized onto the reactor surface (Figure 5-2(B)), or immobilized onto the glazing window (Figure 5-2(C)).

In this work, TiO_2 were immobilized onto the glazing window of the flat-plate reactor using the 3D-printed casting template and smectite clay. The flow streams were well mixed as observed in a computational fluid dynamics simulation. A process condition was optimized by varying residence time, temperature, and light power through a response surface methodology. A mass conservation was formulated to elucidate the transport phenomena and estimate the reaction kinetics.

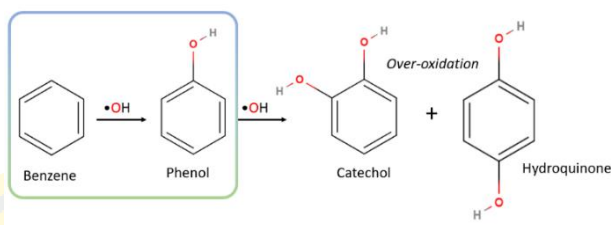
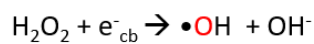
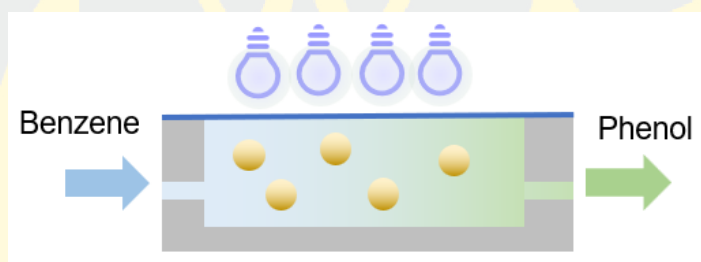


Figure 5 - 1 Mechanism of benzene hydroxylation into phenol via radical formation from H_2O_2 .

(A)



(B)



(C)



Figure 5 - 2 Three configurations of a photocatalytic flat-plate reactor: (A) Photocatalysts as suspensions, (B) Photocatalysts immobilized onto the reactor's surface, (C) Photocatalysts immobilized onto the glazing window.

Methods

1. Material and reagents

Benzene (ACS reagent, 99%), phenol (ACS reagent, 99%), hydroquinone (AR), benzoquinone (AR), Acetonitrile (MeCN) (isocratic grade for HPLC), and titanium dioxide (Degussa P25) were purchased from Sigma-Aldrich. Ultra-pure water was provided by a water purification system, Sartorius arium[®] pro, wherein the electronic conductance was 18.2 MΩ cm. Borosilicate glass plates of 150 mm x 50 mm in size and 3.3 mm in thickness were purchased from Misumi (Thailand). A smectite clay (a synthetic hectorite, Sumecton SWF) was kindly donated by Kunimine Industrial Co., Ltd. All the chemicals were used without purification.

2. Flat-plate reactor design and assembly

The photocatalytic film reactor was designed and in-house constructed with four components, which were made of different materials, as shown in Figure 5-3(A). The top PTFE plate was used to keep the glass surface in place. The glass plate was a light-exposure window on which the photocatalysts were also immobilized. The irradiation area was 30 mm x 100 mm. The subsequent plate was made of a 316 stainless steel, which was etched chemically (Kyosei, Thailand) into a milli-flow channel (30 mm wide, 100 mm long, and 0.5 mm deep). The bottom plate was made of aluminum (grade 6061), serving as a mechanical support for the entire reactor assembly and a heating component in which the heating cartridge (40 W) was inserted.

3. Photocatalyst immobilization onto a glass plate

In this work, TiO₂ (Degussa P25) was selected as a photocatalyst. To simplify the catalyst separation and maximize photon transfer, TiO₂ were immobilized onto a glass plate. TiO₂ suspension was prepared by adding 0.1 g of P25 and 1 mg of a smectite clay in 100 mL water (Deepracha et al., 2019). The suspension was thoroughly stirred, and then sonicated for 1 hour. The glass plate was first cleaned by ethanol and later by HCl to remove any residual contaminant. We found that if the suspension was drop-casted onto the glass plate directly, the immobilized TiO₂ layer would have a non-uniform thickness. To address this issue, we fabricated a 3D-printed template, which consists of multiple triangles (3 mm each side). The TiO₂ suspension was dropped onto the empty space of the template, and let dry overnight. The immobilized TiO₂ layer

onto the glass plate was heated at 60°C for 12 hours. The glass plate with immobilized TiO₂ was obtained (Figure 5-5(B)), and assembled into the flat-plate reactor.

The surface morphology and elemental analysis of the coated glass surfaces were characterized using a JEOL JSM-7610F scanning electron microscope and an energy-dispersive X-ray (EDX) probe, respectively. The SEM images were taken at a low landing energy of 1.5 kV on a gentle-beam high mode. The sheets were platinum-sputtered at 10 mA for 300 s to increase the surface conductivity before the measurement.

We also measured the amount of photocatalysts that could possibly be leached out during the reaction. The effluent samples were collected at time point 6, 12 and 24 h. The samples were digested by microwave (Titan MPS, PerkinElmer) and analyzed by inductively coupled plasma optical Emission spectrometry (ICP-OES) (Optima 8300, PerkinElmer). To prepare the samples for the ICP-OES, 8 mL of nitric acid was added into the effluent samples. Then, 2 mL of hydrogen peroxide was added. The samples were filtrated by a filter paper, added with Type I water to a final volume of 100 mL, and taken to the ICP-OES measurement.

4. Study of process variable via Response Surface Methodology (RSM)

The performance of the reaction can be assessed in terms of the percentage benzene conversion and phenol selectivity, which are considered to be the main dependent variables. Three independent process variables were varied: residence time (A, mins), reaction temperature (B, °C), and light power (C, %). The light power was represented in terms of the percentage of the maximum light power (40W). Design-Expert V13 software was used to perform the DoE. The central composite design (CCD) was employed to generate a set of experimental conditions with five varying levels of each variable ($-\alpha$, -1, 0, +1, $+\alpha$), as in Table 5-1. A total of 20 experimental conditions were generated with six replications at the center point.

Table 5 - 1 Five levels of values for each variable according to CCD

Variable	Symbol	Coded levels				
		$-\alpha$	-1	0	+1	$+\alpha$
Residence time (min)	A	19.8	30	45	60	70.2
Temperature (°C)	B	19.8	30	45	60	70.2
% Light power (%)	C	24.7	40	62.5	85	100

5. Reaction setup and HPLC analysis

The light source was 365-nm UV LED (Figure 5-3(B)) with a maximum power of 40W. The actual light power output could be adjusted by a pulse-width modulation (PWM) LED dimming. The light source was located 5 cm away from the glass surface of the flat-plate reactor (Figure 5-4(A)). The reaction setup is shown in Figure 5-4(B). The residence time was calculated from the reactor volume of 2.25 mL, divided by the volumetric flowrate of the feeding solution. As a base case, the feeding solution consisted of two streams: (1) the 5 mM benzene in acetonitrile and (2) the aqueous 0.5% (v/v) H₂O₂ solution. The volumetric ratio of the two streams was 1:1. As for the start-up of the synthesis, the two streams were first flowed to completely fill the reactor. The temperature control was initiated.

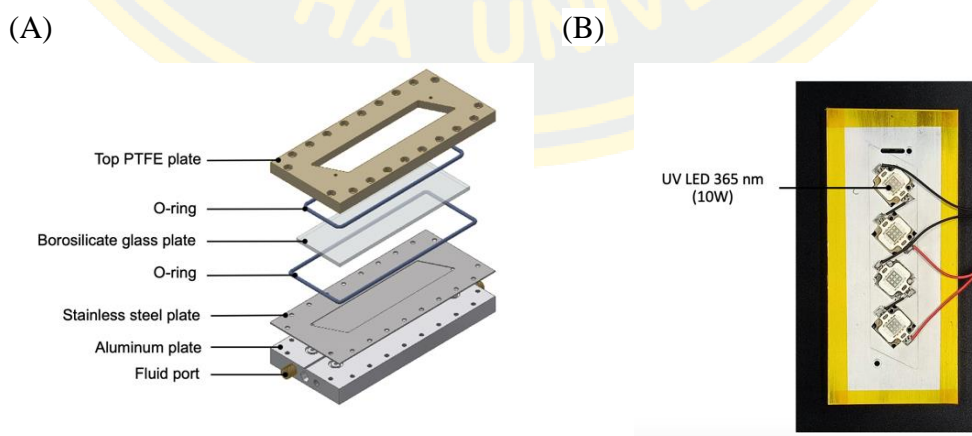
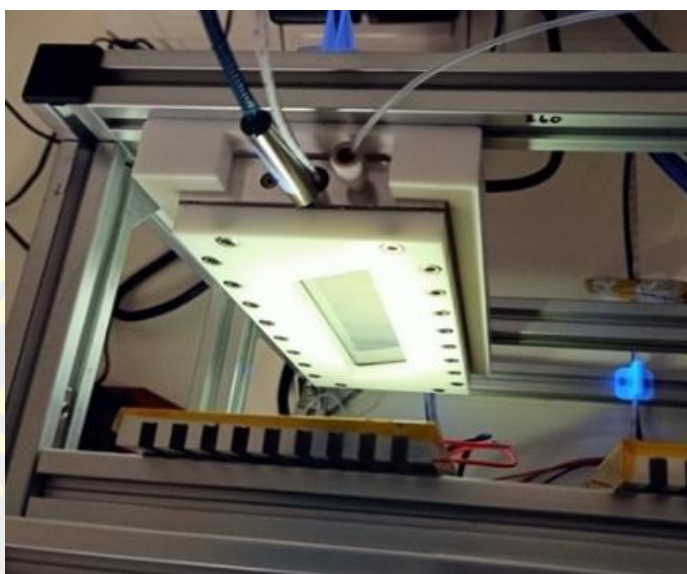


Figure 5 - 3 (A) Components of the flat-plate reactor assembly, (B) UV LED panel.

(A)



(B)

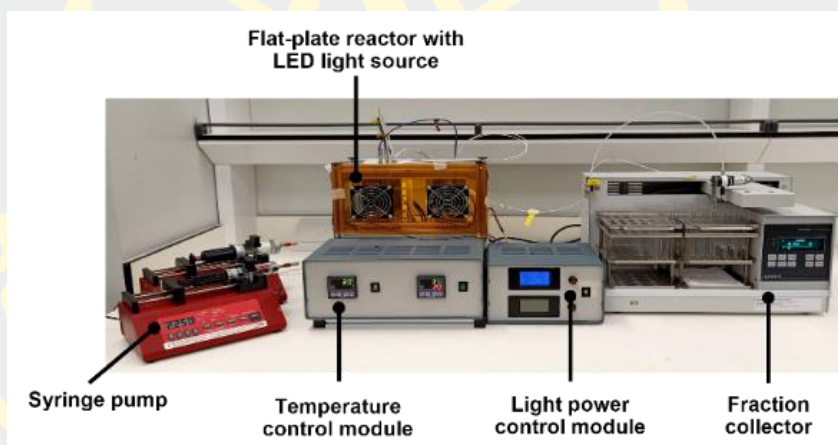


Figure 5 - 4 (A) LED irradiating the flat-plate reactor, (B) Setup of the continuous flow photocatalytic hydroxylation of benzene.

The effluent stream was collected at different time points by a fraction collector in order to ensure a steady state. The effluent stream was analyzed by Agilent 1260 infinity II high performance liquid chromatography (HPLC). The column was ZORBAX Eclipse plus C18 (4.6 x 250 mm, 5 μ m) equipped with guard column (4 x 80 mm, 5 μ m). Benzene and phenol could be detected at wavelengths of 205 and 214 nm, and at retention times of 8.5 and 4.5 min, respectively. The percentage benzene conversion and phenol selectivity could be calculated using the following equations:

$$\% \text{ Benzene conversion} = 1 - \frac{C_{\text{benzene,out}}Q_{\text{out}}}{C_{\text{benzene,in}}Q_{\text{in}}} \times 100 \quad (5-1)$$

$$\% \text{ Phenol selectivity} = \frac{C_{\text{phenol,out}}Q_{\text{out}}}{C_{\text{benzene,in}}Q_{\text{in}} - C_{\text{benzene,out}}Q_{\text{out}}} \times 100 \quad (5-2)$$

Where $C_{\text{benzene,in}}$ and $C_{\text{benzene,out}}$ are the concentrations of benzene in the inlet and effluent (outlet) streams, respectively. $C_{\text{phenol,out}}$ is the concentration of phenol in the effluent (outlet) stream. Q_{in} and Q_{out} are the volumetric flowrates of the inlet and outlet streams, respectively.

6. Characterization of a mixing performance of the two streams

The mixing performance was characterized using SolidWorks (2021). The physical properties of EtOH in the software's database was used while those of IPA and acetonitrile were user-input and obtained from the National Institute of Standards and Technology (NIST) (Lemmon, 2010). The two streams were mixed using a Y-mixer, similar to the actual experimental setup. It was likely that the two miscible streams could be completely mixed in the Y-mixer, before entering the flat-plate reactor. The flow rate of each stream was set to be 0.1125 mL/min, similar to the actual reaction condition. The fluids were assumed to be fully-developed. The outlet pressure was set to be an ambient pressure. The mesh sizes were optimized by comparing the simulation results at different pre-defined mesh levels (1 – 7). Through the simulation, the mass fractions of organic solvents were determined spatially.

Results and discussions

1. Characterization of the immobilized TiO₂ layer on the glass plate

The TiO₂ suspension was drop-casted onto the glass plate, and let it dry at room and oven temperatures. Our previous study (Khositanon et al., 2022) has shown that that the smectite clay affects a rheological behavior of the suspension, and can be used to keep the TiO₂ particles dispersed (Figure 5-5(A)). In addition, the synthetic smectite was selected due to its high elemental purity and its finite nanosized particle (*ca.* 20-100 nm), which allows good transparency and less scattering of light compared to natural smectites for efficient photon penetration.

We also examined the effect of the 3D-printed casting template for the drop casting deposition. As in Figure 5-5(B), when the template was not used, the immobilized TiO_2 layer appeared to be non-uniform. On the other hand, the optimal arrangement of the spaces in the template allowed for even evaporation throughout the surface, with minimal effects of liquid wetting. As a result, homogeneous replicates were observed as a triangular white grid (Figure 5-5(B)), confirming the highly uniform replication of TiO_2 as well as highlighting the potential for constructing shapeable film in more complex design and/or a long-range hybrid film. Microstructure of the TiO_2 layer were investigated by SEM measurement to ensure its homogeneity.

Figure 5-6(A) shows a SEM image of the layer after the drying, indicating a uniform layer of TiO_2 over the glass surface, even at acute angles. The EDX results also verified the uniform distribution of Ti over the surface (See appendix C1) Cross section image of the layer (Figure 5-6(B)) shows the uniform thickness, ranging between 1.38 and 1.57 μm . Upon measuring the weights of the glass plate before and after the immobilization, the photocatalyst loading on the surface was approximately 0.423 mg/cm^2 . The uniformity of the TiO_2 layer was a result of both the well-dispersed TiO_2 suspension in the presence of the clay and the optimal arrangement of the template.

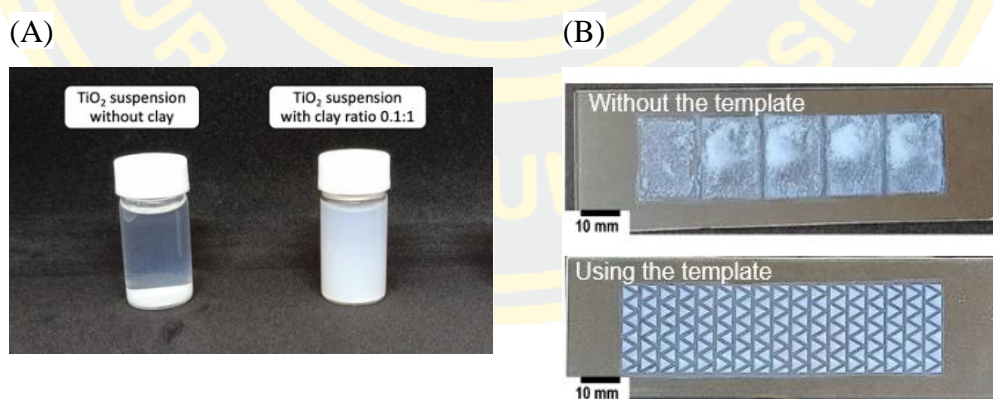


Figure 5 - 5 (A) Images of the TiO_2 suspensions with and without the smectite clay additions after 24 h of settling, (B) Image of the TiO_2 layer on the glass surface with and without the template.

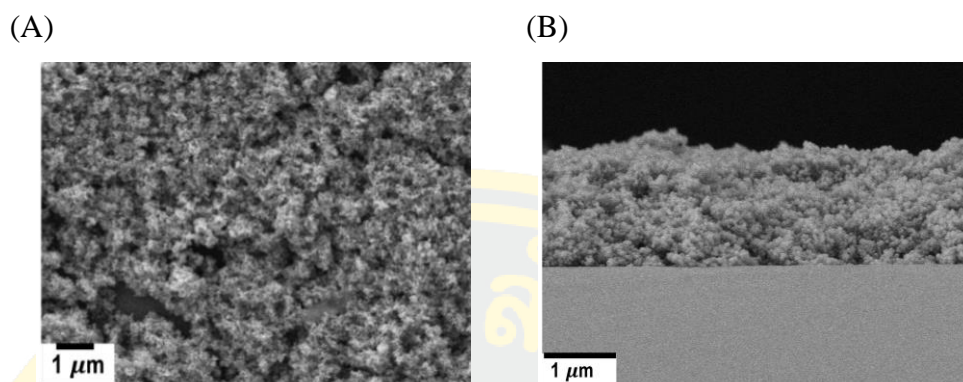


Figure 5 - 6 (A) SEM image of the TiO₂ layer with the clay addition and the use of the template, (B) the cross-section SEM image of the TiO₂ showed a uniform layer thickness of 1.38 – 1.57 μm.

2. Selection of a carrier solvent for benzene and benzene-to-H₂O₂ ratio

Benzene is more soluble in a non-polar solvent while H₂O₂ is in an aqueous solution. Therefore, in order to ensure a homogeneous mixing, we performed the fluid dynamics simulation of the mixing of the benzene solution (in organic solvent) and the aqueous H₂O₂ solution. Choosing the appropriate initial mesh level is crucial for an accurate and efficient flow simulation. As in Figure 5-7, an initial mesh level of 5 was optimal as there is no significant change in the mixing index at higher initial mesh levels (6 and 7). To observe the mixing performance, we plotted the mixing index at the centerline along the reactor's axial position. As in Figure 5-8, the mixing index of 1 was obtained within ~20 mm of length. Acetonitrile (MeCN) exhibits the most effective mixing as compared to IPA and EtOH (See appendix C2). Homogenous mixing of the streams was attained over the length of the reactor.

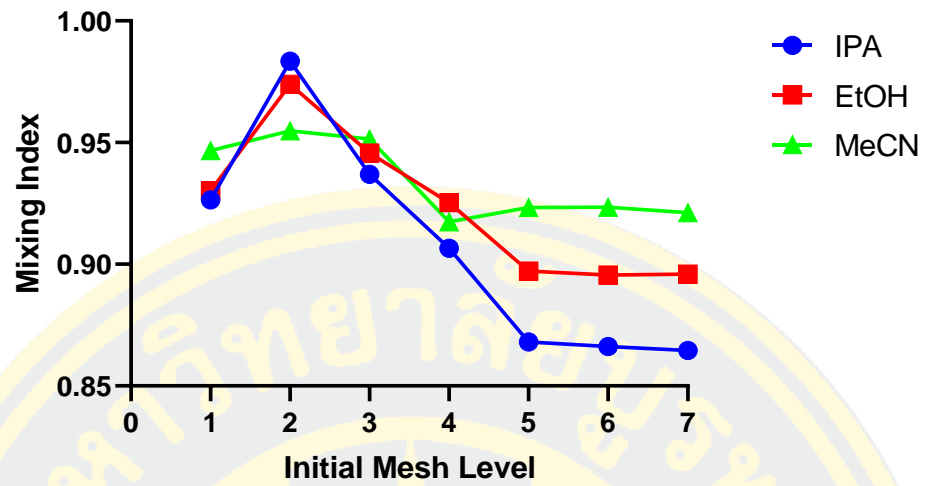


Figure 5 - 7 The simulation result in terms of the mixing index at different initial mesh levels (1 – 7)

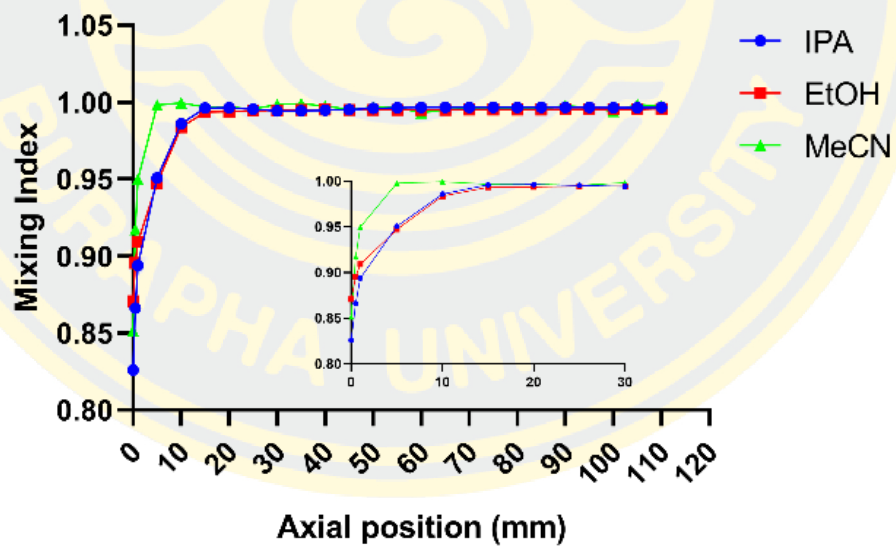


Figure 5 - 8 The mixing index at the centerline along the length of the reactor.

The choice of the solvent may also influence the stability of the immobilized photocatalyst film. The smectite clay typically prefers to disperse in water. According to the ICP-OES measurement, less than 10 mg/L of Ti was observed for all the effluent samples collected from the flow reactor, indicating that the film was stable, and the photocatalyst leaching was negligible. Acetonitrile has also been reported to suppress the over-oxidation of phenol.(Z. Wang et al., 2022) Therefore, we used acetonitrile as a carrier solvent for benzene.

Subsequently, the ratios of the feeding of the benzene and H₂O₂ solutions were varied and optimized. Reaction condition: residence time of 30 mins, 25 °C, 40 W light power, varying volumetric flow ratios of the benzene and H₂O₂ solutions. The reaction reached a steady state within three residence times, as shown in Figure 5-9 and Figure 5-10, after turning on the light source. We found that a higher amount of H₂O₂ added led to a higher percentage conversion of benzene. As in Table 5-2, with the ratio of benzene to H₂O₂ being 1:4, the conversion of 95.97% was obtained. However, when a high amount of H₂O₂ was added, phenol selectivity dropped as excess amount of H₂O₂ could cause an over-oxidation of phenol to form other undesired side products.

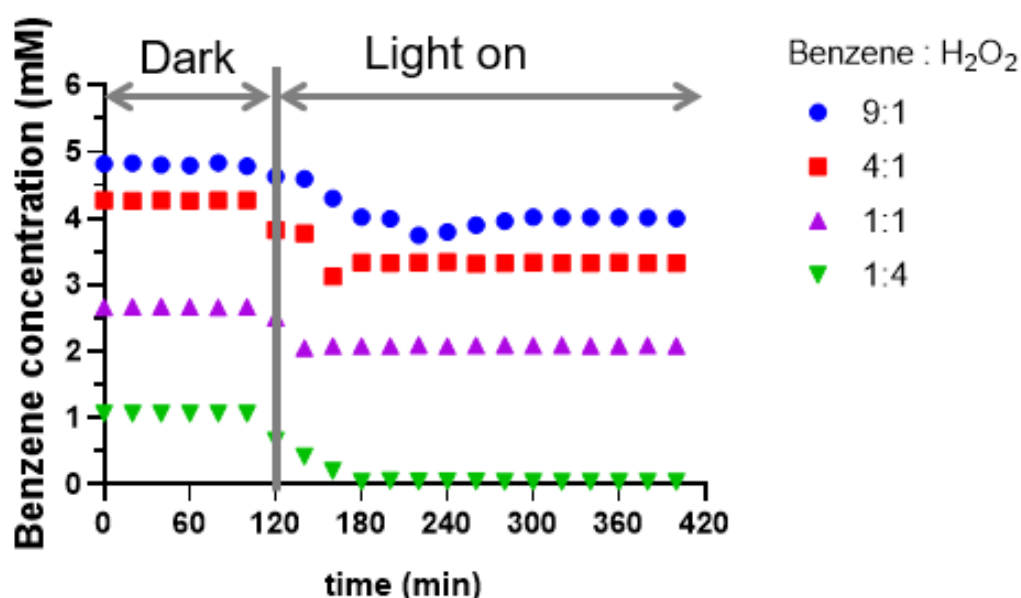


Figure 5 - 9 The progress of reaction over the time course of benzene concentration

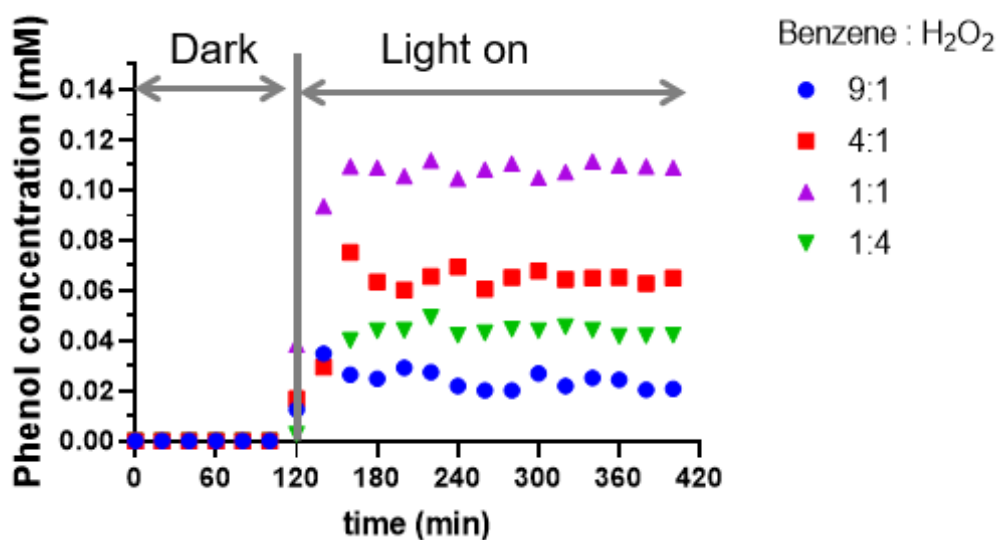


Figure 5 - 10 The progress of reaction over the time course of phenol concentration.

Table 5 - 2 Percentage benzene conversion and phenol selectivity at different feeding benzene to H₂O₂ ratios. Reaction condition: residence time of 30 mins, 25 °C, 40 W light power

Benzene: H ₂ O ₂ ratio	% Benzene conversion	% Phenol selectivity
9:1	16.68%	2.60%
4 :1	21.96%	6.93%
1:1	21.70%	18.80%
1:4	95.97%	6.28%

3. Study of process variable via Response Surface Methodology (RSM)

In this study, the volumetric feeding ratio of benzene to H_2O_2 was maintained constant at 1:1. Three important process variables were varied: residence time (A), reaction temperature (B), and % light power (C) (See appendix C3 for the measured light intensities). Response surface methodology was performed to examine the interactions between these variables, determine the statistically significant variables, and obtain the equations to predict the benzene conversion and phenol selectivity for a given process conditions.

The two models, describing conversion and selectivity, showed low p-values (<0.05), meaning they were statically significant. As in Table 5-3, for the benzene conversion, all variables have p-values of less than 0.05, meaning that they were statistically significant. The high R-square and adjusted R-square values (0.9300 and 0.9796, respectively) also indicate that the model was in a good fit with the data. For the phenol selectivity, only the temperature was statistically insignificant, with the p-value of 0.8990 (>0.05). However, the high R-square and adjusted R-square values (0.9697 and 0.9542, respectively) indicate that the model was in a good fit with the data (See appendix C4)

The residence times exhibit an apparent effect on both the conversion and selectivity. As in Figure 5-11, the benzene conversion increased from 20.14% to 33.39% when the residence time was increased from 30 to 60 mins. On the other hand, the phenol selectivity decreased from 34.05% to 18.03%. The drop in the phenol selectivity was due to the over-oxidation of phenols to other side products such as benzoquinone, hydroquinone, and catechol (Bui et al., 2011; Haseneder, 2014). This also emphasizes an importance of the flow reactor, which tends to have a narrow residence time distribution than the stirred batch reactor. Therefore, the reaction time can be precisely controlled with the flow reactor.

Table 5 - 3 ANOVA results of the percentage benzene conversion and phenol selectivity (A = Residence time, B = Temperature, C = Percent light power)

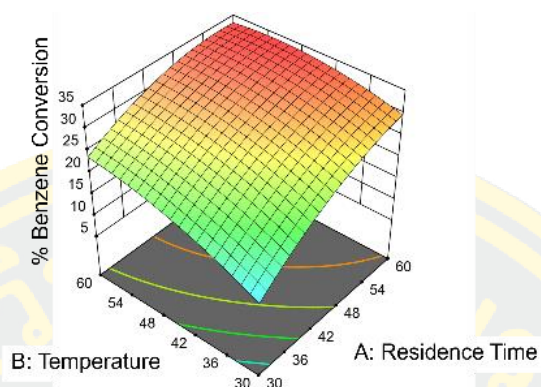
Response		p-value	Response		p-value
Benzene conversion	Model	< 0.0001	Phenol selectivity	Model	< 0.0001
	A-RT	< 0.0001		A-RT	< 0.0001
	B-Temp.	< 0.0001		B-Temp.	0.8990
	C-% lamp power	0.0060		C-% lamp power	0.0300
	AB	0.0009		AB	0.0080
	AC	< 0.0001		AC	0.0197
	BC	0.0156		BC	0.0101
	A ²	< 0.0001		A ²	< 0.0001
	B ²	< 0.0001		B ²	0.3438
C ²	< 0.0001	C ²	0.0016		

Despite being rarely examined in most previous works, a reaction temperature was another interesting variable to be studied in this work. Different temperatures can result in a different photocatalytic activity. At a high temperature, electron-hole pairs become more active, allowing electrons to combine with absorbed water or oxygen molecules faster and holes to generate hydroxyl radicals faster (Ide et al., 2012). However, if the temperature was too high, it might also have a detrimental effect on the reaction rate as previously shown for the photocatalytic dye degradation by Pd/Cu-TiO₂ (Meng et al., 2017). In our study, we also found that heating the reactor to 60°C enhanced the benzene conversion. It is worth noting that the evaporation of benzene, a high vapor pressure compound, could be avoided thanks to the advantage of a flow reactor, ensuring the disappearance of benzene by photocatalysis. Nevertheless, the phenol selectivity seemed not to be affected by the change in temperature (between 30 and 60°C).

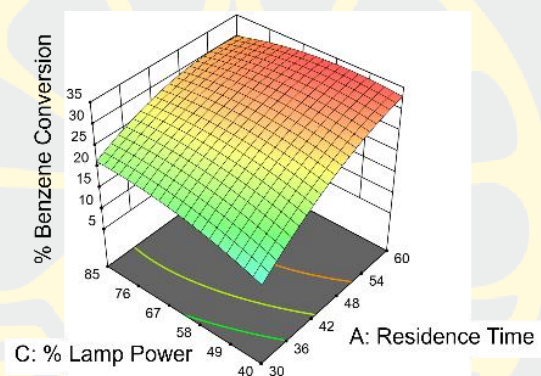
The light power could be adjusted by the PWM LED dimming module. As in Figure 5-11, the benzene conversion increased only slightly when the percentage of the light power was adjusted from 40% to 85%. This demonstrated that the light intensity was already sufficient for the photocatalytic activity of this reaction. Similarly, the light power also had a minor effect on the phenol selectivity. As in Figure 5-12 The phenol selectivity slightly decreased from 24.42% to 21.48% when the light power was increased from 40% to 85%. The RSM mappings depict the effects of interacting variables on the two responses: conversion and selectivity (Figure 5-11 and Figure 5-12).

% Benzene conversion

(A)



(B)



(C)

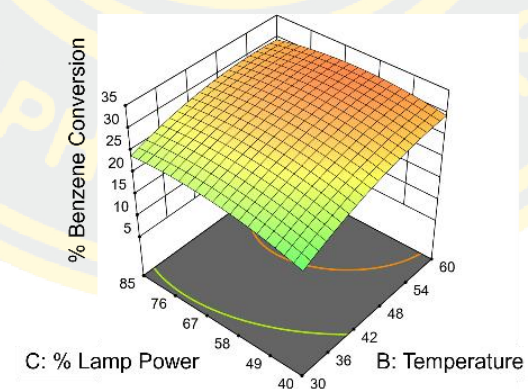
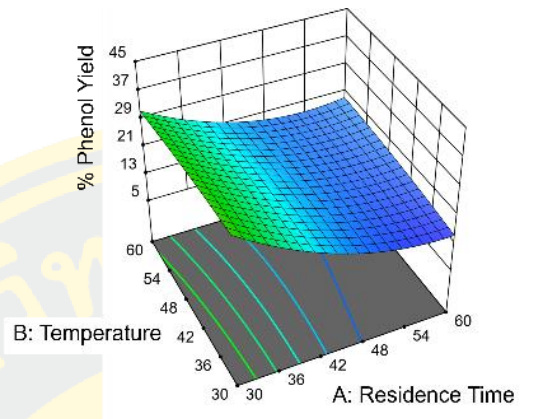


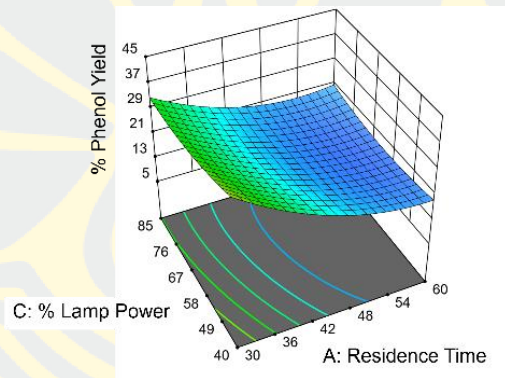
Figure 5 - 11 Three-dimensional response surface plot for the effects of temperature, residence time and light power on the conversion of the benzene hydroxylation to phenol

% Phenol selectivity

(A)



(B)



(C)

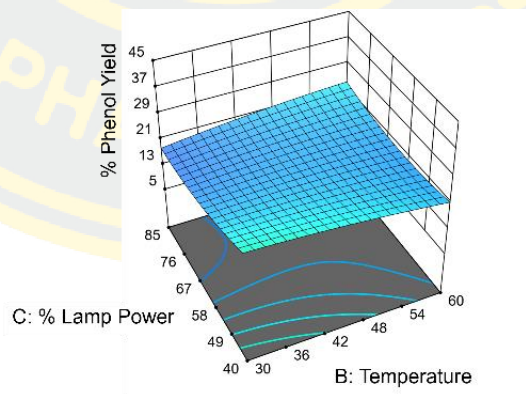


Figure 5 - 12 Three-dimensional response surface plot for the effects of temperature, residence time and light power on the selectivity of phenol

In addition, we obtained the prediction equations for the benzene conversion and the phenol selectivity. The response surfaces were generated to observe the effects of single variables as well as the effects of interacting variables.

$$y_{benzene\ conv.} = -107.35882 + 2.41979A + 1.53621B + 0.999018C - 0.007816AB \\ - 0.007498AC - 0.003277BC - 0.012910A^2 - 0.008145B^2 - 0.003754C^2 \quad (5-3)$$

$$y_{phenol\ selec.} = 162.43159 - 3.44327A - 0.649439B - 1.13138C + 0.009957AB + 0.005580AC \\ + 0.006369BC + 0.023358A^2 - 0.002236B^2 + 0.004282C^2 \quad (5-4)$$

The response surface equations can be used to predict optimal conditions for achieving a high conversion and/or a high selectivity. For maximizing the conversion, the reaction was suggested to operate at 49.4 mins of residence time, 50.5 °C, and 100% light power (40W), which could result in 26.7% conversion. For maximizing the selectivity, the reaction was suggested to operate at 19.8 mins of residence time, 41.7 °C, and 100% light power (40W), which could result in 47.6% selectivity. To maximize the yield, the conversion and selectivity must be compromised. At 24.9 mins of residence time, 61.6 °C, and 100% light power (40W), 20.1% conversion and 40.8% selectivity could be obtained. The response surface methodology has facilitated the process optimization, and significantly increased the conversion and selectivity from the original result obtained before the optimization (as previously shown in Table 5-2).

4. Transport phenomena formulation and reaction kinetic parameters

In order to elucidate the kinetics inside the flow reactor, we formulated a steady-state transport phenomena, based on the assumption that the fluid flow was in a laminar regime. We assume that there is no edge effect on the z direction. The reactor is modelled in a cartesian coordinate system, as shown in Figure 5-13.

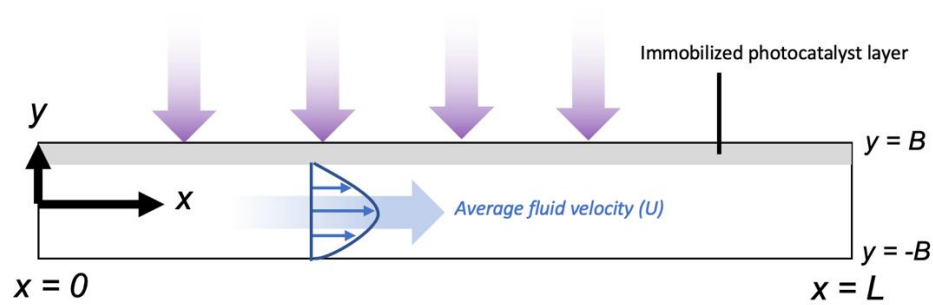


Figure 5 - 13 A drawing of the reactor in a cartesian coordinate system for the transport phenomena modelling

By calculating the momentum entrance length similar to our previous study (Khositanon et al., 2022), we can justify that the flow field is one-dimensional and fully developed. The mass transfer of benzene primarily relies on the molecular diffusion in the y direction. The advection and diffusion of benzene also occurs in the axial (x) direction. Given these assumptions, the species conservation equation can be written as follows:

$$v_x(y) \frac{\partial c_i}{\partial x} = D_i \left(\frac{\partial^2 c_i}{\partial x^2} + \frac{\partial^2 c_i}{\partial y^2} \right) + R_{v,i} \quad (5-5)$$

The photocatalytic only happens at the top surface. Therefore, the reaction rate within a fluid volume can be assumed to be negligible. The flow field is parabolic, and can be related to an average flow velocity (U).

$$\frac{3}{2} U \left(1 - \left(\frac{y}{B} \right)^2 \right) \frac{\partial c_i}{\partial x} = D_i \left(\frac{\partial^2 c_i}{\partial x^2} + \frac{\partial^2 c_i}{\partial y^2} \right) \quad (5-6)$$

To evaluate the importance of the advection and diffusion along the axial direction, the species conservation equation is transformed into a dimensionless form (Table 5-4):

Table 5 - 4 Dimensionless parameters for the formulation of the transport phenomena inside the flat-plate reactor

dimensionless parameter	definition	note
ϕ	C_i/C_{in}	dimensionless concentration of benzene
λ	x/L	dimensionless axial position
η	y/B	dimensionless transverse position
θ	B/L	reactor's aspect ratio
Pe	UL/D_i	Péclet number

$$\frac{3}{2} Pe(1 - \eta^2) \left(\frac{\partial \phi}{\partial \lambda} \right) - \frac{\partial^2 \phi}{\partial \lambda^2} = \left(\frac{1}{\theta^2} \right) \frac{\partial^2 \phi}{\partial \eta^2} \quad (5-7)$$

The Péclet number is greater than 10^3 , meaning that the advection is a dominant mass transfer mode, so the second term on the left can be neglected. We can therefore reduce the Equation (5-8) to only two terms, as follows:

$$\frac{3}{2} U \left(1 - \left(\frac{y}{B} \right)^2 \right) \frac{\partial C_i}{\partial x} = D_i \frac{\partial^2 C_i}{\partial y^2} \quad (5-8)$$

Then, we convert $C_i(x, y)$ to the velocity-averaged bulk concentration of benzene or $C_b(x)$ (Deen, 1998). This involves the surface integral over the cross section of the reactor.

$$C_b(x) = \frac{\int_{-B}^B \int_0^L C_i(x, y) v_x dx dy}{\int_{-B}^B \int_0^L v_x dx dy} \quad (5-9)$$

We can integrate the left term of Equation (5-8) over dy and use to the definition of the bulk concentration to transform the term.

$$\int_{-B}^B \frac{3}{2} U \left(1 - \left(\frac{y}{B} \right)^2 \right) \frac{\partial C_i}{\partial x} dy = 2BU \frac{dC_b}{dx} \quad (5-10)$$

Similarly, we can integrate the right term of Equation (5-8) over dy and perform the definite integral from $-B$ to B .

$$\int_{-B}^B D_i \frac{\partial^2 C_i}{\partial y^2} dy = D_i \frac{\partial C_i(x,B)}{\partial y} - D_i \frac{\partial C_i(x,-B)}{\partial y} \quad (5-11)$$

The last term represents the mass transfer flux in the y direction at the bottom surface of the reactor ($y = -B$), which is an impermeable solid without any photocatalyst. Therefore, we can assume that the last term is negligible. On the other hand, the flux at $y = B$ refers to the mass transfer flux at the top surface, where the photocatalytic reaction occurs. This flux can be related to the kinetics of the heterogeneously catalytic reaction, which can be described by the Langmuir-Hinshelwood model.

$$D_i \frac{\partial C_i(x,B)}{\partial y} = \frac{-k_r K C_b}{1 + K C_b} \quad (5-12)$$

We can now replace the terms in Equation (5-8) with the terms in Equations (5-10) and (5-12).

$$2BU \frac{dC_b}{dx} = \frac{-k_r K C_b}{1 + K C_b} \quad (5-13)$$

The definite integral of Equations (5-13) from $x = 0$ to $x = L$ gives an analytical solution as shown in Equation (5-14).

$$\frac{\ln\left(\frac{C_{benzene,out}}{C_{benzene,in}}\right)}{(C_{benzene,out} - C_{benzene,in})} = \frac{-k_r K L}{2BU(C_{benzene,out} - C_{benzene,in})} - K \quad (5-14)$$

Where $C_{benzene,in}$ and $C_{benzene,out}$ the benzene concentrations in the inlet and outlet streams, respectively. k_r and K are the intrinsic kinetic parameter and the adsorption constant, respectively. B is half of the fluid flat-plate reactor's thickness. U is the mean fluid velocity.

The reaction data, namely the benzene concentrations in the inlet and outlet streams, were used to fit the reaction kinetic equation. We selected the condition from Entry 18 (See appendix C5) as a basis for this kinetic analysis. From the data fitting in Figure 5-14, the kinetic and adsorption parameters can be obtained from the slope and intercept of the fitting line. The adsorption constant (K) was found to be $0.0535 \text{ m}^3 \text{ mol}^{-1}$. The intrinsic kinetic parameter (k_r) was found to be $8.21 \times 10^{-6} \text{ mol m}^{-2} \text{ s}^{-1}$.

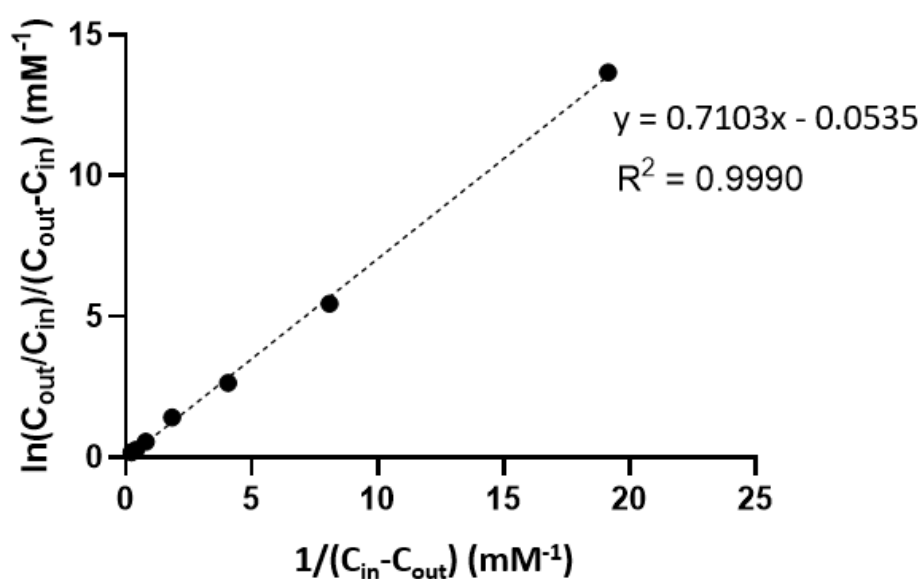


Figure 5 - 14 A linear fit to the reaction data to estimate the kinetic and adsorption constants of the photocatalytic benzene conversion in the flat-plate reactor. Reaction condition: residence time of 19.8 mins, 45 °C, 62.5% light power (25 W)

In order to benchmark the performance of our flat-plate reactor with previous batch setups demonstrated for the benzene hydroxylation, the photocatalytic space-time yield (PSTY) was estimated to. The PSTY was calculated using the Equation (5) and (6) for the batch and continuous reactors, respectively (Kayahan et al., 2020):

$$PSTY \left(\frac{\text{mol}}{\text{Ws}} \right) = \frac{n_{phenol}}{t \cdot P} \quad (5-15)$$

$$PSTY \left(\frac{\text{mol}}{\text{Ws}} \right) = \frac{C_{phenol} V_{reactor}}{\tau \cdot P} \quad (5-16)$$

Where n_{phenol} is the amount of phenol produced in the batch reactor (mol), $V_{reactor}$ is the flow reactor volume (m^3), t is the reaction time (s), τ is the residence time (s), and P is the light power (W). The space-time yield describes the amount of product formed within the reaction or residence time, present in the applied reaction volume. For photoreactors, it is essential to include the term of light power. As in Table 5-5, the PSTY of the flat-plate reactor in this study was 1-2 orders of magnitude higher than those of the batch photoreactors. Note that we selected the study with TiO_2 or P25 as photocatalysts to avoid other effects of photocatalysts.

Table 5 - 5 Comparison of the photocatalytic benzene hydroxylation in different setups, particularly in terms of the PSTY

Reactor setup	% Conversion	% Selectivity	% Yield	PSTY (mol/W.s)	Reference
Batch, 24 h, TiO ₂ , 400W	0.3%	100.0%	0.3%	9.74×10^{-13}	(Devaraji et al., 2014)
Batch, 3 h, P25, 300W	3.8%	70.0%	2.6%	1.72×10^{-12}	(Li et al., 2020)
Batch, 21 h, P25, 300W	31.8%	28.9%	9.2%	2.64×10^{-12}	(Z. Wang et al., 2022)
Batch, 2 h, TiO ₂ , 300W	69.3%	15.8%	10.9%	1.53×10^{-13}	(Zhang et al., 2011)
Flat-plate reactor, 19.8 mins, P25, 25W	10.62%	50.41%	5.35%	1.20×10^{-11}	(Entry 18, this study)

CHAPTER 6

CONCLUSION

The work in this thesis has focused on the continuous-flow system that is relevant to heterogeneous catalysis, from the synthesis and purification of metal nanoparticles to the development of reactors with immobilized heterogeneous catalysts. The conclusions of different work in this thesis can be summarized as below:

1. The continuous silver nanoparticle synthesis and purification
 - We showed that solvent extraction method is non-destructive to the nanoparticles, maintaining their morphology as well as physical properties such as light absorption.
 - We demonstrated that this method could remove the ligands in the solution in a significant level (~56.7% extraction, in the experiment with a volumetric ratio of 1:3 for the unpurified sample to the solvent). Further removal of ligands are achieved through higher extraction solvent usage or cascading of extraction.
 - This method was also demonstrated as an in-line purification after the flow synthesis of AgNPs. About 73.3% removal of ligands was obtained during continuous production of AgNPs. Therefore, this continuous-flow purification can potentially replace the conventional methods that are time-consuming and laborious.
2. The continuous-flow photocatalytic degradation of methylene blue using a tubular reactor made of PFA with dopamine-assisted immobilization of photocatalysts
 - We successfully demonstrated the use of PDA and PEI for immobilizing TiO₂-P25 (P25) onto the wall of the PFA tubing.
 - The FTIR spectra confirmed the presence of the deposited PDA and PEI, while the SEM/EDX verified the immobilization of P25.
 - A higher density of P25 was achieved through a layer-by-layer assembly of PEI-P25, with the highest loading being 0.107 ± 0.009 mg/cm² for

the five bilayers, which also gave the highest activity of 37.07% of MB decolorization (a residence time of 10 min).

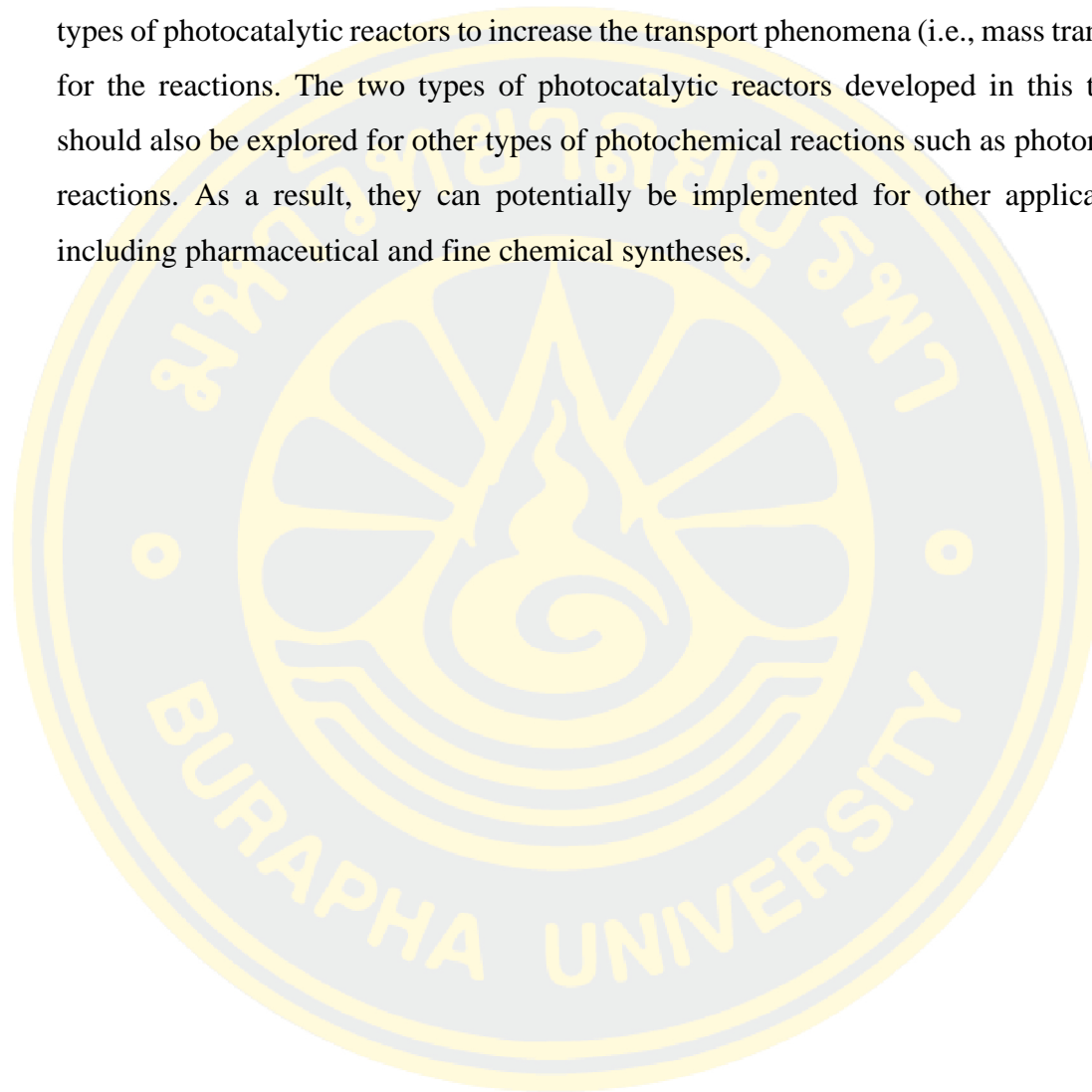
- This simple fabrication from a commercially available tubing opens up considerable opportunities for continuous flow photocatalytic applications.
3. The continuous-flow photocatalytic benzene hydroxylation in a plate reactor
- The smectite clay, with high transparency and low light scattering, and the casting template were keys to the uniform immobilization of P25 over the glass surface.
 - Acetonitrile was an optimal carrier solvent for benzene given the high mixing efficiency with the aqueous H₂O₂ solution.
 - According to RSM, the optimal condition for a high phenol yield was a moderate residence time (24.9 mins) and a relatively high temperature (61.6 °C).
 - The transport phenomena formulation gave the adsorption constant of 0.0535 m³/mol and the intrinsic kinetic constant of 8.21×10^{-6} mol/(m².s).
 - Our flat-plate reactor was promising with a high photocatalytic space-time yield (1.20×10^{-11} mol/W.s), which is 1-2 orders of magnitude higher than the reported batch reactor setups.

Future work

Overall, this thesis has achieved developments of the continuous-flow systems that involve use of heterogeneous catalysts. Nevertheless, there are future works that can be studied further for making these technologies practical for real implementations:

For the continuous-flow synthesis and purification of metal nanoparticles, this technology can be implemented for continuous productions of nanoparticles. However, in order to make it feasible, the degree of separation has to be improved. This can be done by constructing a multi-stage separation setup and employing a highly selective extractant. Different designs of the membrane-based separator should also be explored to increase the productivity of the separation for a large scale production.

For the continuous-flow setups of the photocatalytic reactions, further study on the surface modifications can be performed to increase a loading of immobilized photocatalyst while maintaining a high light transparency. Future work can also focus on applying the immobilization protocols (i.e., dopamine-assisted, clay-based) for other types of photocatalytic reactors to increase the transport phenomena (i.e., mass transfer) for the reactions. The two types of photocatalytic reactors developed in this thesis should also be explored for other types of photochemical reactions such as photoredox reactions. As a result, they can potentially be implemented for other applications including pharmaceutical and fine chemical syntheses.



APPENDIX A

A1 Surface characterization of silver nanoparticles

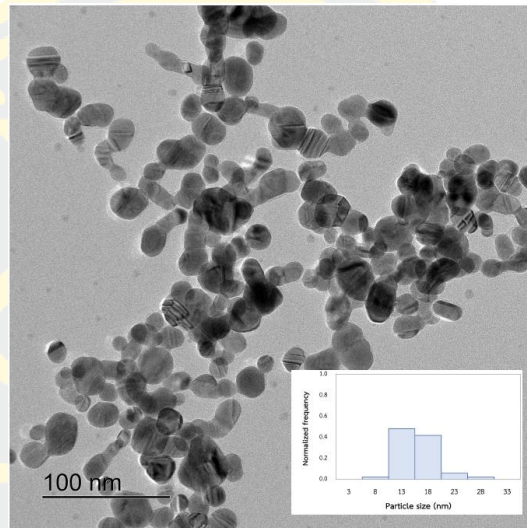


Figure A-1 The TEM image of the SE1:3 sample

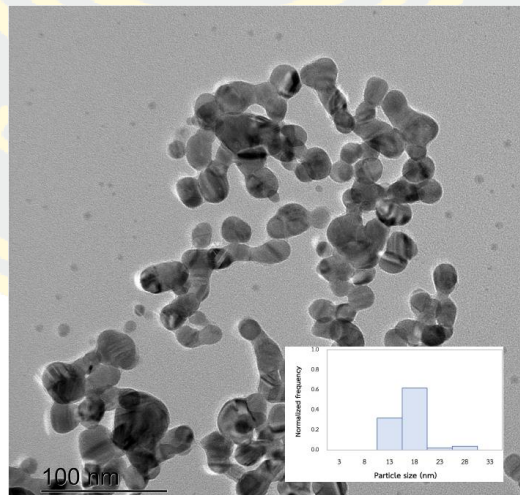


Figure A-2 The TEM image of the F1:3 sample

A2 The ^1H -NMR spectra of silver nanoparticle samples

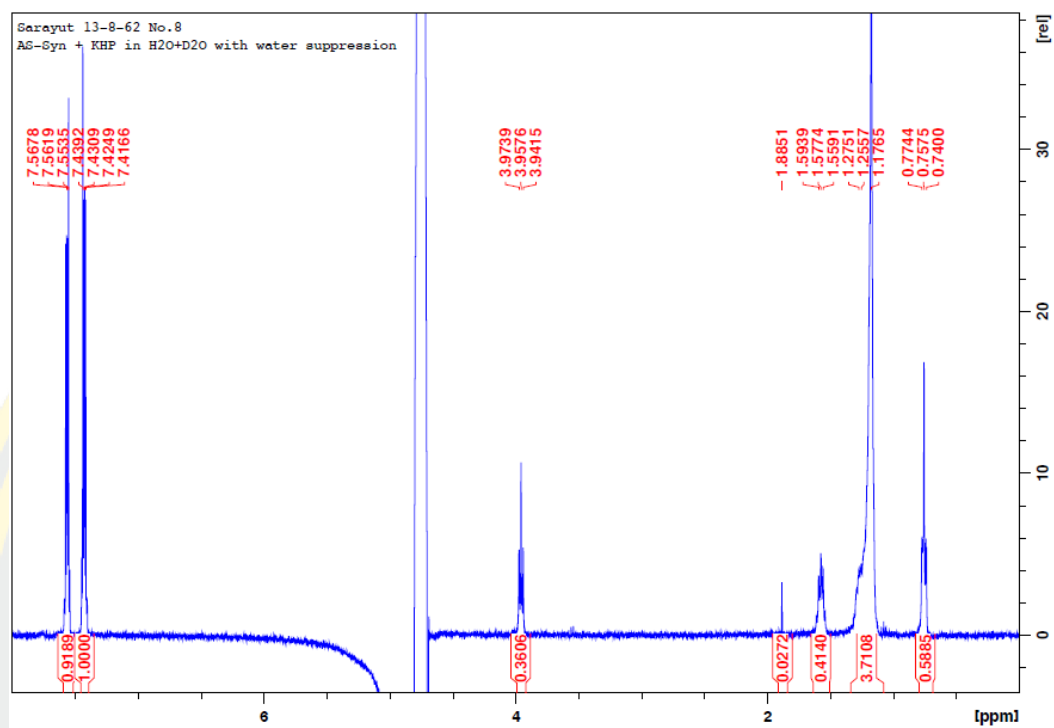


Figure A-3 The ^1H -NMR spectra of the as-syn sample

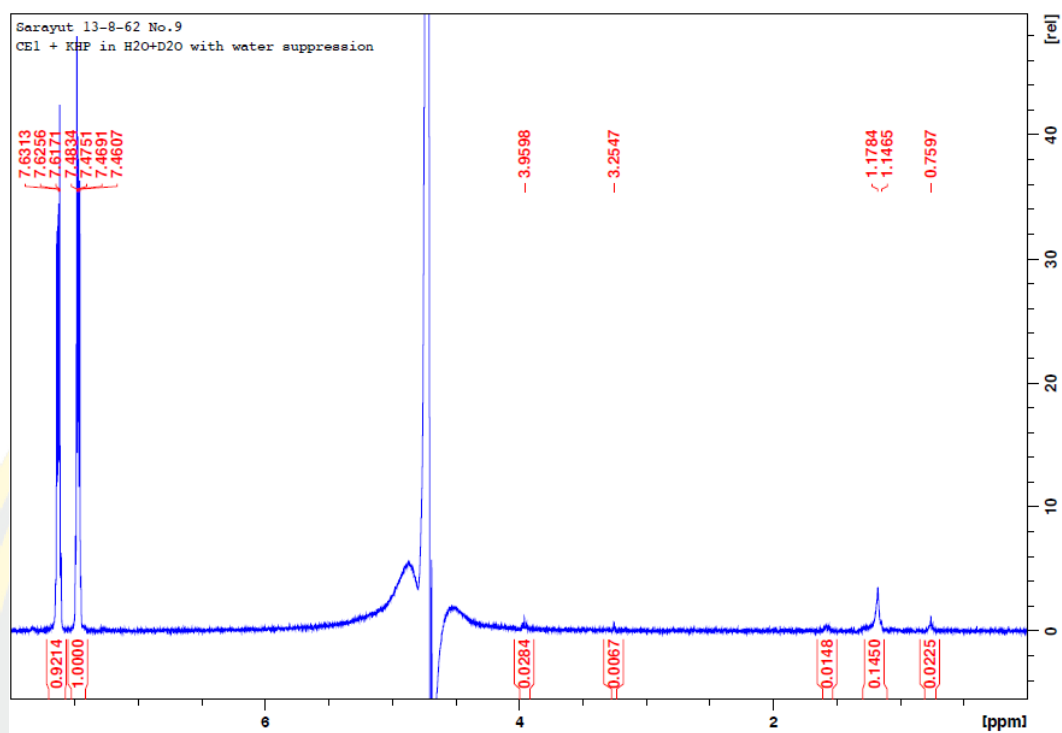


Figure A-4 The ¹H-NMR spectra of the PR1 sample

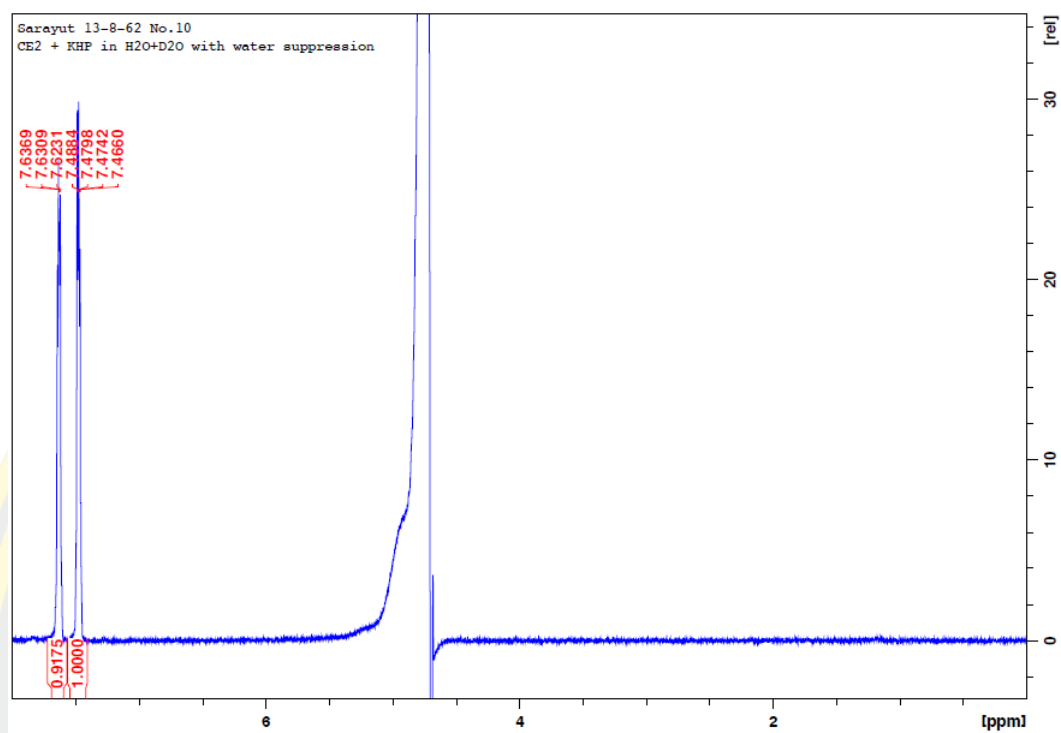


Figure A-5 The ^1H -NMR spectra of the PR2 sample

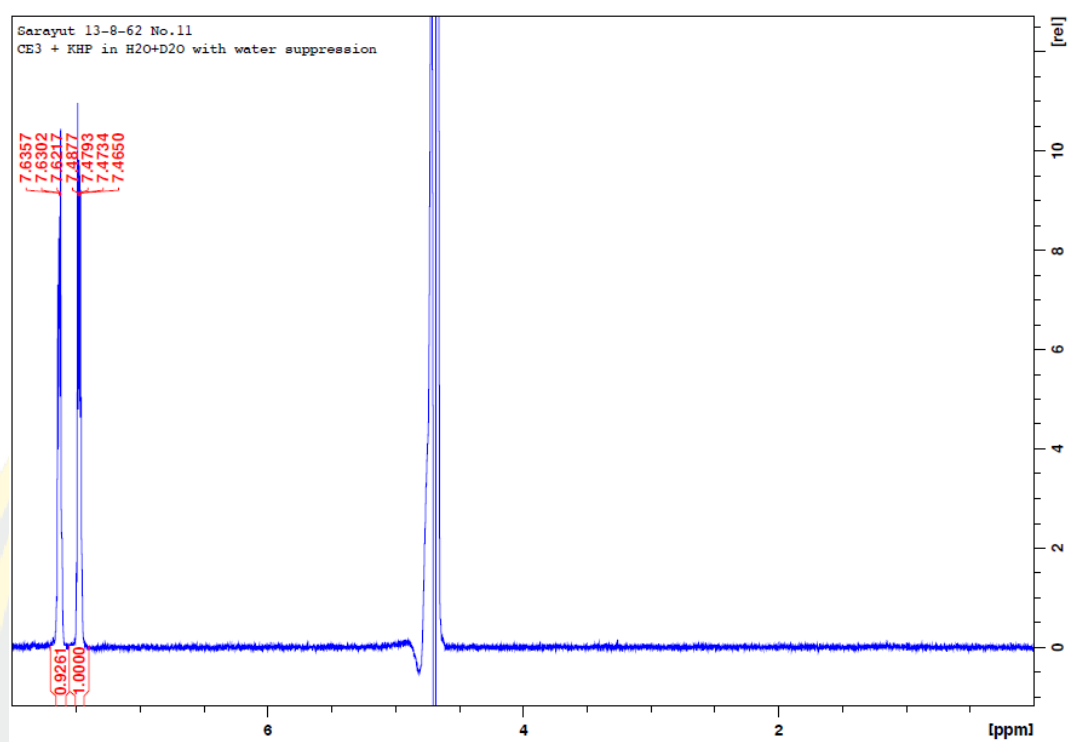


Figure A-6 The ¹H-NMR spectra of the PR3 sample

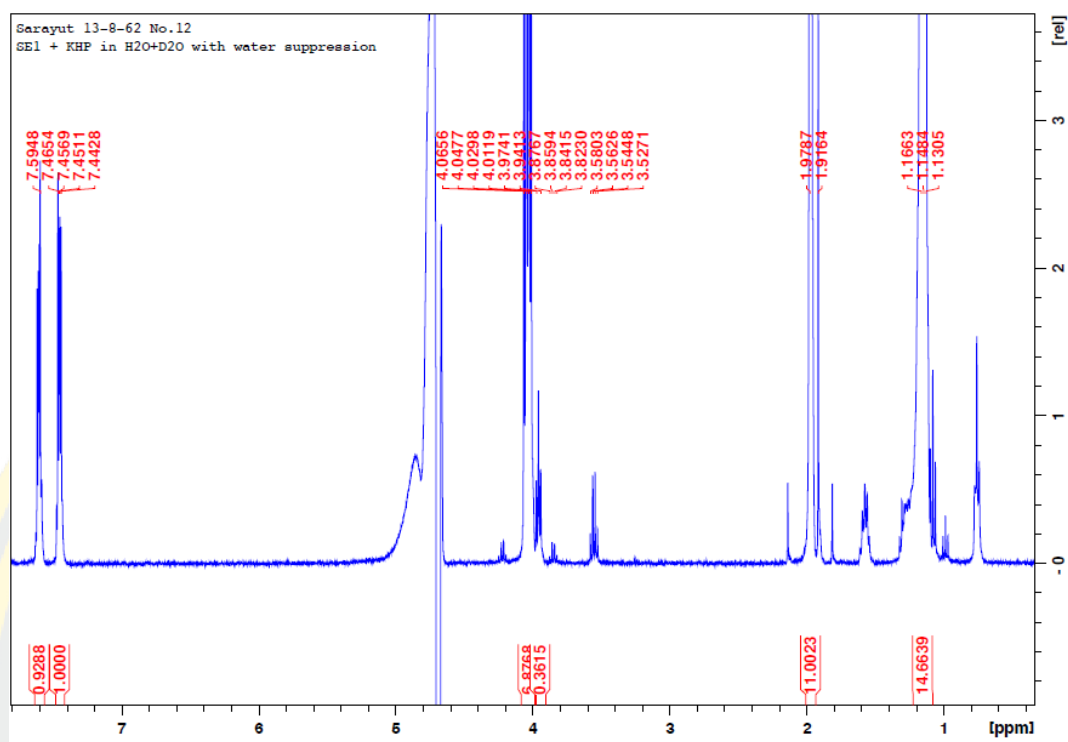


Figure A-7 The ¹H-NMR spectra of the SE1:1 sample

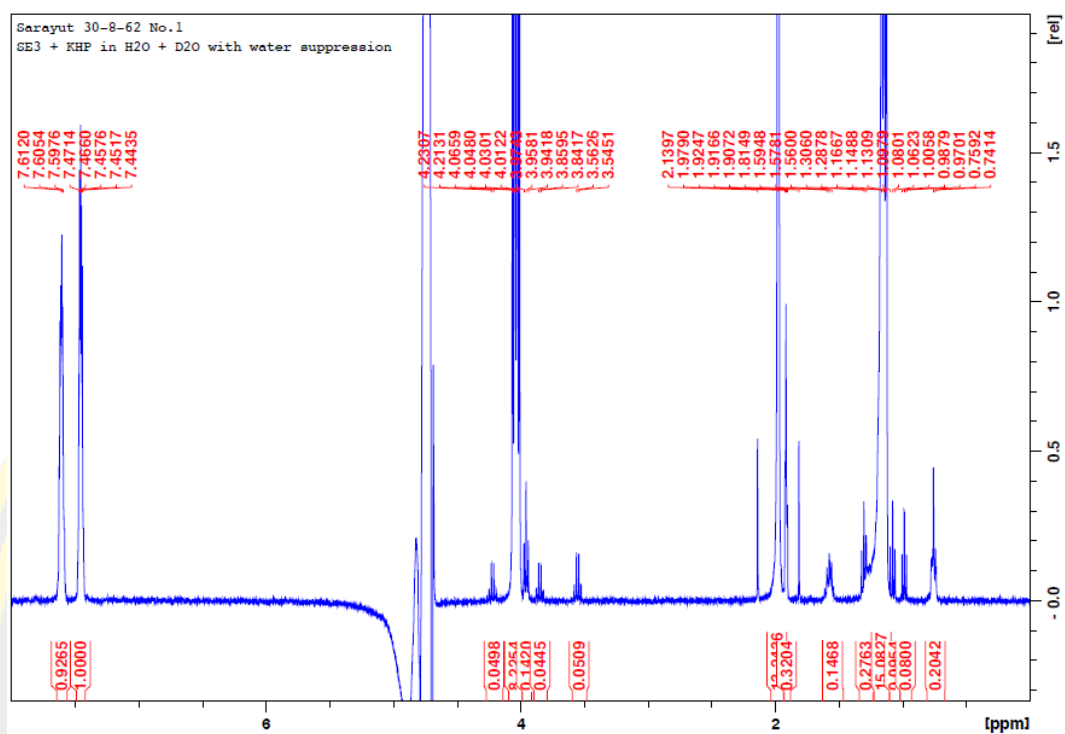


Figure A-8 The ¹H-NMR spectra of the SE1:3 sample

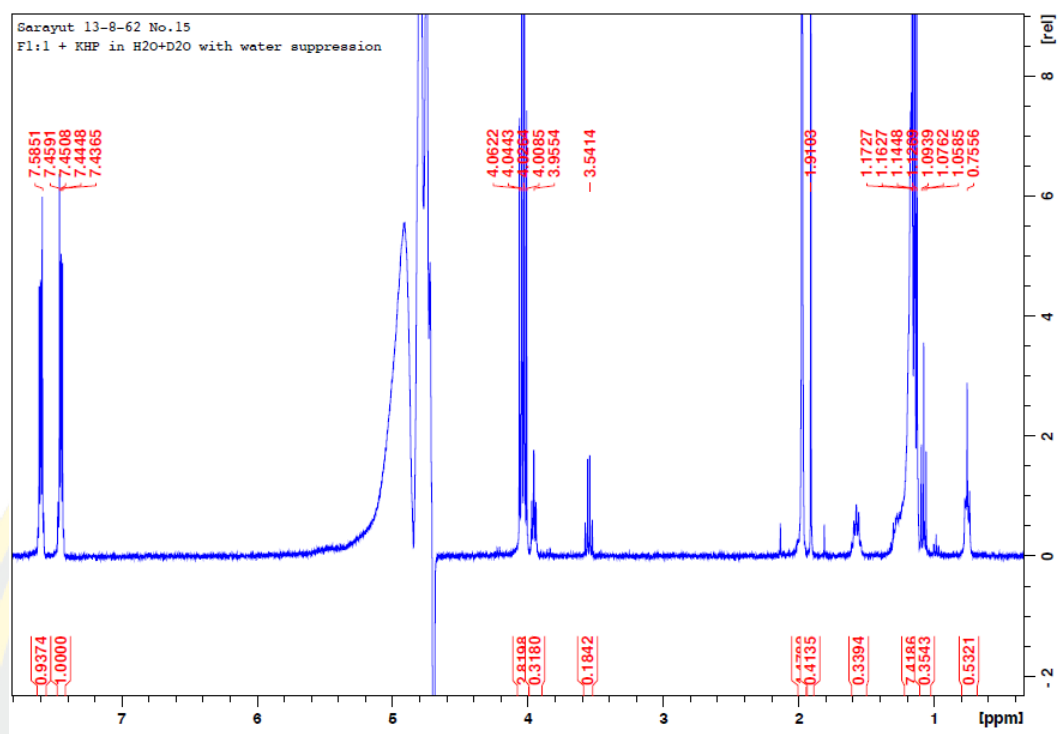


Figure A-9 The ^1H -NMR spectra of the F1:1 sample

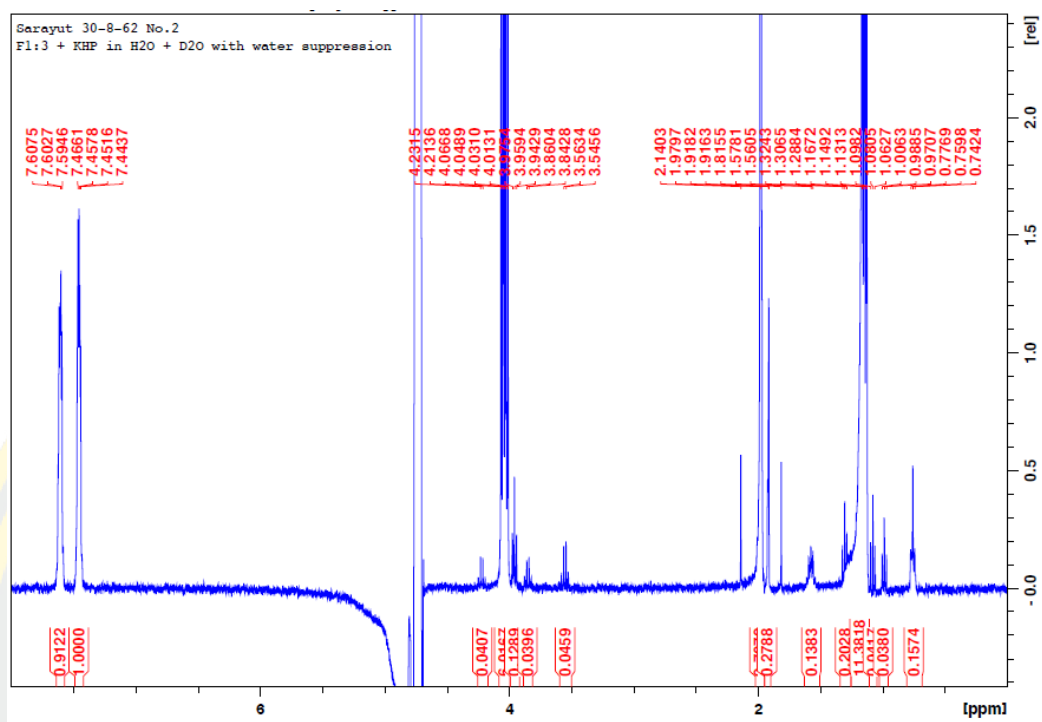


Figure A-10 The ¹H-NMR spectra of the F1:3 sample

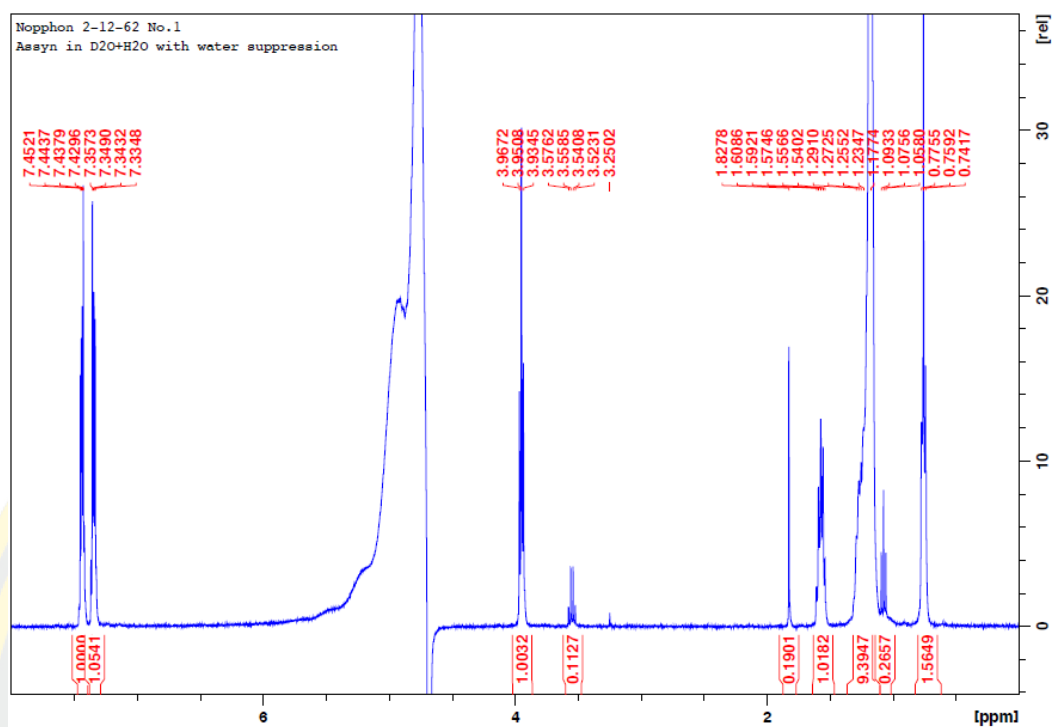


Figure A-11 The ^1H -NMR spectra of the as-syn_in flow sample

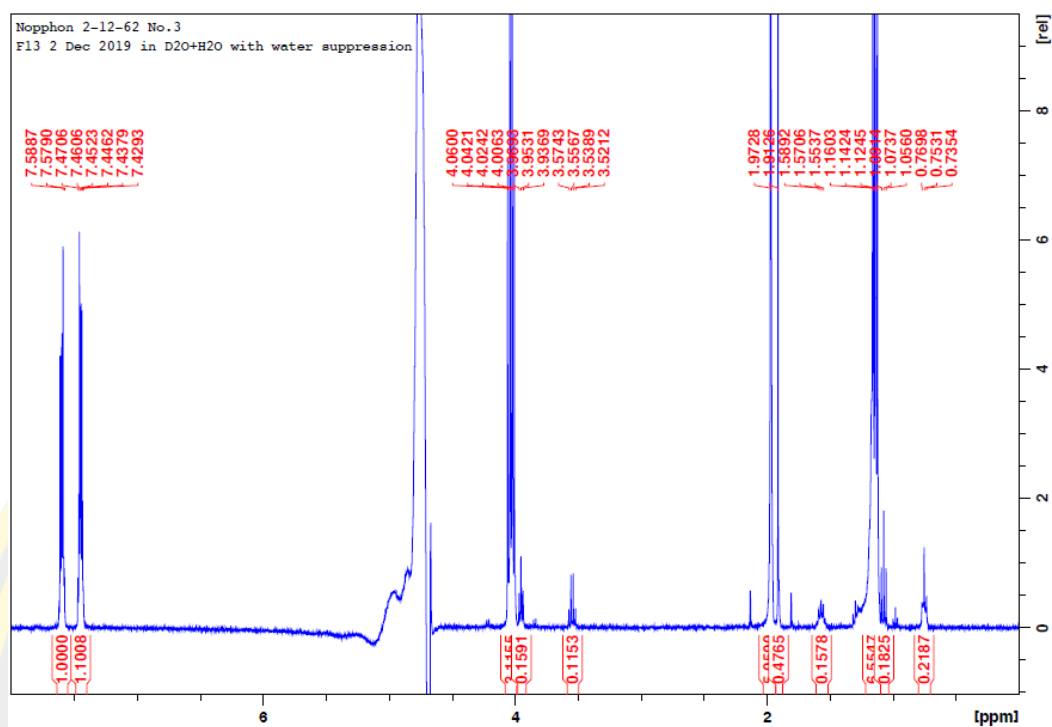


Figure A-12 The $^1\text{H-NMR}$ spectra of the F1:3_in flow sample

APPENDIX B

B1 Effect of clay on stabilizing P25 particles in solution

In order to maintain stable dispersion of P25 during the immobilization process, we added synthetic hectorite clay into the P25 solution. In the absence of clay, P25 particles precipitated almost completely after 24 h (Figure B-1). This is undesired for the immobilization process as most of the particles would precipitate the entrance zone of the tubing. When we added the clay, particles were able to maintain its colloidal state for a longer time. We found that the optimal (mass) ratio of clay to P25 was 1:1 in which the particles stayed colloidal for longer than 24 h.

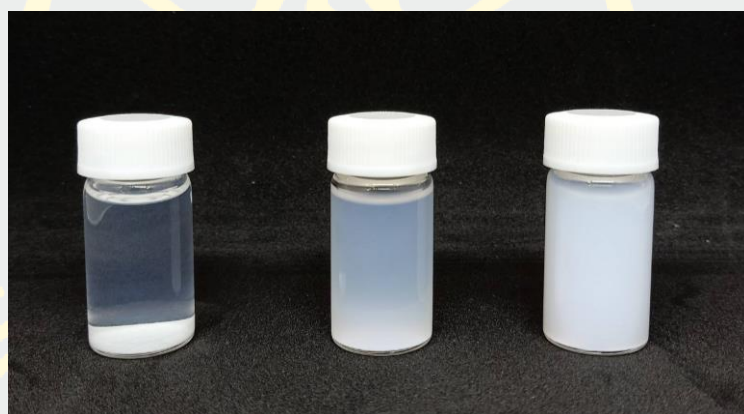


Figure B-1 The pictures of 0.1% wt P25 solution (Left) without clay, (Middle) with clay at the clay to P25 ratio of 1:4, and (Right) with clay at the clay to P25 ratio of 1:1

B2 Decolorization ratio of methylene blue at different time points: Different samples

The photocatalytic activities were studied for different samples: PEI@PDA, PEI-P25_{1L}@PDA, PEI-P25_{3L}@PDA, PEI-P25_{5L}@PDA. The residence time in the tubular reactor was set to be 10 mins. Since the calculated volume of the reactor was 1.76 mL, a flow rate of the 0.05 mM methylene blue solution into the reactor was set to be 0.176 mL/min. The samples were collected at every three residence times. Therefore, for the 10-min residence time, we collected samples at 30, 60, 90, 120, 150, 180, 210, 240, and 270 mins). Each sample was then measured with UV-Vis spectrometer. The characteristic absorbance of the methylene blue at 664 nm was noted. Figure B-2 depicts the ratio between the outlet and inlet concentrations of methylene blue at different time points over the course of the experiment for different samples.

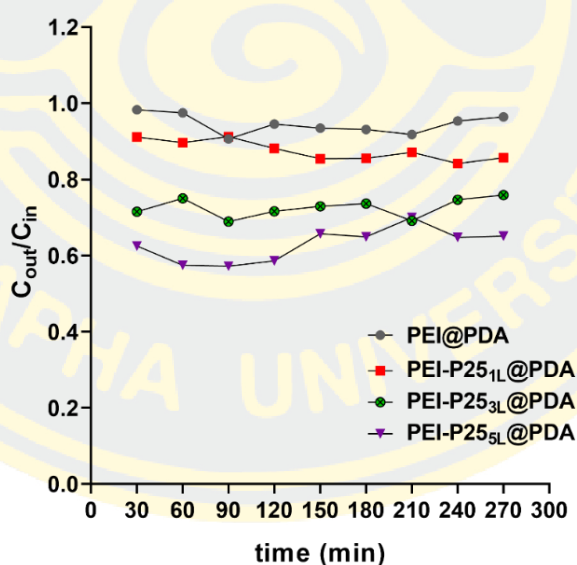


Figure B-2 C_{out}/C_{in} at different time points for different samples (Experimental conditions: $C_{in} = 0.0500$ mM, residence time = 10 mins, light intensity = 5830 mW/cm²)

B3 Decolorization ratio of methylene blue at different time points: Photolysis and adsorption tests

The photocatalytic activity of the “PEI-P25_{5L}@PDA” were studied along with other controls:

- Bare PFA with light on (light)
- PEI-P25_{5L}@PDA with light off (dark)
- PEI@PDA with light on (light)
- PDA with light on (light)

The “bare PFA with light on” experiment was to check whether the decrease in absorbance was due to the photocatalysis or photolysis. The “PEI-P25_{5L}@PDA with light off” experiment was to check whether the decrease in absorbance was due to physical adsorption of methylene blue to the immobilizing layers. The “PEI@PDA with light on” and “PDA with light on (light)” experiments were to check whether the activity was affected by PEI and PDA layers. In this experiment, the residence time in the tubular reactor was set to be 10 mins. Since the calculated volume of the reactor was 1.76 mL, a flow rate of the 0.05 mM methylene blue solution into the reactor was set to be 0.176 mL/min. The samples were collected at every three residence times. Therefore, for the 10-min residence time, we collected samples at 30, 60, 90, 120, 150, 180, 210, 240, and 270 mins). Each sample was then measured with UV-Vis spectrometer. The characteristic absorbance of the methylene blue at 664 nm was noted. The ratio between the outlet and inlet concentrations of methylene blue at different time points was shown in Figure B-3.

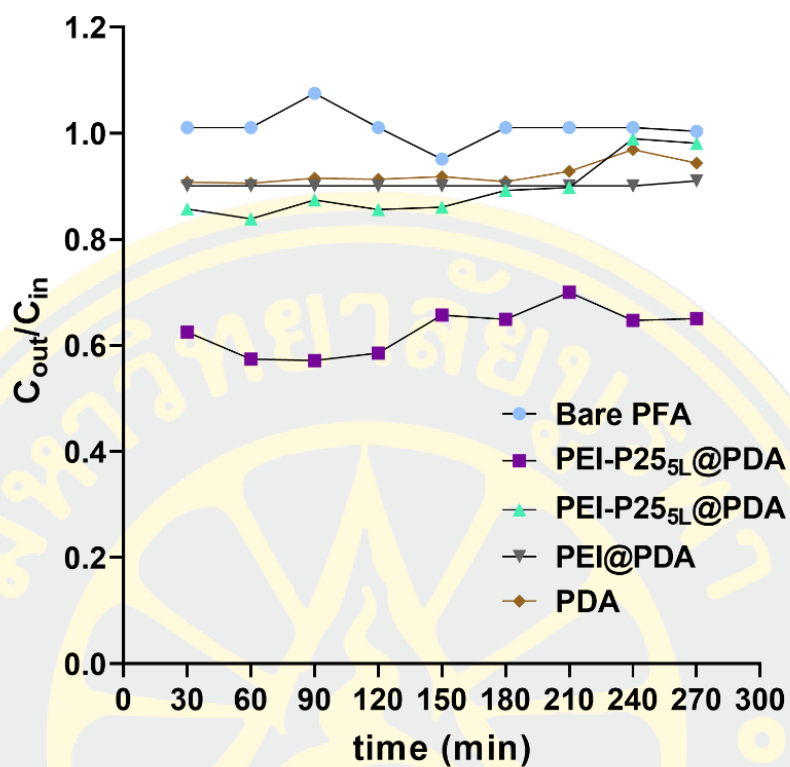


Figure B-3 C_{out}/C_{in} at different time points for different tests (Experimental conditions: $C_{in} = 0.0500$ mM, residence time = 10 mins, light intensity = 5830 mW/cm^2)

B4 Decolorization ratio of methylene blue at different time points: Different inlet concentrations

To fit the tubular modelling as formulated in the article, we have to perform the experiments at different inlet concentrations of methylene blue. Here, we varied the concentrations to be 0.00625, 0.0125, 0.0250, 0.0375, 0.0500 mM. In this experiment, the residence time in the tubular reactor was set to be 10 mins. Since the calculated volume of the reactor was 1.76 mL, a flow rate of the methylene blue solution (at particular concentration) into the reactor was set to be 0.176 mL/min. The samples were collected at every three residence times. Therefore, for the 10-min residence time, we collected samples at 30, 60, 90, 120, and 150 mins). Each sample was then measured with UV-Vis spectrometer. The characteristic absorbance of the methylene blue at 664 nm was noted. Figure B-4 represented the absorbances of methylene blue at different time points over the course of the experiment for different samples.

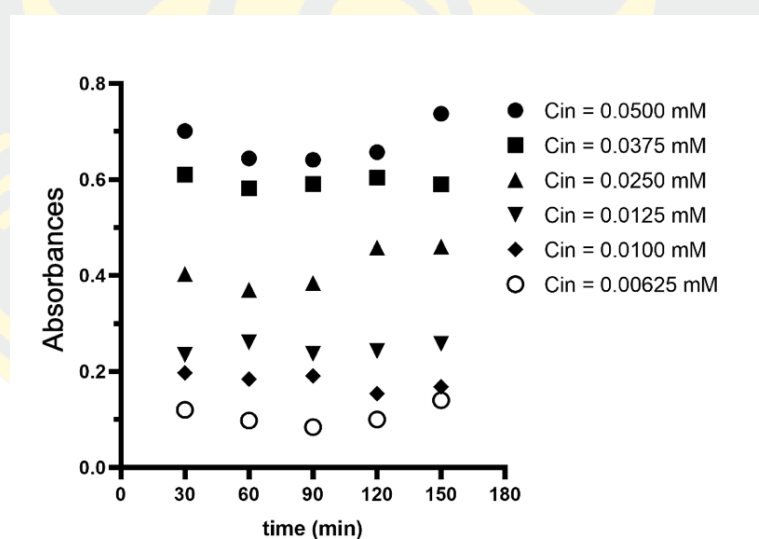


Figure B-4 Absorbances of methylene blue (at 664 nm) at different time points for different tests (Experimental conditions: residence time = 10 mins, light intensity = 5830 mW/cm²)

B5 Measurement of the light intensity at the irradiation surface

Different light intensities were varied by adjusting the electric current into the 365 nm UV-LED lamp (10 V). The electrical currents were adjusted to be 0.2, 0.4, 0.6, 0.8 and 1.0 A, corresponding to 20%, 40%, 60%, 80% and 100% power output. A portable photometer (OHSP 350P) was used to measure the light intensity. The photometer was put at the exact same location as the surface of the tubular reactor to measure the actual light intensity as incident on the reactor. The measured light intensities were shown in Figure B-5.

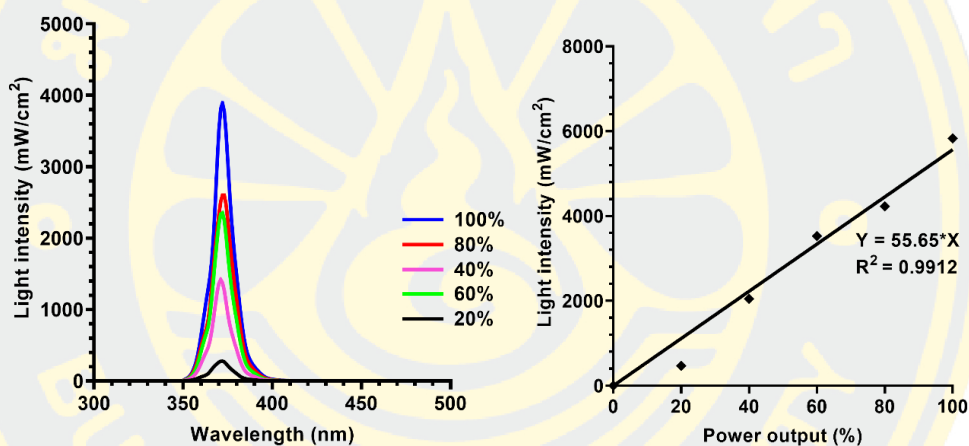


Figure B-5 Measured light intensities at different power outputs (20%, 40%, 60%, 80%, 100%)

B6 Test on repeated use of the photocatalytic flow reactor: Comparative photocatalytic activities

In this test, we have prepared a PEI-P25_{5L}@PDA sample to be used as a photocatalytic flow reactor. The “newly prepared” reactor was used continuously for more than 240 mins. The condition for the photocatalytic degradation of methylene blue was 10 mins of residence time, 10 W of light (100% of power output), and 0.0500 mM of inlet concentration of methylene blue. After that, the sample was cleaned by flowing through the sample with DI water at a flow rate of 0.01 mL/min for 30 mins. Then, the “reuse” reactor was tested with the same condition as the newly prepared one. As shown in Figure B-6, the percent decolorization of the newly prepared and reuse reactor were comparable (34.52% and 32.61%, respectively), indicating the stability of the reactor after the repeated use.

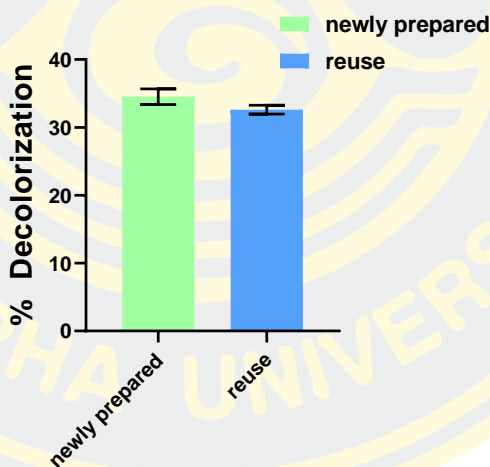
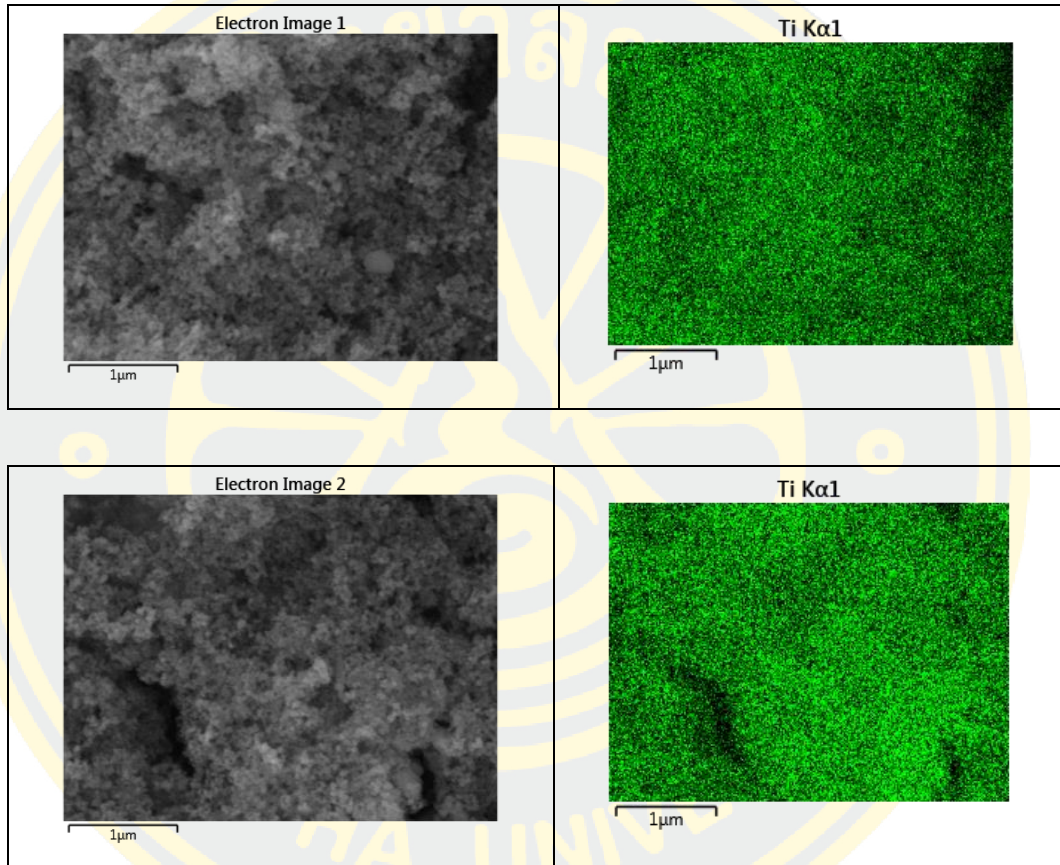


Figure B-6 Percent decolorization of the newly prepared and reuse samples shows that the photocatalytic activity was maintained after the repeated use

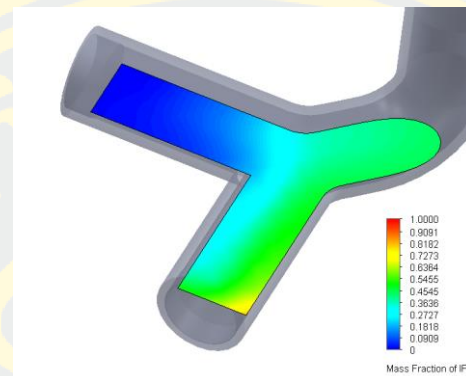
APPENDIX C

C1 EDX images of the immobilized P25 onto the glass surface at two different locations on the surface

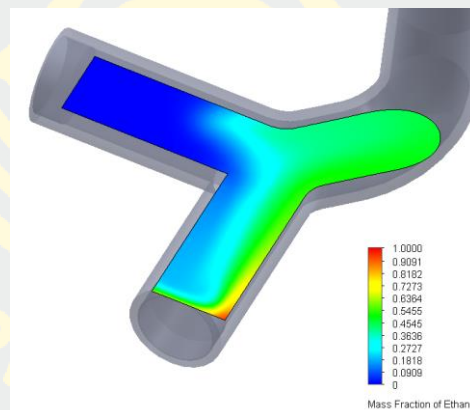


C2 Mixing performance of two inlet streams using different carrier solvents as simulated in SolidWorks

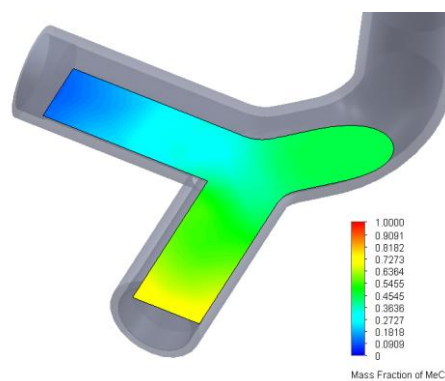
IPA as a carrier solvent



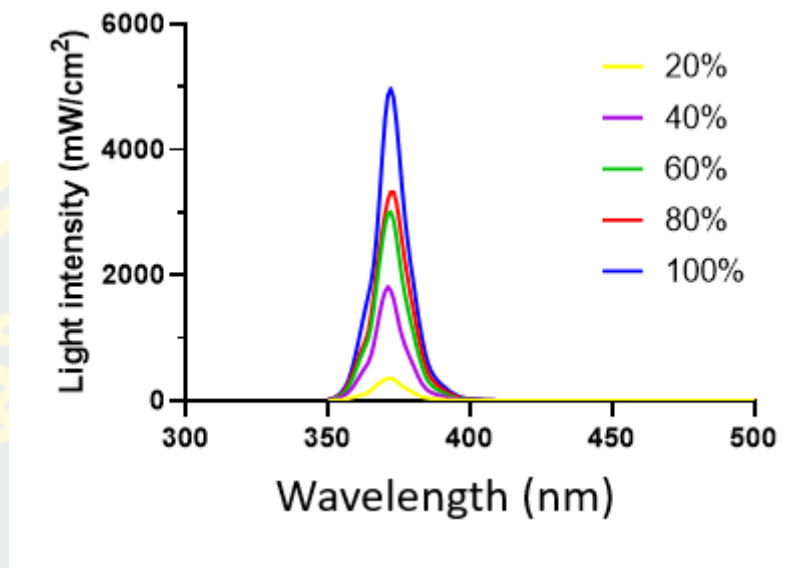
Ethanol as a carrier solvent

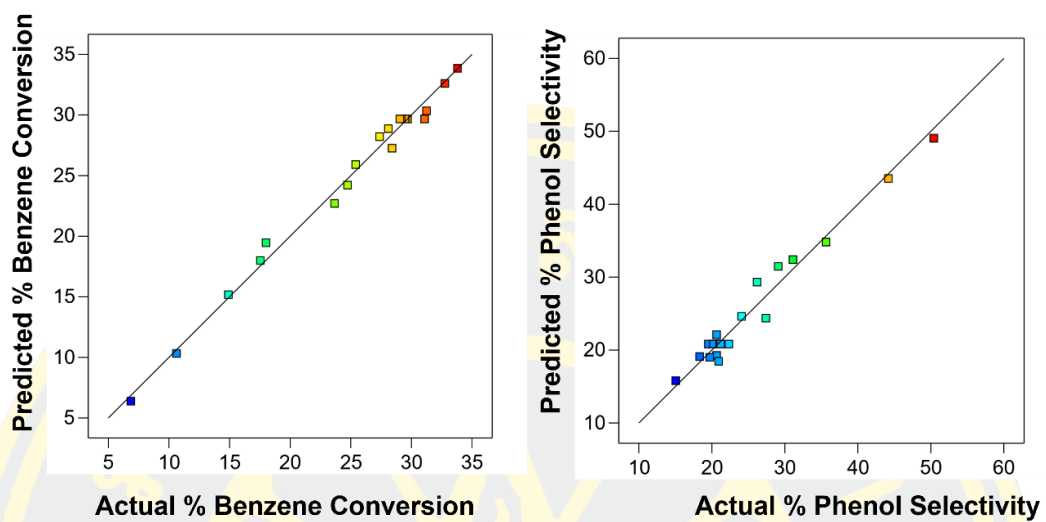


Acetonitrile as a carrier solvent



C3 Measured light intensity at the incident glass surface using different light powers



C4 Actual versus predicted values of benzene conversion and phenol selectivity

C5 Experimental conditions as generated by Design Expert using CCD model

Entry	RT(min)	Temp.(C)	% light power
1	30	30	40
2	45	45	62.5
3	60	30	85
4	45	45	62.5
5	30	30	85
6	45	19.77	62.5
7	30	60	85
8	60	30	40
9	60	60	85
10	45	45	62.5
11	45	45	62.5
12	70.23	45	62.5
13	45	45	62.5
14	45	70.23	62.5
15	30	60	40
16	45	45	24.66
17	45	45	100
18	19.77	45	62.5
19	45	45	62.5
20	60	60	40

REFERENCES



- Adamo, A., Heider, P. L., Weeranoppanant, N., & Jensen, K. F. (2013). Membrane-Based, Liquid–Liquid Separator with Integrated Pressure Control. *Industrial & Engineering Chemistry Research*, 52(31), 10802-10808. <https://doi.org/10.1021/ie401180t>
- Akiyama, R., & Kobayashi, S. (2009). “Microencapsulated” and related catalysts for organic chemistry and organic synthesis. *Chemical reviews*, 109(2), 594-642.
- Alam, A.-M., & Shon, Y.-S. (2021). Water-Soluble Noble Metal Nanoparticle Catalysts Capped with Small Organic Molecules for Organic Transformations in Water. *ACS Applied Nano Materials*, 4(4), 3294-3318. <https://doi.org/10.1021/acsnm.1c00335>
- Alele, N., Streubel, R., Gamrad, L., Barcikowski, S., & Ulbricht, M. (2016). Ultrafiltration membrane-based purification of bioconjugated gold nanoparticle dispersions. *Separation and Purification Technology*, 157, 120-130. <https://doi.org/https://doi.org/10.1016/j.seppur.2015.11.033>
- Alkilany, A. M., Abulateefeh, S. R., Mills, K. K., Bani Yaseen, A. I., Hamaly, M. A., Alkhatib, H. S., Aiedeh, K. M., & Stone, J. W. (2014). Colloidal Stability of Citrate and Mercaptoacetic Acid Capped Gold Nanoparticles upon Lyophilization: Effect of Capping Ligand Attachment and Type of Cryoprotectants. *Langmuir*, 30(46), 13799-13808. <https://doi.org/10.1021/la504000v>
- Ansar, S. M., Perera, G. S., Gomez, P., Salomon, G., Vasquez, E. S., Chu, I. W., Zou, S., Pittman, C. U., Jr., Walters, K. B., & Zhang, D. (2013). Mechanistic Study of Continuous Reactive Aromatic Organothiol Adsorption onto Silver Nanoparticles. *The Journal of Physical Chemistry C*, 117(51), 27146-27154. <https://doi.org/10.1021/jp4090102>
- Astruc, D. (2020). Introduction: Nanoparticles in Catalysis. *Chemical Reviews*, 120(2), 461-463. <https://doi.org/10.1021/acs.chemrev.8b00696>
- Augugliaro, V., Loddo, V., Marci, G., Palmisano, L., & López-Muñoz, M. a. J. (1997). Photocatalytic oxidation of cyanides in aqueous titanium dioxide suspensions. *Journal of catalysis*, 166(2), 272-283.
- Avnir, D., Braun, S., Lev, O., & Ottolenghi, M. (1994). Enzymes and other proteins entrapped in sol-gel materials. *Chemistry of Materials*, 6(10), 1605-1614.

- Awais, M., Khursheed, S., Tehreem, R., Sirajuddin, Mok, Y. S., & Siddiqui, G. U. (2022). pH regulated rapid photocatalytic degradation of methylene blue dye via niobium-nitrogen co-doped titanium dioxide nanostructures under sunlight. *Applied Catalysis A: General*, *643*, 118764. <https://doi.org/https://doi.org/10.1016/j.apcata.2022.118764>
- Azouz, A. B., Murphy, S., Karazi, S., Vázquez, M., & Brabazon, D. (2014). Fast fabrication process of microfluidic devices based on cyclic olefin copolymer. *Materials and Manufacturing Processes*, *29*(2), 93-99.
- Baek, J., Allen, P. M., Bawendi, M. G., & Jensen, K. F. (2011). Investigation of Indium Phosphide Nanocrystal Synthesis Using a High-Temperature and High-Pressure Continuous Flow Microreactor. *Angewandte Chemie International Edition*, *50*(3), 627-630. <https://doi.org/https://doi.org/10.1002/anie.201006412>
- Ball, V., Del Frari, D., Toniazzo, V., & Ruch, D. (2012). Kinetics of polydopamine film deposition as a function of pH and dopamine concentration: Insights in the polydopamine deposition mechanism. *Journal of colloid and interface science*, *386*(1), 366-372.
- Bhatkhande, D. S., Pangarkar, V. G., & Beenackers, A. A. C. M. (2002). Photocatalytic degradation for environmental applications—a review. *Journal of Chemical Technology & Biotechnology: International Research in Process, Environmental & Clean Technology*, *77*(1), 102-116.
- Bi, Y., Zhou, H., Jia, H., & Wei, P. (2017). Polydopamine-mediated preparation of an enzyme-immobilized microreactor for the rapid production of wax ester [10.1039/C7RA00499K]. *RSC Advances*, *7*(20), 12283-12291. <https://doi.org/10.1039/C7RA00499K>
- Bora, L. V., & Mewada, R. K. (2017). Visible/solar light active photocatalysts for organic effluent treatment: Fundamentals, mechanisms and parametric review. *Renewable and Sustainable Energy Reviews*, *76*, 1393-1421.
- Bosc, F., Ayrál, A., & Guizard, C. (2005). Mesoporous anatase coatings for coupling membrane separation and photocatalyzed reactions. *Journal of Membrane Science*, *265*(1), 13-19. <https://doi.org/https://doi.org/10.1016/j.memsci.2005.04.039>

- Brühwiler, D. (2010). Postsynthetic functionalization of mesoporous silica. *Nanoscale*, 2(6), 887-892.
- Buglioni, L., Raymenants, F., Slattery, A., Zondag, S. D. A., & Noël, T. (2022). Technological Innovations in Photochemistry for Organic Synthesis: Flow Chemistry, High-Throughput Experimentation, Scale-up, and Photoelectrochemistry. *Chemical Reviews*, 122(2), 2752-2906. <https://doi.org/10.1021/acs.chemrev.1c00332>
- Bui, T. D., Kimura, A., Higashida, S., Ikeda, S., & Matsumura, M. (2011). Two routes for mineralizing benzene by TiO₂-photocatalyzed reaction. *Applied Catalysis B: Environmental*, 107(1), 119-127. <https://doi.org/https://doi.org/10.1016/j.apcatb.2011.07.004>
- Burda, C., Chen, X., Narayanan, R., & El-Sayed, M. A. (2005). Chemistry and Properties of Nanocrystals of Different Shapes. *Chemical Reviews*, 105(4), 1025-1102. <https://doi.org/10.1021/cr030063a>
- Cambié, D., Bottecchia, C., Straathof, N. J. W., Hessel, V., & Noël, T. (2016). Applications of Continuous-Flow Photochemistry in Organic Synthesis, Material Science, and Water Treatment. *Chemical Reviews*, 116(17), 10276-10341. <https://doi.org/10.1021/acs.chemrev.5b00707>
- Cargnello, M., Chen, C., Diroll, B. T., Doan-Nguyen, V. V. T., Gorte, R. J., & Murray, C. B. (2015). Efficient Removal of Organic Ligands from Supported Nanocrystals by Fast Thermal Annealing Enables Catalytic Studies on Well-Defined Active Phases. *Journal of the American Chemical Society*, 137(21), 6906-6911. <https://doi.org/10.1021/jacs.5b03333>
- Carneiro, J. T., Berger, R., Moulijn, J. A., & Mul, G. (2009). An internally illuminated monolith reactor: Pros and cons relative to a slurry reactor. *Catalysis Today*, 147, S324-S329. <https://doi.org/https://doi.org/10.1016/j.cattod.2009.07.041>
- Chandrakala, V., Aruna, V., & Angajala, G. (2022). Review on metal nanoparticles as nanocarriers: current challenges and perspectives in drug delivery systems. *Emergent Materials*, 5(6), 1593-1615. <https://doi.org/10.1007/s42247-021-00335-x>
- Chaudhuri, A., Zondag, S. D., Schuurmans, J. H., van der Schaaf, J., & Noël, T. (2022). Scale-up of a heterogeneous photocatalytic degradation using a photochemical

- rotor–stator spinning disk reactor. *Organic Process Research & Development*, 26(4), 1279-1288.
- Cheng, D., He, M., Ran, J., Cai, G., Wu, J., & Wang, X. (2018). In situ reduction of TiO₂ nanoparticles on cotton fabrics through polydopamine templates for photocatalysis and UV protection. *Cellulose*, 25(2), 1413-1424.
- Chong, M. N., Jin, B., Chow, C. W. K., & Saint, C. (2010). Recent developments in photocatalytic water treatment technology: A review. *Water Research*, 44(10), 2997-3027. <https://doi.org/10.1016/j.watres.2010.02.039>
- Claes, T., Dilissen, A., Leblebici, M. E., & Van Gerven, T. (2019). Translucent packed bed structures for high throughput photocatalytic reactors. *Chemical Engineering Journal*, 361, 725-735. <https://doi.org/10.1016/j.cej.2018.12.107>
- Claes, T., Gerven, T. V., & Leblebici, M. E. (2021). Design considerations for photocatalytic structured packed bed reactors. *Chemical Engineering Journal*, 403, 126355. <https://doi.org/10.1016/j.cej.2020.126355>
- Claes, T., Van Gerven, T., & Leblebici, M. E. (2021). Design considerations for photocatalytic structured packed bed reactors. *Chemical Engineering Journal*, 403, 126355.
- Colmenares, J. C., Nair, V., Kuna, E., & Łomot, D. (2018). Development of photocatalyst coated fluoropolymer based microreactor using ultrasound for water remediation. *Ultrasonics Sonochemistry*, 41, 297-302. <https://doi.org/10.1016/j.ultsonch.2017.09.053>
- Constantinou, M., Hadjigeorgiou, K., Abalde-Cela, S., & Andreou, C. (2022). Label-Free Sensing with Metal Nanostructure-Based Surface-Enhanced Raman Spectroscopy for Cancer Diagnosis. *ACS Applied Nano Materials*, 5(9), 12276-12299. <https://doi.org/10.1021/acsnm.2c02392>
- Cushing, B. L., Kolesnichenko, V. L., & O'Connor, C. J. (2004). Recent Advances in the Liquid-Phase Syntheses of Inorganic Nanoparticles. *Chemical Reviews*, 104(9), 3893-3946. <https://doi.org/10.1021/cr030027b>
- Daghrir, R., Drogui, P., & Robert, D. (2013). Modified TiO₂ For Environmental Photocatalytic Applications: A Review. *Industrial & Engineering Chemistry Research*, 52(10), 3581-3599. <https://doi.org/10.1021/ie303468t>

- de Sá, D. S., Vasconcellos, L. E., de Souza, J. R., Marinkovic, B. A., Del Rosso, T., Fulvio, D., Maza, D., Massi, A., & Pandoli, O. (2018). Intensification of photocatalytic degradation of organic dyes and phenol by scale-up and numbering-up of meso- and microfluidic TiO₂ reactors for wastewater treatment. *Journal of Photochemistry and Photobiology A: Chemistry*, *364*, 59-75. <https://doi.org/https://doi.org/10.1016/j.jphotochem.2018.05.020>
- Deen, W. M. (1998). Analysis of transport phenomena. (*No Title*).
- Deepracha, S., Bureekaew, S., & Ogawa, M. (2019). Synergy effects of the complexation of a titania and a smectite on the film formation and its photocatalyst' performance. *Applied Clay Science*, *169*, 129-134. <https://doi.org/https://doi.org/10.1016/j.clay.2018.12.005>
- Devaraji, P., Sathu, N. K., & Gopinath, C. S. (2014). Ambient oxidation of benzene to phenol by photocatalysis on Au/TiO₂. 98V0. 02O2: role of holes. *Acs Catalysis*, *4*(9), 2844-2853.
- Dionysiou, D. D., Balasubramanian, G., Suidan, M. T., Khodadoust, A. P., Baudin, I., & Laine, J.-M. (2000). Rotating disk photocatalytic reactor: development, characterization, and evaluation for the destruction of organic pollutants in water. *Water Research*, *34*(11), 2927-2940.
- Dionysiou, D. D., Suidan, M. T., Baudin, I., & Laine, J.-M. (2002). Oxidation of organic contaminants in a rotating disk photocatalytic reactor: reaction kinetics in the liquid phase and the role of mass transfer based on the dimensionless Damköhler number. *Applied Catalysis B: Environmental*, *38*(1), 1-16.
- Ebnesajjad, S. (2015). *Fluoroplastics, Volume 2: Melt Processible Fluoropolymers-The Definitive User's Guide and Data Book*. William Andrew.
- Emmanuel, N., Emonds-Alt, G., Lismont, M., Eppe, G., & Monbaliu, J.-C. M. (2017). Exploring the Fundamentals of Microreactor Technology with Multidisciplinary Lab Experiments Combining the Synthesis and Characterization of Inorganic Nanoparticles. *Journal of Chemical Education*, *94*(6), 775-780. <https://doi.org/10.1021/acs.jchemed.6b00899>
- Eskandarloo, H., Badii, A., Behnajady, M. A., & Ziarani, G. M. (2015). UV-LEDs assisted preparation of silver deposited TiO₂ catalyst bed inside microchannels

- as a high efficiency microphotoreactor for cleaning polluted water. *Chemical Engineering Journal*, 270, 158-167.
- Fox, M. A., & Dulay, M. T. (1993). Heterogeneous photocatalysis. *Chemical reviews*, 93(1), 341-357.
- Giusi, D., Ampelli, C., Genovese, C., Perathoner, S., & Centi, G. (2021). A novel gas flow-through photocatalytic reactor based on copper-functionalized nanomembranes for the photoreduction of CO₂ to C1-C2 carboxylic acids and C1-C3 alcohols. *Chemical Engineering Journal*, 408, 127250. <https://doi.org/https://doi.org/10.1016/j.cej.2020.127250>
- Gomathi Devi, L., Narasimha Murthy, B., & Girish Kumar, S. (2009). Heterogeneous photo catalytic degradation of anionic and cationic dyes over TiO₂ and TiO₂ doped with Mo⁶⁺ ions under solar light: Correlation of dye structure and its adsorptive tendency on the degradation rate. *Chemosphere*, 76(8), 1163-1166. <https://doi.org/https://doi.org/10.1016/j.chemosphere.2009.04.005>
- Gondoni, P., Ghidelli, M., Di Fonzo, F., Li Bassi, A., & Casari, C. S. (2013). Fabrication of nano-engineered transparent conducting oxides by pulsed laser deposition. *J Vis Exp*(72), e50297. <https://doi.org/10.3791/50297>
- Gora, A., Toepfer, B., Puddu, V., & Li Puma, G. (2006). Photocatalytic oxidation of herbicides in single-component and multicomponent systems: Reaction kinetics analysis. *Applied Catalysis B: Environmental*, 65(1), 1-10. <https://doi.org/https://doi.org/10.1016/j.apcatb.2005.12.009>
- Gorges, R., Meyer, S., & Kreisel, G. (2004). Photocatalysis in microreactors. *Journal of Photochemistry and Photobiology A: Chemistry*, 167(2-3), 95-99.
- Goto, T., & Ogawa, M. (2015). Visible-light-responsive photocatalytic flow reactor composed of titania film photosensitized by metal complex-clay hybrid. *ACS Applied Materials & Interfaces*, 7(23), 12631-12634.
- Goto, T., & Ogawa, M. (2016). Efficient photocatalytic oxidation of benzene to phenol by metal complex-clay/TiO₂ hybrid photocatalyst. *RSC advances*, 6(28), 23794-23797.
- Gracias, D. H., Tien, J., Breen, T. L., Hsu, C., & Whitesides, G. M. (2000). Forming Electrical Networks in Three Dimensions by Self-Assembly. *Science*, 289(5482), 1170-1172. <https://doi.org/doi:10.1126/science.289.5482.1170>

- Guild, C., Biswas, S., Meng, Y., Jafari, T., Gaffney, A. M., & Suib, S. L. (2014). Perspectives of spray pyrolysis for facile synthesis of catalysts and thin films: An introduction and summary of recent directions. *Catalysis Today*, 238, 87-94. <https://doi.org/10.1016/j.cattod.2014.03.056>
- Han, W., Xiang, W., Meng, Z., Dong, S., & Lv, Y. (2023). A novel Cr-doped CdS/ZnO nanocomposite for efficient photocatalytic hydroxylation of benzene to phenol. *Colloids and Surfaces A: Physicochemical and Engineering Aspects*, 670, 131529.
- Han, W., Xiang, W., Shi, J., & Ji, Y. (2022). Recent advances in the heterogeneous photocatalytic hydroxylation of benzene to phenol. *Molecules*, 27(17), 5457.
- Haseneder, R. (2014). Encyclopedia of Membrane Science and Technology, Vol. 1–3. Von EMV Hoek, VV Tarabara. *Chemie Ingenieur Technik*, 86(11), 1986-1987.
- Hassinen, A., Moreels, I., De Nolf, K., Smet, P. F., Martins, J. C., & Hens, Z. (2012). Short-Chain Alcohols Strip X-Type Ligands and Quench the Luminescence of PbSe and CdSe Quantum Dots, Acetonitrile Does Not. *Journal of the American Chemical Society*, 134(51), 20705-20712. <https://doi.org/10.1021/ja308861d>
- Hench, L. L., & West, J. K. (1990). The sol-gel process. *Chemical Reviews*, 90(1), 33-72. <https://doi.org/10.1021/cr00099a003>
- Hervés, P., Pérez-Lorenzo, M., Liz-Marzán, L. M., Dzubiella, J., Lu, Y., & Ballauff, M. (2012). Catalysis by metallic nanoparticles in aqueous solution: model reactions [10.1039/C2CS35029G]. *Chemical Society Reviews*, 41(17), 5577-5587. <https://doi.org/10.1039/C2CS35029G>
- Higashimoto, S., Kurikawa, Y., Tanabe, Y., Fukushima, T., Harada, A., Murata, M., Sakata, Y., & Kobayashi, H. (2023). Photocatalytic property of WO₃ modified with noble metal co-catalysts towards selective hydroxylation of benzene to phenol under visible light irradiation. *Applied Catalysis B: Environmental*, 325, 122289.
- Hirano, K., & Asami, M. (2013). Phenolic resins—100years of progress and their future. *Reactive and Functional Polymers*, 73(2), 256-269. <https://doi.org/10.1016/j.reactfunctpolym.2012.07.003>

- Hoffmann, N. (2015). Photocatalysis with TiO₂ Applied to Organic Synthesis. *Australian Journal of Chemistry*, 68(11), 1621-1639. <https://doi.org/10.1071/CH15322>
- Hollamby, M. J., Eastoe, J., Chemelli, A., Glatter, O., Rogers, S., Heenan, R. K., & Grillo, I. (2010). Separation and Purification of Nanoparticles in a Single Step. *Langmuir*, 26(10), 6989-6994. <https://doi.org/10.1021/la904225k>
- Hook, B. D., Dohle, W., Hirst, P. R., Pickworth, M., Berry, M. B., & Booker-Milburn, K. I. (2005). A practical flow reactor for continuous organic photochemistry. *The Journal of organic chemistry*, 70(19), 7558-7564.
- Hühn, J., Carrillo-Carrion, C., Soliman, M. G., Pfeiffer, C., Valdeperez, D., Masood, A., Chakraborty, I., Zhu, L., Gallego, M., Yue, Z., Carril, M., Feliu, N., Escudero, A., Alkilany, A. M., Pelaz, B., del Pino, P., & Parak, W. J. (2017). Selected Standard Protocols for the Synthesis, Phase Transfer, and Characterization of Inorganic Colloidal Nanoparticles. *Chemistry of Materials*, 29(1), 399-461. <https://doi.org/10.1021/acs.chemmater.6b04738>
- Ide, Y., Matsuoka, M., & Ogawa, M. (2010). Efficient visible-light-induced photocatalytic activity on gold-nanoparticle-supported layered titanate. *Journal of the American Chemical Society*, 132(47), 16762-16764.
- Ide, Y., Matsuoka, M., & Ogawa, M. (2012). Controlled photocatalytic oxidation of benzene in aqueous clay suspension. *ChemCatChem*, 4(5), 628-630.
- Ide, Y., Nakamura, N., Hattori, H., Ogino, R., Ogawa, M., Sadakane, M., & Sano, T. (2011). Sunlight-induced efficient and selective photocatalytic benzene oxidation on TiO₂-supported gold nanoparticles under CO₂ atmosphere [10.1039/C1CC14662A]. *Chemical Communications*, 47(41), 11531-11533. <https://doi.org/10.1039/C1CC14662A>
- Jamkhande, P. G., Ghule, N. W., Bamer, A. H., & Kalaskar, M. G. (2019). Metal nanoparticles synthesis: An overview on methods of preparation, advantages and disadvantages, and applications. *Journal of Drug Delivery Science and Technology*, 53, 101174. <https://doi.org/10.1016/j.jddst.2019.101174>
- Jensen, H., Soloviev, A., Li, Z., & Søgaaard, E. G. (2005). XPS and FTIR investigation of the surface properties of different prepared titania nano-powders. *Applied*

- Surface Science*, 246(1), 239-249.
<https://doi.org/https://doi.org/10.1016/j.apsusc.2004.11.015>
- Jiang, J., Zhu, L., Zhu, L., Zhu, B., & Xu, Y. (2011). Surface characteristics of a self-polymerized dopamine coating deposited on hydrophobic polymer films. *Langmuir*, 27(23), 14180-14187.
- Jin, F.-L., Zhao, M., Park, M., & Park, S.-J. (2019). Recent Trends of Foaming in Polymer Processing: A Review. *Polymers*, 11(6), 953.
<https://www.mdpi.com/2073-4360/11/6/953>
- Jo, W.-K., & Tayade, R. J. (2014). New Generation Energy-Efficient Light Source for Photocatalysis: LEDs for Environmental Applications. *Industrial & Engineering Chemistry Research*, 53(6), 2073-2084.
<https://doi.org/10.1021/ie404176g>
- Jolliffe, H. G., & Gerogiorgis, D. I. (2015). Process modelling and simulation for continuous pharmaceutical manufacturing of ibuprofen. *Chemical Engineering Research and Design*, 97, 175-191.
- Jossen, R. (2006). *Controlled synthesis of mixed oxide nanoparticles by flame spray pyrolysis* [ETH Zurich].
- Jung, D. S., Park, S. B., & Kang, Y. C. (2010). Design of particles by spray pyrolysis and recent progress in its application. *Korean Journal of Chemical Engineering*, 27(6), 1621-1645. <https://doi.org/10.1007/s11814-010-0402-5>
- Kayahan, E., Jacobs, M., Braeken, L., Thomassen, L. C., Kuhn, S., van Gerven, T., & Leblebici, M. E. (2020). Dawn of a new era in industrial photochemistry: the scale-up of micro-and mesostructured photoreactors. *Beilstein journal of organic chemistry*, 16(1), 2484-2504.
- Khositanon, C., Adpakpang, K., Bureekaew, S., & Weeranoppanant, N. (2020). Continuous-flow purification of silver nanoparticles and its integration with flow synthesis. *Journal of Flow Chemistry*, 10(1), 353-362.
<https://doi.org/10.1007/s41981-020-00084-8>
- Khositanon, C., Deepracha, S., Assabumrungrat, S., Ogawa, M., & Weeranoppanant, N. (2022). Simple Fabrication of a Continuous-Flow Photocatalytic Reactor Using Dopamine-Assisted Immobilization onto a Fluoropolymer Tubing.

- Industrial & Engineering Chemistry Research*, 61(3), 1322-1331.
<https://doi.org/10.1021/acs.iecr.1c04303>
- Kirimura, K., Gunji, H., Wakayama, R., Hattori, T., & Ishii, Y. (2010). Enzymatic Kolbe–Schmitt reaction to form salicylic acid from phenol: Enzymatic characterization and gene identification of a novel enzyme, *Trichosporon moniliiforme* salicylic acid decarboxylase. *Biochemical and Biophysical Research Communications*, 394(2), 279-284.
<https://doi.org/10.1016/j.bbrc.2010.02.154>
- Knop, A., Bohmer, V., & Pilato, L. (1989). Phenol–Formaldehyde Polymers. *Pergamon Press plc, Comprehensive Polymer Science.*, 5, 611-647.
- Kralj, J. G., Sahoo, H. R., & Jensen, K. F. (2007). Integrated continuous microfluidic liquid–liquid extraction. *Lab on a Chip*, 7(2), 256-263.
- Kucuk, I., & Edirisinghe, M. (2014). Microfluidic preparation of polymer nanospheres. *Journal of nanoparticle research*, 16(12), 2626.
- Kumar, K., & Chowdhury, A. (2018). Use of novel nanostructured photocatalysts for the environmental sustainability of wastewater treatments.
- Kundu, S., & Patra, A. (2017). Nanoscale Strategies for Light Harvesting. *Chemical Reviews*, 117(2), 712-757. <https://doi.org/10.1021/acs.chemrev.6b00036>
- Leblebici, M. E., Stefanidis, G. D., & Van Gerven, T. (2015). Comparison of photocatalytic space-time yields of 12 reactor designs for wastewater treatment. *Chemical Engineering and Processing: Process Intensification*, 97, 106-111.
<https://doi.org/10.1016/j.cep.2015.09.009>
- Lee, H., Dellatore, S. M., Miller, W. M., & Messersmith, P. B. (2007). Mussel-inspired surface chemistry for multifunctional coatings. *science*, 318(5849), 426-430.
- Lei, L., Wang, N., Zhang, X., Tai, Q., Tsai, D. P., & Chan, H. L. (2010). Optofluidic planar reactors for photocatalytic water treatment using solar energy. *Biomicrofluidics*, 4(4), 043004.
- Lemmon, E. W. (2010). Thermophysical properties of fluid systems. *NIST chemistry WebBook*.
- Li, J., Xu, Y., Ding, Z., Mahadi, A. H., Zhao, Y., & Song, Y.-F. (2020). Photocatalytic selective oxidation of benzene to phenol in water over layered double

- hydroxide: A thermodynamic and kinetic perspective. *Chemical Engineering Journal*, 388, 124248. <https://doi.org/https://doi.org/10.1016/j.cej.2020.124248>
- Li, J., Yuan, S., Zhu, J., & Van der Bruggen, B. (2019). High-flux, antibacterial composite membranes via polydopamine-assisted PEI-TiO₂/Ag modification for dye removal. *Chemical Engineering Journal*, 373, 275-284. <https://doi.org/https://doi.org/10.1016/j.cej.2019.05.048>
- Liebscher, J. r., Mrówczyński, R., Scheidt, H. A., Filip, C., Hädade, N. D., Turcu, R., Bende, A., & Beck, S. (2013). Structure of polydopamine: a never-ending story? *Langmuir*, 29(33), 10539-10548.
- Lin, C., Liu, M., & Yang, Z. (2016). Performance of a Metal Ion-Doped Titania-Coated Planar Photocatalytic Microreactor. *Chemical Engineering & Technology*, 39(1), 88-96.
- Lin, H., & Valsaraj, K. T. (2005). Development of an optical fiber monolith reactor for photocatalytic wastewater treatment. *Journal of Applied Electrochemistry*, 35(7-8), 699-708.
- Lin, X. Z., Terepka, A. D., & Yang, H. (2004). Synthesis of Silver Nanoparticles in a Continuous Flow Tubular Microreactor. *Nano Letters*, 4(11), 2227-2232. <https://doi.org/10.1021/nl0485859>
- Liu, G., Xiang, J., Xia, Q., Li, K., Yan, H., & Yu, L. (2020). Fabrication of Durably Antibacterial Cotton Fabrics by Robust and Uniform Immobilization of Silver Nanoparticles via Mussel-Inspired Polydopamine/Polyethyleneimine Coating. *Industrial & Engineering Chemistry Research*, 59(20), 9666-9678. <https://doi.org/10.1021/acs.iecr.9b07076>
- Livage, J., Henry, M., & Sanchez, C. (1988). Sol-gel chemistry of transition metal oxides. *Progress in Solid State Chemistry*, 18(4), 259-341. [https://doi.org/https://doi.org/10.1016/0079-6786\(88\)90005-2](https://doi.org/https://doi.org/10.1016/0079-6786(88)90005-2)
- Lopez-Lopez, C., Purswani, J., Martín-Pascual, J., Martínez-Toledo, M., Muñoz, M., & Poyatos, J. (2015). Toxic effect of H₂O₂ in H₂O₂/UV, photo-Fenton and heterogeneous photocatalysis (TiO₂/H₂O₂/UV) systems to treat textile wastewater. *Desalination and Water Treatment*, 56(11), 3044-3053.
- Lu, H., Schmidt, M. A., & Jensen, K. F. (2001). Photochemical reactions and on-line UV detection in microfabricated reactors. *Lab on a Chip*, 1(1), 22-28.

- Luo, L., Huang, W., Zhang, J., Yu, Y., & Sun, T. (2024). Metal-Based Nanoparticles as Antimicrobial Agents: A Review. *ACS Applied Nano Materials*, 7(3), 2529-2545. <https://doi.org/10.1021/acsnm.3c05615>
- Macwan, D. P., Dave, P. N., & Chaturvedi, S. (2011). A review on nano-TiO₂ sol-gel type syntheses and its applications. *Journal of Materials Science*, 46(11), 3669-3686. <https://doi.org/10.1007/s10853-011-5378-y>
- Mädler, L., Kammler, H. K., Mueller, R., & Pratsinis, S. (2002). Controlled synthesis of nanostructured particles by flame spray pyrolysis. *Journal of Aerosol Science*, 33, 369-389. [https://doi.org/10.1016/S0021-8502\(01\)00159-8](https://doi.org/10.1016/S0021-8502(01)00159-8)
- Maeda, K., & Domen, K. (2010). Photocatalytic Water Splitting: Recent Progress and Future Challenges. *The Journal of Physical Chemistry Letters*, 1(18), 2655-2661. <https://doi.org/10.1021/jz1007966>
- Maric, R., Fukui, T., Ohara, S., Yoshida, H., Nishimura, M., Inagaki, T., & Miura, K. (2000). Powder prepared by spray pyrolysis as an electrode material for solid oxide fuel cells. *Journal of Materials Science*, 35(6), 1397-1404. <https://doi.org/10.1023/A:1004754729231>
- Martini, P., Adamo, A., Syna, N., Boschi, A., Uccelli, L., Weeranoppanant, N., Markham, J., & Pascali, G. (2019). Perspectives on the use of liquid extraction for radioisotope purification. *Molecules*, 24(2), 334.
- McMorn, P., & Hutchings, G. J. (2004). Heterogeneous enantioselective catalysts: strategies for the immobilisation of homogeneous catalysts. *Chemical Society Reviews*, 33(2), 108-122.
- Meng, Y., Xia, S., Pan, G., Xue, J., Jiang, J., & Ni, Z. (2017). Preparation and photocatalytic activity of composite metal oxides derived from Salen-Cu (II) intercalated layered double hydroxides. *Korean Journal of Chemical Engineering*, 34, 2331-2341.
- Mikaeili, F., Topcu, S., Jodhani, G., & Gouma, P.-I. (2018). Flame-sprayed pure and Ce-doped TiO₂ photocatalysts. *Catalysts*, 8(9), 342.
- Morris-Cohen, A. J., Donakowski, M. D., Knowles, K. E., & Weiss, E. A. (2010). The Effect of a Common Purification Procedure on the Chemical Composition of the Surfaces of CdSe Quantum Dots Synthesized with Trioctylphosphine Oxide.

- The Journal of Physical Chemistry C*, 114(2), 897-906.
<https://doi.org/10.1021/jp909492w>
- Mueller, R., Mädler, L., & Pratsinis, S. E. (2003). Nanoparticle synthesis at high production rates by flame spray pyrolysis. *Chemical Engineering Science*, 58(10), 1969-1976. [https://doi.org/10.1016/S0009-2509\(03\)00022-8](https://doi.org/10.1016/S0009-2509(03)00022-8)
- Mukherjee, P. S., & Ray, A. K. (1999). Major challenges in the design of a large-scale photocatalytic reactor for water treatment. *Chemical Engineering & Technology: Industrial Chemistry-Plant Equipment-Process Engineering-Biotechnology*, 22(3), 253-260.
- Nakamura, H., Li, X., Wang, H., Uehara, M., Miyazaki, M., Shimizu, H., & Maeda, H. (2004). A simple method of self assembled nano-particles deposition on the micro-capillary inner walls and the reactor application for photo-catalytic and enzyme reactions. *Chemical Engineering Journal*, 101(1-3), 261-268.
- Nemani, S. K., Annavarapu, R. K., Mohammadian, B., Raiyan, A., Heil, J., Haque, M. A., Abdelaal, A., & Sojoudi, H. (2018). Surface modification of polymers: methods and applications. *Advanced Materials Interfaces*, 5(24), 1801247.
- Nisar, A., Saeed, M., Usman, M., Muneer, M., Adeel, M., Khan, I., & Akhtar, J. (2020). Kinetic modeling of ZnO-rGO catalyzed degradation of methylene blue. *International Journal of Chemical Kinetics*, 52(10), 645-654.
- Nishiyama, H., Yamada, T., Nakabayashi, M., Maehara, Y., Yamaguchi, M., Kuromiya, Y., Nagatsuma, Y., Tokudome, H., Akiyama, S., & Watanabe, T. (2021). Photocatalytic solar hydrogen production from water on a 100-m² scale. *Nature*, 598(7880), 304-307.
- Niu, Z., & Li, Y. (2014). Removal and Utilization of Capping Agents in Nanocatalysis. *Chemistry of Materials*, 26(1), 72-83. <https://doi.org/10.1021/cm4022479>
- Ola, O., & Maroto-Valer, M. M. (2015). Review of material design and reactor engineering on TiO₂ photocatalysis for CO₂ reduction. *Journal of Photochemistry and Photobiology C: Photochemistry Reviews*, 24, 16-42. <https://doi.org/10.1016/j.jphotochemrev.2015.06.001>
- Pandey, P. A., Bell, G. R., Rourke, J. P., Sanchez, A. M., Elkin, M. D., Hickey, B. J., & Wilson, N. R. (2011). Physical vapor deposition of metal nanoparticles on

- chemically modified graphene: observations on metal-graphene interactions. *Small*, 7(22), 3202-3210. <https://doi.org/10.1002/sml.201101430>
- Panigrahi, S., Kundu, S., Ghosh, S., Nath, S., & Pal, T. (2004). General method of synthesis for metal nanoparticles. *Journal of Nanoparticle Research*, 6(4), 411-414. <https://doi.org/10.1007/s11051-004-6575-2>
- Parashar, M., Shukla, V. K., & Singh, R. (2020). Metal oxides nanoparticles via sol-gel method: a review on synthesis, characterization and applications. *Journal of Materials Science: Materials in Electronics*, 31(5), 3729-3749. <https://doi.org/10.1007/s10854-020-02994-8>
- Pardieu, E., Chau, N. T. T., Dintzer, T., Romero, T., Favier, D., Roland, T., Edouard, D., Jierry, L., & Ritleng, V. (2016). Polydopamine-coated open cell polyurethane foams as an inexpensive, flexible yet robust catalyst support: a proof of concept. *Chemical communications*, 52(25), 4691-4693.
- Park, H., & Choi, W. (2005). Photocatalytic conversion of benzene to phenol using modified TiO₂ and polyoxometalates. *Catalysis Today*, 101(3), 291-297. <https://doi.org/https://doi.org/10.1016/j.cattod.2005.03.014>
- Park, J. Y., Aliaga, C., Renzas, J. R., Lee, H., & Somorjai, G. A. (2009). The role of organic capping layers of platinum nanoparticles in catalytic activity of CO oxidation. *Catalysis letters*, 129, 1-6.
- Pechini, M. P. (1967). Washington, DC: US patent and trademark office. *US patent*, 3, 697.
- Pedersen, H., & Elliott, S. D. (2014). Studying chemical vapor deposition processes with theoretical chemistry. *Theoretical Chemistry Accounts*, 133(5), 1476. <https://doi.org/10.1007/s00214-014-1476-7>
- Pizzi, A., & Ibeh, C. C. (2014). 2 - Phenol-Formaldehydes. In H. Dodiuk & S. H. Goodman (Eds.), *Handbook of Thermoset Plastics (Third Edition)* (pp. 13-44). William Andrew Publishing. <https://doi.org/https://doi.org/10.1016/B978-1-4557-3107-7.00002-6>
- Plutschack, M. B., Pieber, B., Gilmore, K., & Seeberger, P. H. (2017). The Hitchhiker's Guide to Flow Chemistry. *Chemical Reviews*, 117(18), 11796-11893. <https://doi.org/10.1021/acs.chemrev.7b00183>

- Pospíšil, J. (1988). Mechanistic action of phenolic antioxidants in polymers—A review. *Polymer Degradation and Stability*, 20(3), 181-202. [https://doi.org/https://doi.org/10.1016/0141-3910\(88\)90069-9](https://doi.org/https://doi.org/10.1016/0141-3910(88)90069-9)
- Pradhan, S. R., Nair, V., Giannakoudakis, D. A., Lisovytskiy, D., & Colmenares, J. C. (2020). Design and development of TiO₂ coated microflow reactor for photocatalytic partial oxidation of benzyl alcohol. *Molecular Catalysis*, 486, 110884. <https://doi.org/https://doi.org/10.1016/j.mcat.2020.110884>
- Pu, X., Zhang, B., & Su, Y. (2019). Heterogeneous photocatalysis in microreactors for efficient reduction of nitrobenzene to aniline: mechanisms and energy efficiency. *Chemical Engineering & Technology*, 42(10), 2146-2153.
- Puma, G., & Yue, P. (2003). Modelling and design of thin-film slurry photocatalytic reactors for water purification. *Chemical Engineering Science*, 58, 2269-2281. [https://doi.org/10.1016/S0009-2509\(03\)00086-1](https://doi.org/10.1016/S0009-2509(03)00086-1)
- Qian, Y., Chi, L., Zhou, W., Yu, Z., Zhang, Z., Zhang, Z., & Jiang, Z. (2016). Fabrication of TiO₂-modified polytetrafluoroethylene ultrafiltration membranes via plasma-enhanced surface graft pretreatment. *Applied Surface Science*, 360, 749-757.
- Qiao, S. Z., Liu, J., & Qing Lu, G. (2011). Chapter 21 - Synthetic Chemistry of Nanomaterials. In R. Xu, W. Pang, & Q. Huo (Eds.), *Modern Inorganic Synthetic Chemistry* (pp. 479-506). Elsevier. <https://doi.org/https://doi.org/10.1016/B978-0-444-53599-3.10021-6>
- Rahman, M., & Davey, K. (2018). Enabling Pt-free photocatalytic hydrogen evolution on polymeric melon: Role of amorphization for overcoming the limiting factors. *Physical Review Materials*, 2(12), 125402. <https://doi.org/10.1103/PhysRevMaterials.2.125402>
- Rahman, M. Z., Kibria, M. G., & Mullins, C. B. (2020). Metal-free photocatalysts for hydrogen evolution [10.1039/C9CS00313D]. *Chemical Society Reviews*, 49(6), 1887-1931. <https://doi.org/10.1039/C9CS00313D>
- Ramos, B., Ookawara, S., Matsushita, Y., & Yoshikawa, S. (2014). Low-cost polymeric photocatalytic microreactors: Catalyst deposition and performance for phenol degradation. *Journal of Environmental Chemical Engineering*, 2(3), 1487-1494.

- Rehm, T. H. (2020). Flow photochemistry as a tool in organic synthesis. *Chemistry–A European Journal*, 26(71), 16952-16974.
- Reilly, K., Fang, B., Taghipour, F., & Wilkinson, D. P. (2017). Enhanced photocatalytic hydrogen production in a UV-irradiated fluidized bed reactor. *Journal of Catalysis*, 353, 63-73. <https://doi.org/10.1016/j.jcat.2017.07.003>
- Reina, A., Jia, X., Ho, J., Nezich, D., Son, H., Bulovic, V., Dresselhaus, M. S., & Kong, J. (2009). Large Area, Few-Layer Graphene Films on Arbitrary Substrates by Chemical Vapor Deposition. *Nano Letters*, 9(1), 30-35. <https://doi.org/10.1021/nl801827v>
- Ren, W., & Cheng, H. M. (2014). The global growth of graphene. *Nat Nanotechnol*, 9(10), 726-730. <https://doi.org/10.1038/nnano.2014.229>
- Richardson, J. J., Björnmalm, M., & Caruso, F. (2015). Technology-driven layer-by-layer assembly of nanofilms. *Science*, 348(6233), aaa2491. <https://doi.org/10.1126/science.aaa2491>
- Roberts, E. J., Karadaghi, L. R., Wang, L., Malmstadt, N., & Brutchey, R. L. (2019). Continuous Flow Methods of Fabricating Catalytically Active Metal Nanoparticles. *ACS Applied Materials & Interfaces*, 11(31), 27479-27502. <https://doi.org/10.1021/acsami.9b07268>
- Ryu, J. H., Messersmith, P. B., & Lee, H. (2018). Polydopamine Surface Chemistry: A Decade of Discovery. *ACS Applied Materials & Interfaces*, 10(9), 7523-7540. <https://doi.org/10.1021/acsami.7b19865>
- Salvadó-Estivill, I., Brucato, A., & Li Puma, G. (2007). Two-Dimensional Modeling of a Flat-Plate Photocatalytic Reactor for Oxidation of Indoor Air Pollutants. *Industrial & Engineering Chemistry Research*, 46(23), 7489-7496. <https://doi.org/10.1021/ie070391r>
- Sauer, M. L., & Ollis, D. F. (1994). Acetone oxidation in a photocatalytic monolith reactor. *Journal of catalysis*, 149(1), 81-91.
- Schick, C. P., & Weber, P. M. (2001). Ultrafast dynamics in superexcited states of phenol. *The Journal of Physical Chemistry A*, 105(15), 3725-3734.
- Schmidt, R. (2005). Industrial catalytic processes—phenol production. *Applied Catalysis A: General*, 280, 89-103. <https://doi.org/10.1016/j.apcata.2004.08.030>

- Sender, M., & Ziegenbalg, D. (2017). Light sources for photochemical processes—estimation of technological potentials. *Chemie Ingenieur Technik*, 89(9), 1159-1173.
- Shah, N. K., Ivone, R., Shen, J., & Meenach, S. A. (2020). A comparison of centrifugation and tangential flow filtration for nanoparticle purification: A case study on acetalated dextran nanoparticles. *Particuology*, 50, 189-196. <https://doi.org/10.1016/j.partic.2019.06.004>
- Shen, C., Wang, Y., Xu, J., & Luo, G. (2015). Glass capillaries with TiO₂ supported on inner wall as microchannel reactors. *Chemical Engineering Journal*, 277, 48-55.
- Shen, Y., Gee, M. Y., & Greytak, A. B. (2017). Purification technologies for colloidal nanocrystals [10.1039/C6CC07998A]. *Chemical Communications*, 53(5), 827-841. <https://doi.org/10.1039/C6CC07998A>
- Shen, Y., Gee, M. Y., Tan, R., Pellechia, P. J., & Greytak, A. B. (2013). Purification of Quantum Dots by Gel Permeation Chromatography and the Effect of Excess Ligands on Shell Growth and Ligand Exchange. *Chemistry of Materials*, 25(14), 2838-2848. <https://doi.org/10.1021/cm4012734>
- Shen, Y., Roberge, A., Tan, R., Gee, M. Y., Gary, D. C., Huang, Y., Blom, D. A., Benicewicz, B. C., Cossairt, B. M., & Greytak, A. B. (2016). Gel permeation chromatography as a multifunctional processor for nanocrystal purification and on-column ligand exchange chemistry [10.1039/C6SC01301E]. *Chemical Science*, 7(9), 5671-5679. <https://doi.org/10.1039/C6SC01301E>
- Shen, Y., Weeranoppanant, N., Xie, L., Chen, Y., Lusardi, M. R., Imbrogno, J., Bawendi, M. G., & Jensen, K. F. (2017). Multistage extraction platform for highly efficient and fully continuous purification of nanoparticles [10.1039/C7NR01826F]. *Nanoscale*, 9(23), 7703-7707. <https://doi.org/10.1039/C7NR01826F>
- Shiraishi, Y., Saito, N., & Hirai, T. (2005). Adsorption-Driven Photocatalytic Activity of Mesoporous Titanium Dioxide. *Journal of the American Chemical Society*, 127(37), 12820-12822. <https://doi.org/10.1021/ja053265s>
- Singh, L. P., Bhattacharyya, S. K., Kumar, R., Mishra, G., Sharma, U., Singh, G., & Ahalawat, S. (2014). Sol-Gel processing of silica nanoparticles and their

- applications. *Advances in Colloid and Interface Science*, 214, 17-37.
<https://doi.org/https://doi.org/10.1016/j.cis.2014.10.007>
- Sonawane, R. S., & Dongare, M. K. (2006). Sol-gel synthesis of Au/TiO₂ thin films for photocatalytic degradation of phenol in sunlight. *Journal of Molecular Catalysis A: Chemical*, 243(1), 68-76.
<https://doi.org/https://doi.org/10.1016/j.molcata.2005.07.043>
- Song, K. C., Lee, S. M., Park, T. S., & Lee, B. S. (2009). Preparation of colloidal silver nanoparticles by chemical reduction method. *Korean Journal of Chemical Engineering*, 26(1), 153-155. <https://doi.org/10.1007/s11814-009-0024-y>
- Su, Y., Straathof, N. J., Hessel, V., & Noël, T. (2014). Photochemical transformations accelerated in continuous-flow reactors: basic concepts and applications. *Chemistry—A European Journal*, 20(34), 10562-10589.
- Sudha, D., & Sivakumar, P. (2015). Review on the photocatalytic activity of various composite catalysts. *Chemical Engineering and Processing: Process Intensification*, 97, 112-133.
- Sundar, K. P., & Kanmani, S. (2020). Progression of Photocatalytic reactors and it's comparison: A Review. *Chemical Engineering Research and Design*, 154, 135-150.
- Sweeney, S. F., Woehrle, G. H., & Hutchison, J. E. (2006). Rapid Purification and Size Separation of Gold Nanoparticles via Diafiltration. *Journal of the American Chemical Society*, 128(10), 3190-3197. <https://doi.org/10.1021/ja0558241>
- Tahir, M. B., Rafique, M., Rafique, M. S., Fatima, N., & Israr, Z. (2020). Chapter 6 - Metal oxide- and metal sulfide-based nanomaterials as photocatalysts. In M. B. Tahir, M. Rafique, & M. S. Rafique (Eds.), *Nanotechnology and Photocatalysis for Environmental Applications* (pp. 77-96). Elsevier.
<https://doi.org/https://doi.org/10.1016/B978-0-12-821192-2.00006-1>
- Takei, G., Kitamori, T., & Kim, H.-B. (2005). Photocatalytic redox-combined synthesis of L-pipecolic acid with a titania-modified microchannel chip. *Catalysis Communications*, 6(5), 357-360.
- Tani, T., Mädler, L., & Pratsinis, S. E. (2002). Homogeneous ZnO Nanoparticles by Flame Spray Pyrolysis. *Journal of Nanoparticle Research*, 4(4), 337-343.
<https://doi.org/10.1023/A:1021153419671>

- Tavakoli, A., Sohrabi, M., & Kargari, A. (2007). A review of methods for synthesis of nanostructured metals with emphasis on iron compounds. *61*(3), 151-170. <https://doi.org/doi:10.2478/s11696-007-0014-7> (Chemical Papers)
- Teoh, W. Y. (2013). A Perspective on the Flame Spray Synthesis of Photocatalyst Nanoparticles. *Materials*, *6*(8), 3194-3212. <https://www.mdpi.com/1996-1944/6/8/3194>
- Teoh, W. Y., Amal, R., & Mädler, L. (2010). Flame spray pyrolysis: An enabling technology for nanoparticles design and fabrication. *Nanoscale*, *2*(8), 1324-1347.
- Thomson, C. G., Lee, A.-L., & Vilela, F. (2020). Heterogeneous photocatalysis in flow chemical reactors. *Beilstein Journal of Organic Chemistry*, *16*, 1495-1549. <https://doi.org/10.3762/bjoc.16.125>
- Trewyn, B. G., Slowing, I. I., Giri, S., Chen, H.-T., & Lin, V. S. Y. (2007). Synthesis and Functionalization of a Mesoporous Silica Nanoparticle Based on the Sol-Gel Process and Applications in Controlled Release. *Accounts of Chemical Research*, *40*(9), 846-853. <https://doi.org/10.1021/ar600032u>
- Vallejos, S., Selina, S., Annanouch, F. E., Gràcia, I., Llobet, E., & Blackman, C. (2016). Aerosol assisted chemical vapour deposition of gas sensitive SnO₂ and Au-functionalised SnO₂ nanorods via a non-catalysed vapour solid (VS) mechanism. *Scientific Reports*, *6*(1), 28464. <https://doi.org/10.1038/srep28464>
- Van Gerven, T., Mul, G., Moulijn, J., & Stankiewicz, A. (2007). A review of intensification of photocatalytic processes. *Chemical Engineering and Processing: Process Intensification*, *46*(9), 781-789.
- Vidyacharan, S., Ramanjaneyulu, B. T., Jang, S., & Kim, D. P. (2019). Continuous-flow visible light organophotocatalysis for direct arylation of 2H-Indazoles: fast access to drug molecules. *ChemSusChem*, *12*(12), 2581-2586.
- Vinnacombe-Willson, G. A., Conti, Y., Stefancu, A., Weiss, P. S., Cortés, E., & Scarabelli, L. (2023). Direct Bottom-Up In Situ Growth: A Paradigm Shift for Studies in Wet-Chemical Synthesis of Gold Nanoparticles. *Chemical Reviews*, *123*(13), 8488-8529. <https://doi.org/10.1021/acs.chemrev.2c00914>
- Visan, A., van Ommen, J. R., Kreutzer, M. T., & Lammertink, R. G. H. (2019). Photocatalytic Reactor Design: Guidelines for Kinetic Investigation. *Industrial*

- & *Engineering Chemistry Research*, 58(14), 5349-5357.
<https://doi.org/10.1021/acs.iecr.9b00381>
- Wallace, R., Brown, A., Brydson, R., Wegner, K., & Milne, S. (2013). Synthesis of ZnO nanoparticles by flame spray pyrolysis and characterisation protocol. *Journal of Materials Science*, 48, 6393-6403.
- Wang, H., Li, X., Zhao, X., Li, C., Song, X., Zhang, P., Huo, P., & Li, X. (2022). A review on heterogeneous photocatalysis for environmental remediation: From semiconductors to modification strategies. *Chinese Journal of Catalysis*, 43(2), 178-214. [https://doi.org/https://doi.org/10.1016/S1872-2067\(21\)63910-4](https://doi.org/https://doi.org/10.1016/S1872-2067(21)63910-4)
- Wang, K., Zhang, H., Shen, Y., Adamo, A., & Jensen, K. F. (2018). Thermoformed fluoropolymer tubing for in-line mixing [10.1039/C8RE00112J]. *Reaction Chemistry & Engineering*, 3(5), 707-713. <https://doi.org/10.1039/C8RE00112J>
- Wang, N., Lei, L., Zhang, X., Tsang, Y., Chen, Y., & Chan, H. L. (2011). A comparative study of preparation methods of nanoporous TiO₂ films for microfluidic photocatalysis. *Microelectronic engineering*, 88(8), 2797-2799.
- Wang, T., Xia, M., & Kong, X. (2018). The Pros and Cons of Polydopamine-Sensitized Titanium Oxide for the Photoreduction of CO₂. *Catalysts*, 8(5), 215. <https://www.mdpi.com/2073-4344/8/5/215>
- Wang, Z., Hojo, H., & Einaga, H. (2022). One-step oxidation of benzene to phenol with H3PW12O₄₀ under photoirradiation: Effect of operating conditions. *Chemical Engineering Journal*, 427, 131369.
- Wang, Z., Zou, Y., Li, Y., & Cheng, Y. (2020). Metal-containing polydopamine nanomaterials: catalysis, energy, and theranostics. *Small*, 16(18), 1907042.
- Ward, D. A., & Ko, E. I. (1995). Preparing Catalytic Materials by the Sol-Gel Method. *Industrial & Engineering Chemistry Research*, 34(2), 421-433. <https://doi.org/10.1021/ie00041a001>
- Weeranoppanant, N. (2019). Enabling tools for continuous-flow biphasic liquid-liquid reaction [10.1039/C8RE00230D]. *Reaction Chemistry & Engineering*, 4(2), 235-243. <https://doi.org/10.1039/C8RE00230D>
- Wei, D., Huang, L., Liang, H., Zou, J., Chen, W., Yang, C., Hou, Y., Zheng, D., & Zhang, J. (2021). Photocatalytic hydroxylation of benzene to phenol over

- organosilane-functionalized FeVO₄ nanorods. *Catalysis Science & Technology*, 11(17), 5931-5937.
- Wu, Z., Jiang, D.-e., Mann, A. K. P., Mullins, D. R., Qiao, Z.-A., Allard, L. F., Zeng, C., Jin, R., & Overbury, S. H. (2014). Thiolate Ligands as a Double-Edged Sword for CO Oxidation on CeO₂ Supported Au₂₅(SCH₂CH₂Ph)₁₈ Nanoclusters. *Journal of the American Chemical Society*, 136(16), 6111-6122. <https://doi.org/10.1021/ja5018706>
- Yang, Y., Li, J., Lin, L., & Peng, X. (2015). An efficient and surface-benign purification scheme for colloidal nanocrystals based on quantitative assessment. *Nano Research*, 8(10), 3353-3364. <https://doi.org/10.1007/s12274-015-0835-6>
- Yen, B. K., Stott, N. E., Jensen, K. F., & Bawendi, M. G. (2003). A continuous-flow microcapillary reactor for the preparation of a size series of CdSe nanocrystals. *Advanced Materials*, 15(21), 1858-1862.
- You, H., Yang, S., Ding, B., & Yang, H. (2013). Synthesis of colloidal metal and metal alloy nanoparticles for electrochemical energy applications [10.1039/C2CS35319A]. *Chemical Society Reviews*, 42(7), 2880-2904. <https://doi.org/10.1039/C2CS35319A>
- Yuzawa, H., Aoki, M., Otake, K., Hattori, T., Itoh, H., & Yoshida, H. (2012). Reaction Mechanism of Aromatic Ring Hydroxylation by Water over Platinum-Loaded Titanium Oxide Photocatalyst. *The Journal of Physical Chemistry C*, 116(48), 25376-25387. <https://doi.org/10.1021/jp308453d>
- Zangmeister, R. A., Morris, T. A., & Tarlov, M. J. (2013). Characterization of Polydopamine Thin Films Deposited at Short Times by Autoxidation of Dopamine. *Langmuir*, 29(27), 8619-8628. <https://doi.org/10.1021/la400587j>
- Zhang, C., Yang, H.-C., Wan, L.-S., Liang, H.-Q., Li, H., & Xu, Z.-K. (2015). Polydopamine-coated porous substrates as a platform for mineralized β -FeOOH nanorods with photocatalysis under sunlight. *ACS applied materials & interfaces*, 7(21), 11567-11574.
- Zhang, G., Yi, J., Shim, J., Lee, J., & Choi, W. (2011). Photocatalytic hydroxylation of benzene to phenol over titanium oxide entrapped into hydrophobically modified siliceous foam. *Applied Catalysis B: Environmental*, 102(1-2), 132-139.

- Zhang, P., Weeranoppanant, N., Thomas, D. A., Tahara, K., Stelzer, T., Russell, M. G., O'mahony, M., Myerson, A. S., Lin, H., & Kelly, L. P. (2018). Advanced continuous flow platform for on-demand pharmaceutical manufacturing. *Chemistry—A European Journal*, *24*(11), 2776-2784.
- Zhang, R.-X., Braeken, L., Luis, P., Wang, X.-L., & Van der Bruggen, B. (2013). Novel binding procedure of TiO₂ nanoparticles to thin film composite membranes via self-polymerized polydopamine. *Journal of membrane science*, *437*, 179-188.
- Zhang, W., Zhang, J., Chen, Z., & Wang, T. (2009). Photocatalytic degradation of methylene blue by ZnGa₂O₄ thin films. *Catalysis Communications*, *10*(13), 1781-1785. <https://doi.org/https://doi.org/10.1016/j.catcom.2009.06.004>
- Zhang, W., Zhou, W., & Chen, Z. (2014). Graphene/polydopamine-modified polytetrafluoroethylene microtube for the sensitive determination of three active components in Fructus Psoraleae by online solid-phase microextraction with high-performance liquid chromatography. *Journal of separation science*, *37*(21), 3110-3116.
- Zhou, M., Roualdès, S., & Ayril, A. (2015). New photocatalytic contactors obtained by PECVD deposition of TiO₂ thin layers on the surface of macroporous supports. *The European Physical Journal Special Topics*, *224*(9), 1871-1882. <https://doi.org/10.1140/epjst/e2015-02506-8>
- Zhu, X., Feng, H., Chen, R., Liao, Q., Ye, D., Zhang, B., Liu, J., Liu, M., & Chen, G. (2018). Experimental study on the durability of the polydopamine functionalized gas–liquid–solid microreactor for nitrobenzene hydrogenation. *RSC advances*, *8*(11), 5661-5669.
- Znaidi, L. (2010). Sol–gel-deposited ZnO thin films: A review. *Materials Science and Engineering: B*, *174*(1), 18-30. <https://doi.org/https://doi.org/10.1016/j.mseb.2010.07.001>

BIOGRAPHY

NAME Chetsada Khositanon

DATE OF BIRTH 7 August 1994

PLACE OF BIRTH Nakhon Ratchasima, Thailand

PRESENT ADDRESS 5 Sueksa Charoen Road, Nai Mueang, Mueang
Phetchabun District, Phetchabun, Thailand, 67000

EDUCATION 2013-2016 Bachelor of Engineering (Mechanical
Engineering), Faculty of Engineering, King Mongkut's
University of Technology North Bangkok, Bangkok,
Thailand

AWARDS OR GRANTS Royal Golden Jubilee (RGJ) Ph.D. scholarships

